Surface Characterization and Reactivity of Methylammionium Lead Iodide

by
Kenneth Zielinski

A Thesis

Submitted to the Faculty of the

WORCESTER POLYTECHNIC INSTITUTE

in partial fulfillment of the requirements for the
Master of Science Degree
in Chemistry
October 2018

APPROVED:

_____

Assistant Professor Ronald L. Grimm, Advisor

_____

Associate Professor N. Aaron Deskins, Committee Member

_____

Associate Teaching Professor Christopher Lambert, Committee Member

_____

Associate Professor Shawn Burdette, Committee Member

_____

Professor Arne Gericke, Department Head

Abstract

We quantify the chemical species present at and reactivity of the tetragonal (100) face of single-crystal methylammonium lead iodide, $MAPbI_3$(100). $MAPbI_3$ is an ABX_3 perovskite, experiments utilized the orthogonal reactivity of the A^+-site cation, the B^{2+}-site cation, and the X^--site halide anion. Ambient-pressure exposure to BF_3 solutions probe the reactivity of interfacial halides. Reactions with *p*-trifluoromethylanilinium chloride probe the exchange reactivity of the A^+-site cation. The ligand 4,4'-bis(trifluoromethyl)-2,2'-bipyridine probe for interfacial B^{2+}-site cations. Fluorine features in x-ray photoelectron spectroscopy (XPS) quantify reaction extents with each solution-phase species. XP spectra reveals adsorption of BF_3 indicating surface-available halide anions on tetragonal $MAPbI_3$(100) and preliminary examinations on the (112), (110), and thin-film surfaces. Temperature-programmed desorption (TPD) established a ~200 kJ mol^{-1} desorption activation energy from tetragonal $MAPbI_3$(100). Adsorption of the fluorinated anilinium cation includes no concomitant adsorption of chlorine as revealed by the absence of Cl 2p features within the limits of XPS detection on the tetragonal (100) and (112) faces with no discernable exchange in preliminary experiments on tetragonal (110). Within detection limits, bipyridine ligand demonstrate no adsorption to tetragonal $MAPbI_3$(100) or (112), while it does demonstrate significant adsorption on the (110) in preliminary experiments. We discuss the present results in the context of interfacial stability, passivation, and reactivity for perovskite-based energy conversion materials and some preliminary investigations into bilayer graphene-based dye sensitized photovoltaic materials.

Acknowledgements

I would like to thank everyone who has supported me through this journey of knowledge, scientific exploration, and growth. I would especially like to thank Professor Ronald Grimm for his support and encouragement through my experience as a student and researcher. With his guidance, I gained valuable laboratory skills, scientific knowledge, understanding, and perhaps more importantly a deeper knowledge of myself as a scientist and person. Thank you for your support, your knowledge, talent as a scientist, and for being among the most enthusiastic people that I have ever had the opportunity to meet. I would like to thank the Grimmgroup for their support and encouragement. I would like to thank Alex Carl for teaching me how to use the XPS, Weiran (Sasha) Gao for her assistance with the TPD rebuild, and Roghi Kalan for helping me start with my research on perovskites. I would like to thank my committee; Professor Deskins, Professor Lambert, Professor Burdette, and formerly Dr. Emmert for their support and encouragement.

I would like to thank my family for the support and kindness that they gave me throughout my work.

Table of Contents

List of Figures

Chapter 1. Introduction

High optical absorption, defect tolerance, and straightforward processing methods drive research and development efforts of perovskite-based solar-energy-conversion photovoltaics.[1–4] Large bandgap tunability and ease of processing may enable scalable deployment of inexpensive tandem-junction solar cells that break the single-junction Shockley–Queisser limit[5], as well as LEDs with wide spectral tunability.[6,7] However, significant research remains before practical realization of devices based on such materials.

Despite several desirable physical and electronic properties, solar-relevant perovskite materials undergo deleterious chemical reactions that degrade performance and long-term stability. A critical challenge facing the lead halide perovskites is decomposition or degradation associated with ambient environmental conditions including humidity, oxygen, and thermal stressors.[8–14] Significant efforts address surface passivation by surface functionalization with chemical methods including thiol functionalization;[15] hydrophobic, fluorinated organic salts;[16] and quaternary ammonium halides.[17] However, a lack of understanding the fundamental surface composition and reactivity at the atom-and-bond level hinders the effective functionalization and passivation of the surfaces. Functionalization via Atomic Layer Deposition (ALD) enables passivation with carrier selectivity or blocking, and demonstrates promise.[18] ALD-deposited, low-defect, electron-transport layers of TiO_2 yielded increased solar energy conversion efficiency as compared to TiO_2 deposited via other methods for methylammonium lead iodide-based devices.[19] Notably, ALD film quality strongly

influences device performance, and variations between deposition techniques for titania-based electron-transport layers yield drastic differences in subsequent device efficiency.[19,20] Selective charge transport, chemical contact, and band-gap tuning may be further enhanced by thiophene functionalization due to its implications as a highly-tunable, conductive organic molecule.[21] Together, the ambient instability at perovskite surfaces and the challenges associated with their passivation drive fundamental studies into the interfacial chemical species, their chemistry, and how their chemistry may be exploited to effect stable, long-term passivation.

High mechanical strength, ideal electronic properties, atomic scale, and high natural abundance, together position graphene to be a strong choice in post-silicon electronics, motivating research and development efforts for graphene-based electronic materials.[22–24] Graphene can be doped and has been applied as a p-n junction.[23,25] Graphene has also found application as a Schottky junction solar cell with n-type silicon, attaining modest efficiency, but due to the vast tunability of graphene other substrates and materials are straightforward to utilize.[26] A dye sensitized solar cell (DSSC) is an alternative to solid state photovoltaic devices with some advantages including simple and versatile fabrication and is considered to be a promising contender in third-generation photovoltaic technology.[27] The design of a functioning bilayer graphene DSSC and subsequent fundamental studies to understand the photoelectrochemical properties will aid in the determination where its niche lies in the energy landscape.

Chapter 2. Background of Methylammonium Lead Iodide

2.1. Overview

Researchers have studied the surfaces of several lead-containing and lead-free solar-and-LED-relevant perovskites. Based on infrared spectroscopic studies, researchers hypothesize that the $(100)_t$ faces of methylammonium lead iodide, $MAPbI_3$, terminate in iodide anions and methylammonium cations. Interfacial methylammonium cations orient such that the methyl group points away from the crystal face and the ammonium cation points towards the crystal as analogous to surfactant orientations.[28–30] Analogous studies of $(110)_t$ faces indicate interfacial lead and iodide terminations. Computational studies demonstrate that the PbI_2-terminated and methylammonium-terminated $(100)_t$ faces are both thermodynamically stable with the methylammonium termination being the more favorable of the two.[31] Computational studies further predict that the forbidden energy gap of $MAPbI_3$ decreases with PbI_2 termination at 1.4 eV and increases with methylammonium-terminated faces to 1.69 eV, relative to an experimental 1.5 eV band gap.[31] However, fundamental studies regarding the surface reactivity, including grain reformation chemistry,[32] remain underexplored. Elucidation of the interfacial chemical species and their reactivity for lead-based perovskites should enable optimal passivation, carrier selectivity/collection, band-edge alignment, and band gap tuning.[33–35] Developing a thorough, fundamental understanding of the surface, its composition, and how to use this knowledge to our advantage will enable more efficient devices and other useful functional surface functionalities. Such studies motivate the present investigation with much work dedicated to the $MAPbI_3$ $(100)_t$ facet and some preliminary studies conducted on the $(112)_t$, $(110)_t$, and thin-film materials.

Chapter 3. Synthesis of Methylammonium Lead Iodide, Surface Derivatization, and Analytical Methods

This chapter details the synthesis of methylammonium lead iodide crystals, the reaction conditions used in these experiments, instrumental methods, and fundamental explanations for both the XPS and TPD.

3.1. Materials

Inert environments for sample preparation, reaction, and storage included an argon-purged (ultrahigh purity, UHP, Airgas) Schlenk line equipped with an oil-diffusion pump with a base pressure below 1×10^{-3} torr. Larger inert environments included a nitrogen-purged (UHP, Airgas) recirculating glovebox (mBraun Inc., Stratham, NH) with an active catalyst to maintain oxygen concentrations below 0.5 ppm as measured by a commercial oxygen sensor.

All chemicals were used as received unless otherwise noted. A Millipore Milli-Q system provided 18 MΩ cm resistivity water for all water requirements. Chemicals used in the production and processing of methylammonium lead iodide crystals included lead iodide (PbI_2, 99.9985% metals basis, Alfa Aesar), γ-butylrolactone (GBL, 99%, Sigma Aldrich), methylamine ($CH_3NH_{2(aq)}$, 40 wt. % in water, Alfa Aesar), hydroiodic acid ($HI_{(aq)}$, 55–58 wt. % in water, Alfa Aesar), ethanol (EtOH, 91%, denatured, Alfa Aesar), and diethyl ether (Et_2O, 99 %, Alfa Aesar). Diethyl ether, dichoromethane (DCM), and *n*-hexane were dried over molecular sieves (3Å, Alfa Aesar, degassed overnight >200 °C under vacuum).

Materials for sample mounting and dicing included paraffin mounting wax (Electron Microscopy Sciences, Hatfield, PA), silicone oil (Acros Organics), a low-speed precision

rotary saw equipped with a diamond blade (IsoMet Low Speed Saw, Buehler, Lake Bluff, IL), a polishing station (MiniMet 1000, Buehler) that utilized with 600 grit silicon carbide paper, and 600 grit silicon carbide particles (Buehler) suspended in silicone oil on a polishing cloth (TexMet, Buehler).

Surface basicity and reactivity experiments of the X^- anion utilized boron trifluoride (BF_3, 46.5 wt. % in diethyl ether, Alfa Aesar) and Et_2O that were dried over sieves and degassed via three freeze-pump-thaw cycles on the Schlenk line prior to use. Reactions probing the chemistry of the A^+ cation site additionally employed *p*-trifluoromethyl aniline (99%, Sigma-Aldrich), hydrochloric acid ($HCl_{(aq)}$, 35-38 wt. %, Acros Organics), tetrachloroethane (TCE, 99%, Alfa Aesar), and DCM from a commercial solvent system (Pure Process Technology, Nashua, NH) and stored over sieves. Chemicals for reactions targeting the B^{2+} cation included tetrabutylammonium iodide (98%, Acros Organics), potassium carbonate (99.0% min., Alfa Aesar), 2-bromo-4-(trifluoromethyl)pyridine (Oakwood Chemical), *i*-propanol (IPA, 99+%, Fisher Chemical), N,N'-dimethylformamide (DMF, 99+%, Sigma), DCM, *n*-hexane (99+%, anhydrous, Alfa Aesar), and ethylacetate (ACS Reagent grade, Pharmco-Aaper).

Chemicals used in the thiophene surface exchange reactions include 2-thiphenemethylamine (97%, Alfa Aesar), acetonitrile (99.8%, Acros Organics), chlorobenzene (99.8%, extra dry, Acros Organics), anisole (99%, Acros Organics), thiophene(99%, Alfa Aesar), tetrahydrothiophene (98%, Alfa Aesar), ethyl acetate (ACS grade, Pharmco-Aaper), toluene (ACS grade, Fisher Chemical), hexafluorophosphoric acid (55% wt. in water, Aldrich), tetrafluoroboric acid (50% wt. in water, Alfa Aesar)

Chemicals used in the boric acid adsorption experiments include boric acid (99.6%, Acros Organics), diethyl ether (Et_2O, 99 %, Alfa Aesar), *n*-hexane (99+%, anhydrous, Alfa Aesar), anisole (99%, Acros Organics), and toluene (ACS grade, Fisher Chemical).

Chemicals used in the 4-trifluoromethylphenylboronic acid, pinacol ester experiments include 4-trifluoromethylboronic acid, pinacol ester (97%, Boron Molecular), chlorobenzene (99.8%, extra dry, Acros Organics), diethyl ether (Et_2O, 99 %, Alfa Aesar), and dichloromethane (DCM).

Chemicals used in the phenylborane experiments include triphenylborane (96%, Alfa Aesar), and tris(pentafluorophenyl)borane (95%, Acros Organics), *n*-hexane (99+%, anhydrous, Alfa Aesar), and dichloromethane (DCM).

Chemicals used in the ammonium ALD chemical hook experiments include 4-aminobenzoic acid (99%, Acros Organics), 5-aminoisophthalic acid (98%, Acros Organics), 3-nitrobenzoic acid (99%, Alfa Aesar), bromotrichloromethane (99%, Acros Organics), triphenylphosphine (99%, Acros Organics), triethylamine was stored over 3A molecular sieves and freeze-pump-thawed (99.7%-extra pure, Acros Organics), zinc dust (Acros Organics), ammonium formate (99%, Acros Organics), methanol (99.9%, semiconductor grade, Alfa Aesar), and dichloromethane (DCM).

Chemicals used in the attempted synthesis in tris(3,4,5-trifluorophenyl)borane include 5-Bromo-1,2,3-trifluorobenzene (98%, Alfa Aesar), magnesium turnings (99.98% metals basis, 1 cm and down, Alfa Aesar) activated by mechanical grinding and lithium

aluminum hydride (4.0 M in diethyl ether, Acros Organics), diethyl ether (Et_2O, 99 %, Alfa Aesar), toluene (ACS grade, Fisher Chemical), and boron trifluoride (BF_3, 46.5 wt. % in diethyl ether, Alfa Aesar), *n*-hexane (99+%, anhydrous, Alfa Aesar).

3.2. Methods

3.2.1. Methylammonium Lead Iodide Single Crystal Synthesis

Prior to the synthesis of $MAPbI_3$, the acidification of methylamine by HI yielded methylammonium iodide.[32] Methylamine was added to ice-cold $HI_{(aq)}$ and stirred for two hours over ice after which rotary evaporation removed the solvent. The resulting precipitate was recrystallized from a nominal amount of ethanol in diethyl ether, filtered, and dried at 40 °C on the Schlenk line overnight.

Inverse-temperature crystallization yielded large methylammonium lead iodide crystals from methylammonium iodide and lead iodide.[36] A 1.23 M solution of both methylammonium iodide and lead iodide in GBL was prepared at 60 °C, and covered tightly. The temperature of the reaction vessel was raised to and subsequently maintained at 105 ± 1 °C for 24–48 h to yield methylammonium lead iodide crystals. Upon removal from the reagent solution, crystal cleaning utilized expeditious rinsing with sequential exposure to GBL, $HI_{(aq)}$, and diethyl ether, followed by drying under an argon stream. The resulting $MAPbI_3$ crystals with ~cm^2 $(100)_t$ and $(112)_t$ facets[37] were stored in a recirculating glovebox until further use.

Dicing and polishing steps yielded methylammonium lead iodide wafer-shaped samples with large exposed facets. Mounting wax affixed crystals parallel to $(100)_t$ or $(112)_t$ facets depending on the facet of interest, and water-free and degassed silicon oil

replaced traditional lubricants that yielded yellow deposits that we ascribed to water-catalyzed disproportionation and PbI_2 formation. Of the $MAPbI_3$ wafers with one nascent, as-synthesized face and one cut face, we considered the nascent face to be the "top" of the wafer that was used for all subsequent surface science investigations. Of the $MAPbI_3$ wafers with two cut faces, one side was subsequently polished to produce their top surfaces. Rough-cut $MAPbI_3$ wafers were polished via sequential steps of 600 grit sand paper and 600 grit silicon carbide slurry in silicone oil, a polishing cloth with 0.05 μm alumina, and finally on an oiled polishing cloth. A final chemical polish via submersion in $HI_{(aq)}$ and rinsing steps as with the synthesized crystals completed wafer preparation. All $MAPbI_3$ wafers were used directly or stored in a recirculating glovebox until further use.

3.2.2. Methylammonium Lead Iodide Single Crystal Synthesis Tips/ Updates

Perovskites can be synthesized by the aforementioned techniques. There are however techniques that can help the process. Overloading the solution with precursor will lead to a murky brown-black solution which is undesirable initially. The dark brown-black color occurs naturally over time. The current best recipe utilizes a solution of 1.0 M lead iodide and 1.1 M methylammonium iodide. The material is dissolved at 60 °C for about 2 hours. The stir bar is removed and the temperature is increased to 100 °C until stable, then finally to 105 ± 1 °C for initial crystallization. Subsequent reuse of the perovskite solution proceeds using the aforementioned procedure but is more effective at 109 °C. The solution can be reused many times and is considered "dead" when it ceases to produce perovskites and attains an oily appearance. The GBL can evaporate, albeit slowly at the crystallization temperature. This can be both advantageous for slow growth

of larger perovskites, but can also be detrimental if it causes uncontrolled perovskite growth. If needed, a suitable volume of GBL can be replaced.

The perovskite heating controllers are capable and useful tools for temperature-controlled experiments. The controllers can be controlled via computer through a LabView program. This enables ramped heating over long periods of time if a crystallization growth experiment requires it. It is extremely important to be cautious when using an oil bath. The thermocouple must be firmly secured to eliminate the possibility of losing contact. If the thermocouple becomes dislodged, excessive heating may result.

Perovskites may be sliced on a saw using the aluminum sample mounts. Mounting wax is dissolved in dichloromethane to make a paste. The paste is then applied to the mount and the perovskite is pressed into the paste with the desired face flat on the sample mount. The mounted perovskite is then dried in the vacuum oven at room temperature for at least three days and longer is typically better. Under three days of curing, the mounting paste is not rigid enough to hold the perovskite during cutting. The wax will expand and look “cloud-like” as in Figure 1 before collapsing onto the perovskite.

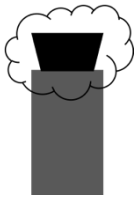

Figure 1. Cartoon of the perovskite being mounted on its face for slicing. The wax becomes “cloud-like” when dry.

3.3.3. Methylammonium Lead Iodide Thin-film Synthesis

Thin film perovskites were synthesized using a 40% by weight solution of lead iodide and methylammonium iodide in N,N’-dimethylformamide. This solution was drop-cast onto FTO slides. FTO slides were cleaned ultrasonically in isopropyl alcohol and >18 MΩ water. The perovskite solution was allowed to sit for 60 seconds on the slide prior to

beginning the spin coating process. Samples were treated to 2000 RPM at an acceleration value of 500 for 30 seconds. About 10 seconds into the spinning, about 1 ml of dry diethyl ether was dropped into the sample. The samples were then annealed on a 110 °C hotplate for 10 minutes.

3.3.4. Methylammonium Lead Iodide Cuboid Crystal Synthesis

Methylammonium lead iodide cuboids were synthesized using an antisolvent assisted crystallization.[37] A solution of 1.5 M methylammonium iodide and 0.5 M lead iodide in GBL in a rubber septum stoppered vial with a 20 gauge needle is held at 40 °C for several days. Chloroform in a 3:1 ratio by volume is in the base of the larger exterior beaker and diffuses through the needle into the vial. After about two days, small crystals form and after 3-4 days visibly distinguished cubioid samples grow.

Cuboid perovskite synthesis to enable easy access to $(110)_t$ faces still needs additional development. Using a 22 G needle seems to produce better samples. Less chloroform, antisolvent to a point improves crystal growth in terms of quality and size. As of now, a 1:1.5 ratio of perovskite solution to chloroform has shown the best yield from a qualitative standpoint. 1:1 results in very low yields, 1:1.5 results in moderate yields with good size and shape, 1:2 results in high yield but many polycrystalline samples, and the 1:3 ratio results in the greatest degree of crystallization, but the overall smallest size and most polycrystalline products. Solvent diffusion at ambient temperature lacks sufficient driving force to volatilize sufficient quantities of either chloroform or dichloromethane to initiate or drive crystallization. Ambient temperature diffusion may be a useful slow growth method to produce large crystals, but will most likely require solvents with a higher vapor

pressure. Chlorobenzene does not exhibit sufficient volatility, even at 50 °C, to diffuse into the perovskite solution in sufficient volumes in a reasonable timeframe.

3.3.4. Reagent Preparations

The halide site reactivity experiments all utilized freeze-pump-thawed solvents that had been stored over 3 Å molecular sieves. BF_3 solutions were prepared as 0.1 M in diethyl ether, n-hexane/DCM (v/vv = 10:1), or toluene. Boric acid was prepared at the solubility limit in n-hexane/ toluene/ anisole: diethyl ether (v/v = 10:1) solvent mixtures. The 4-trifluoromethylphenylboronic acid, pinacol ester was examined at 10 mM in diethyl ether, 40 mM diethyl ether and DCM, and 80 mM in chlorobenzene.

Ammonium exchange reagents were used as received or synthesized from the corresponding amine. Amines were acidified using a 1 M acid solution and filtered to yield the salt. Ammoniums were dissolved to their solubility limit and filtered to remove excess. Preparation of the 2-thiophene methylammonium salt was successfully prepared as a chloride and hexafluorophosphate but unsuccessful thus far as a tetrafluoroborate. These reactions are exothermic and should be conducted with care.

Metal ligation experiments utilized 4,4'-bis(trifluoromethyl)-2,2'-bipyridine as the test reagent. The fluorinated bpy compound was synthesized from 2-bromo-4-(trifluoromethyl) pyridine (1 g, 4.4 mmol), palladium acetate (50 mg, 0.22 mmol), tetrabutylammonium iodide (1.63 g, 4.4 mmol), potassium carbonate (916 mg, 6.6 mmol), and isopropyl alcohol (0.68 mL, 8.8 mmol) in 15 mL of DMF.[38,39] The reaction mixture was heated at 100 °C for 20 h. The mixture was filtered through a fine fritted funnel. DCM (50 mL) was added to the filtrate and was washed with DI water three times. The aqueous

fractions were washed with an additional 20 mL of DCM and combined. The DCM fraction was dried over anhydrous magnesium sulfate and concentrated to dryness. The crude product was dissolved in 2 mL of DCM and loaded onto a silica gel column using hexane/ ethyl acetate (v:v = 10:1) as eluent. The first three fractions were collected, combined, and dried to yield an off white-orange solid. The solid was further purified via vacuum sublimation at 60 °C with a liquid nitrogen cooled cold-finger to yield a pure white powder. The 4,4'-bis(trifluoromethyl)-2,2'-bipyridine was prepared as a 10 mM solution in DCM for application. Wafer transfer, exposure, rinsing, and drying proceeded as above for 60-minute exposures of $MAPbI_3(100)_t$.

Initial synthesis of 3,3'-dinitrobenzoicanhydride as a stepping stone towards surface orientation experiments using 3,3'-diaminobenzoicanhydrides has been completed. Beyond the simple anhydride, methylene, naphthalic, and other groups are possible methods to attain desirable amino spacing. The 3,3'-diaminobenzoic anhydride has a spacing of approximately 7.2–7.8 Å as determined by Gaussian calculations using PM3 or B3LYP and the 6-31G(d) basis set. This is slightly larger than the ammonium group spacing as observed in VESTA point-to-point spacing. here is some room for flexibility of the molecule, which may be advantageous. Methylene or naphthalene style bridges can produce spacings of approximately 9.6 to 10.5 or approximately 12 to 12.3 Å spacing respectively depending on the rotation of the molecule. These two spacings are hypothesized to be capable of substituting into diagonal sites or every other linear site with approximate spacings of 8.9 and 12.6 Å respectively. It is also important to note that the approximate distance between the ammonium groups on the anhydride is only a little

larger than the 6.8 Å of a methylammonium lead iodide unit cell.[28] The anhydride should have some flexibility and degree of freedom to rotate around the anhydride. Molecules utilizing a 3,3'-dinitrobenzoicanhydride was synthesized inspired by Al-Azani et al., using an Appel type transformation to couple 3-nitrobenzoic acid.[40] The nitro groups will be converted to amino groups through a zinc catalyzed reduction inspired by Gowda et al., the straightforward procedure should prove to be advantageous.[41] The anhydride is ideal for IRRAS experiments due to its characteristic signal between 1780–1740 cm^{-1} and its vertical orientation with relation to the surface. We expect that the anhydride will be more rigid than the benzoic acid counterparts.

3.3.5. Basicity and halide site experiments

Samples were transferred from their inert environments to the Schlenk line in atmosphere-isolating flasks (e.g. Chemglass AF-0520). Cannula transfer of an ethereal BF_3 solution submerged individual wafer samples under an argon ambient at either 25 or 40 °C. Following either 5 min or 60 min exposures, the reagent solution was removed and wafers were rinsed via sequential submersions in diethyl ether. Samples were dried via evacuation. Under an air ambient the $MAPbI_3$ wafers were directly mounted on XPS sample pucks. Samples using the n-hexane/ DCM (v/v= 10:1) or toluene solvents were conducted at 40 °C with 1-, 15-, and 30-min exposures.

Cannula transfer of triphenylborane and tris(pentafluorophenyl)borane solutions submerged samples for one hour at 40 °C. The solutions were drained, wafers rinsed, and dried under vacuum. Under an air ambient the $MAPbI_3$ wafers were directly mounted on XPS sample pucks.

Samples were transferred from their inert environments to the Schlenk line in atmosphere-isolating flasks (e.g. Chemglass AF-0520). Cannula transfer of boric acid solutions submerged individual wafers at room temperature unless otherwise noted. The hexane mixtures were examined at 1,2,4 and 24-hour reaction times and the 2-hour reaction completed in parallel at 35 °C. The toluene mixture was examined at 1 hour. The anisole mixture was examined at 3 hours. Following the exposures, the solution was removed and the wafers were rinsed via sequential submersions in the corresponding solvent. Samples were dried via evacuation. Under an air ambient, $MAPbI_3$ wafers were expeditiously mounted and transferred to the XPS load-lock.

Solutions of 4-trifluoromethylphenyl boronic acid, pinacol ester were freshly freeze-pump-thawed prior to use and stored over sieves for greater than three days prior. Cannula transfer of the solution submerged individual wafers for 5 hours. The solution was removed and the wafers were rinsed via sequential submersions. Samples were dried via evacuation. The initial diethyl ether experiment utilized 10 mM at room temperature, subsequent experiments utilized 40 mM at reflux in ether and DCM, and finally 80 mM in refluxing chlorobenzene. Under an air ambient, $MAPbI_3$ wafers were expeditiously mounted and transferred to the XPS load-lock.

3.3.6. Ammonium Exchange experiments

Samples were transferred to reagent flasks as in the basicity study and submerged in the *p*-trifluoromethylanilinium chloride or 2-thiophene methylammonium chloride/hexafluorophosphate solution for one hour at 25 °C followed by rinsing in DCM, drying under vacuum, and sample mounting/transfer as described above. 2,2,2-

trifluoroethylammonium chloride was submerged for 30-minutes using both DCM and chlorobenzene.

Samples were submerged in the 4-ammonium benzoic acid chloride for 5 hours at room temperature followed by rinsing, drying under vacuum, and sample mounting/ transfer as mentioned above. IR studies utilized the Seagull attachment. This involved collecting background prior to the treatment in identical orientation before and after.

3.3.7. Metal Ligation

Coupling of 4-(trifluoromethyl)-2-bromopyridine yielded 4,4'-bis(trifluoromethyl)-2,2'-bipyridine via literature procedures.[38,39] Wafer transfer, exposure to the fluorinated-bpy compound, rinsing, and drying proceeded as above for 60 min exposures of $MAPbI_3$(100).

The post-reaction solution was examined by total reflectance x-ray fluorescence (TXRF) to measure lead content in solution before and after. A fresh solution of 4,4'-bis(trifluoromethyl)-2,2'-bipyridine in DCM was split into three fractions, one as a blank, one to use in a normal experiment, and one on crushed $MAPbI_3$.

3.3.8. X-ray Photoelectron Spectroscopy

A PHI5600 XPS system with a third-party data acquisition system (RBD Instruments, Bend Oregon) acquired all photoelectron spectra as detailed previously.[7] Analysis chamber base pressures were $<1 \times 10^{-9}$ Torr. A hemispherical energy analyzer that was positioned at 90° with respect to the incoming monochromated Al K_α X-ray flux and 45° with respect to standard sample positioning collected the photoelectrons. Survey spectra utilized a 117 eV pass energy, a 0.5 eV step size, and a 50-ms-per-step dwell

time. High-resolution XP spectra employed a 23.5 eV pass energy, 0.025 eV step size, and a 50 ms dwell time per step. Based on a consistent 285 eV position of features ascribed to adventitious carbon, acquisitions did not necessitate charge neutralization. Post-acquisition data fitting employed W-Tougaard-style baselines and GL(70) peak shapes for features within the I 3d; a Shirley-style baseline and GL(70) peak shape within the Pb 4f region; a W-Tougaard baseline and GL(30) peak shape for the N 1s region; and linear baselines with GL(30) peak shapes for B 1s, C 1s, F 1s, and O 1s regions. Fits that employ multiple peaks within a spectral region utilized identical fwhm values for each peak to minimize mathematically optimized but potentially chemically unrealistic fits.

3.3.9. Adsorption motifs and adsorbate coverages from overlayer models

Interpreting photoelectron data in terms of coverages requires assumptions of adsorption motifs and the associated parameters in substrate overlayer models. This section describes the overall model, its terms, and components, this is in contrast with the following sections which go into greater detail regarding the perovskite structure and its implications on the model. A substrate overlayer model converted photoelectron-determined peak area ratios to fractional monolayer coverage values for the reagent molecules that functionalized the $MAPbI_3$ surfaces.[42,43] Equation 1 models a fractional monolayer coverage, Φ, of a unique chemical overlayer, "Ov", of thickness d_{Ov} that is separated from a substrate, "Sub", by a thickness D.[44]

$$\frac{I_{\mathrm{Ov}}}{I_{\mathrm{Sub}}} = \frac{I_{\mathrm{Ov}}^{\infty}}{I_{\mathrm{Sub}}^{\infty}} \frac{\Phi\left(1-\exp\frac{-d_{\mathrm{Ov}}}{\lambda_{\mathrm{Ov,\,self}}\cos\theta}\right)}{1-\Phi+\Phi\exp\frac{-d_{\mathrm{Ov}}-D}{\lambda_{\mathrm{Sub,\,Ov}}\cos\theta}} \qquad (1)$$

The signal intensity from an ideal, pure, infinitely thick overlayer sample, I^{∞}_{Ov}, is attenuated due to only having fractional coverage, Φ, and being d_{Ov} thick, to yield the measured intensity from the overlayer, I_{Ov}. Electrons that are photogenerated in the overlayer are attenuated in travelling through the overlayer itself by $\lambda_{Ov,self} \cos \theta$, where θ represents the angle between the electron collection direction and the surface normal. The signal intensity from an ideal, pure, infinitely thick substrate, I^{∞}_{Sub}, is attenuated due to being partially obscured by the fractional monolayer coverage represented by the $\Phi \exp \ldots$ term, while the non-obscured substrate fraction, $1 - \Phi$, is not attenuated to cumulatively yield the measured intensity from the substrate, I_{Sub}. The exponential term in the denominator relies on substrate-generated electrons that travel through the overlayers of thickness d_{Ov} and D whilst being attenuated though the overlayers by $\lambda_{Sub,Ov} \cos \theta$. Note that eq 1 simplifies more explicit models by assuming assume a similar attenuation factor $\lambda_{Sub,Ov}$ for substrate photoelectrons travelling through the overlayer of interest, d_{Ov}, and the spacer, D.[42]

The ideal pure intensity terms may be disassembled and rearranged to better describe the specific systems under study. The intensity, I^{∞}, of a pure, homogeneous, clean material is given by $\rho f \sigma \phi y A T \lambda$ that includes the number density of measured atoms per unit volume, ρ; the x-ray photon flux in photons per area per time, f; the photoionization cross section in area per atom, σ; the instrument-specific angular detection efficiency, ϕ; the efficiency of photoelectron production, y; the sample detection area, A; the instrument-specific photoelectron detection efficiency, T; and the attenuation length of escaping photoelectrons, λ. The angle between the sample normal and the

detector, θ, is not explicitly included but is rather implied as the effective solid angle of detection scales with angle according to A / cos θ, while the electron attenuation length scales as $\lambda \cos \theta$.[45] In practice, we ignore f due to considering intensity ratios, and because the penetration depth for x-rays is significantly larger than the escape depth for photoelectrons, or $\lambda_{\text{x-ray}} \gg \lambda_{\text{photoelectron}}$.[43,45] Further, for each signal of interest, an instrument-specific, illumination-specific atomic sensitivity factor denoted SF collects terms $\sigma\phi yAT\lambda$.[46,47] This sensitivity factor should not be confused for a Scofield factor, an instrument-independent but illumination-specific photoionization cross section, which is approximately σy and normalized to a cross section such as C 1s or F 1s.[48] Thus $I^{\infty}_{\text{Ov}} = SF_{\text{Ov}} \rho_{\text{Ov}}$ for the overlayer signal intensity, and $I^{\infty}_{\text{Sub}} = SF_{\text{Sub}} \rho_{\text{Sub}}$ for the substrate signals.

One may further simplify the atom number density terms for both the overlayer and the substrate. The study functionalizes perovskites with fluorine-containing organic and borane molecules and quantifies experimental intensity ratios between F 1s and the halide, I $3d_{5/2}$ from the perovskite. Thus, $\rho_{\text{Ov}} = \rho_{\text{F}}$, and $\rho_{\text{Sub}} = \rho_{\text{X}}$ where the halide X is I for $MAPbI_3$. In the case of ρ_{X}, both perovskite structures contain three halide anions per cubic unit cell. Although $MAPbI_3$ possesses a tetragonal structure at room temperature, we use the cubic structure for simplification as there are three iodide anions in the 0.6311^3 nm^3 cubic unit cell,[28] which is approximately identical to the twelve iodide anions in the $0.88392 \times 0.88392 \times 1.26948$ nm^3 tetragonal unit cell.[49] (Recall that to a very good approximation, the tetragonal unit cell is a 45° rotation of the cubit unit cell with a and b sides that are $\sqrt{2}$ longer than the cubit unit cell while the c side is twice as thick). Therefore, we use $\rho_{\text{X}} = 3a_{\text{perov}}^{-3}$ were a_{perov} respectively refers to the 0.6311 nm length of

one side of a $MAPbI_3$ cubic unit cell.[28] For the fluorine overlayer, volumetric number density, ρ_F, each BF_3 molecule and *p*-trifluoromethylanilinium cation contains three fluorine atoms per monolayer molecule. We do not consider the six-fluorine-atom bpy as that ligand yields trace reactivity with methylammonium lead iodide. As included in the discussion section, we further assume an ideal, monolayer-complete bonding arrangement in which one BF_3 molecule forms a Lewis adduct with the halide in the AX layer of the (100) face of each ABX_3 perovskite. Recall that (100)-parallel layers alternatively have AX (*i.e.* methylammonium iodide) and BX_2 (*i.e.* PbI_2) stoichiometry for ABX_3 perovskites in both the cubic and the tetragonal phases relevant to the current study. We also assume an ideal, monolayer-complete bonding arrangement in which the anilinium cation completely replaces the A-type cation in the AX layer of a (100) face. Thus, for 100% monolayer coverage of one BF_3 molecule or anilinium cation per unit cell area of perovskite, $\rho_F = 3a_{perov}^{-2}d_F^{-1}$ where d_F is the thickness of the fluorine atoms in the monolayer. For clarification, we assume that the fluorine atoms are all contained in a layer d_{Ov} that is as thick as a fluorine atom itself, d_F, and that the fluorine layer is spaced away from the perovskite substrate by *D* due to the boron-iodide adduct bond in BF_3, or the height of the anilinium cation. As "real" surfaces do not possess 100% monolayer coverage, we collect the Φ in the numerator of eq 1 that we believe is better expressed with the fluorine density term considering that it attenuates 100% surface coverage densities. Thus, fractional coverage of the molecular overlayer would result in an attenuated density, or $\Phi\rho_F = \Phi 3a_{perov}^{-2}d_F^{-1}$. Equation 2 re-expresses eq 1 from terms above.

$$\frac{I_{\mathrm{F\,1s}}}{I_{\mathrm{X\,3d}}} = \frac{SF_{\mathrm{F\,1s}}}{SF_{\mathrm{X\,3d}}} \frac{\Phi\, d_{\mathrm{F}}^{-1}}{a_{\mathrm{perov}}^{-1}} \frac{1 - \exp\frac{-d_{\mathrm{F}}}{\lambda_{\mathrm{F,\,overlayer}}\cos\theta}}{1 - \Phi + \Phi\exp\frac{-d_{\mathrm{F}} - D}{\lambda_{\mathrm{X,\,overlayer}}\cos\theta}} \quad (2)$$

Equation S2 presents d_{F} and a_{perov} so as to keep overlayer terms collected in the numerator and substrate terms in the denominator. Equation 2 specifies the overlayer sensitivity factor term SF_{Ov} as $SF_{\mathrm{F\,1s}}$ referring to fluorine photoelectron signals and the substrate sensitivity factor SF_{Sub} as $SF_{\mathrm{X\,3d}}$ for I 3d from $MAPbI_3$. Further, eq 2 represents the characteristic attenuation lengths for photoelectrons generated in the overlayer and travelling through the overlayer, $\lambda_{\mathrm{Ov,self}}$, as $\lambda_{\mathrm{F,overlayer}}$ and represents photoelectrons generated in the substrate and travelling through the overlayer $\lambda_{\mathrm{Sub,Ov}}$, as $\lambda_{\mathrm{X,overlayer}}$. Lastly, eq E2 defines the ratio of experimentally determined peak-area-intensity values for fluorine photoelectrons in the overlayer, $I_{\mathrm{Ov}} = I_{\mathrm{F\,1s}}$, and that for halide photoelectrons from the substrate, $I_{\mathrm{Sub}} = I_{\mathrm{X\,3d}}$.

In practice, all parameters in eq 2 are known or must be estimated *a priori* to solve for Φ, the surface coverage of molecules comprising an adsorbate overlayer. In the present study, spectral analyses utilize the ratio of F 1s in fluorine-containing overlayers to either the I 3d signals from $MAPbI_3$. We use instrument-specific values of 1.000 and 5.337 for the respective F 1s and I $3d_{5/2}$ sensitivity factors.[47] An experimentally determined electron attenuation length for F 1s photoelectrons in poly(tetrafluoroethylene) determines $\lambda_{\mathrm{F\,1s}}$ = 2.05 nm that we use for both BF_3 and anilinium adlayers.[50] Equation E3 estimates $\lambda_{\mathrm{X,overlayer}}$ values based on an empirical model that relies on: **E**, the photoelectron kinetic energy; $\langle A \rangle$, the average atomic mass of

species in the overlayer in g mol^{-1}; ρ, the substrate density in kg m^{-3}; N, Avogadro's number; as well as $\langle Z \rangle$, the average atomic number of atoms in the overlayer.[51]

$$\lambda = 0.316 \times 10^{12} \left(\frac{\langle A \rangle}{\rho N} \right)^{1/2} \left[\frac{\mathbf{E}}{\langle Z \rangle^{0.45} \left(3 + \ln \frac{\mathbf{E}}{27} \right)} + 4 \right] \quad (3)$$

For I 3d photoelectrons, $\mathbf{E} \approx 863$ eV corresponding to Al K_α radiation, a 619 eV binding energy, and a ~4 eV instrument work function. For I 3d photoelectrons travelling through a BF_3 or *p*-trifluoromethylanilium overlayer, $\lambda_{I\ 3d,BF_3}$ = 2.92 nm, and $\lambda_{I\ 3d,anilinium}$ = 2.68 nm when 1050 kg m^{-3} density of bulk aniline estimates the density of the overlayer species. Attenuations were approximated by $\lambda_{I\ 3d,\ F_{15}\ C_{18}B}$ = 3.80 nm for tris(pentafluorophenylborane) and $\lambda_{I\ 3d,anilinium}$ = 2.10 nm for the 2,2,2-trifluoroethylammonium. For d_F, we approximate the height of a fluorine layer in CF_3 or BF_3 moieties from the cubic volume that occupies the same volume as a hard sphere given by the covalent radius of fluorine,[44] or $d_{Ov} = d_F = 2\sqrt[3]{\pi/6}\, r_F \approx 0.103$ nm.[52] For BF_3 overlayers, we approximate the spacing D by an aliphatic C – C length of 0.15 nm, two aliphatic and two aromatic carbon bond lengths yielded $D \approx 0.58$ nm for adsorbed *p*-trifluoromethylanilinium species, the approximate D spacing for 2,2,2-trifluoroethylammonium species is about 0.28 nm by estimating the aliphatic chain and in Gaussian calculations, and tris(pentafluorophenyl)borane yielded an approximate D thickness of 0.4 nm utilizing a Gaussian model to force a tetragonal structure. A *Mathematica* notebook solves for Φ with the parameters described above. As we observed no fluorine signal on $MAPbI_3$ (100) surfaces following a reaction with a

fluorinated bipyridyl compound, the presented overlayer models do not include the corresponding analyses. Adsorption on the (110) facet has been estimated.

3.3.10 Adsorption motifs and resulting photoelectron ratios on tetragonal $MAPbI_3(100)$ surfaces

Figure 2 presents a tetragonal $MAPbI_3(100)_t$ unit cell with a plane drawn in green through: A, the $(100)_t$ layer with $MA_2Pb_2I_2$ stoichiometry; and B, the $(100)_t$ layer with I_4 stoichiometry per tetragonal unit cell. Recall that for the $MAPbI_3$ tetragonal unit cell $a_{tetragonal} = b_{tetragonal} = \sqrt{2}a_{cubic} = 0.88392$ nm , $c_{tetragonal} = 2a_{cubic} = 1.26947$ nm, and contains four equivalents of $MAPbI_3$ (or $MA_4Pb_4I_{12}$).[28,49] It is also important to note as others have done, that the alternating layers in frames A and B respectively carry a net charge of 4+ and 4– elementary charges per unit cell. Considering the layer charges, it is unlikely that a "real" tetragonal $MAPbI_3(100)_t$ surface would present either of the idealized stoichiometric ratios in Fig. 2, however we will come back to this below.

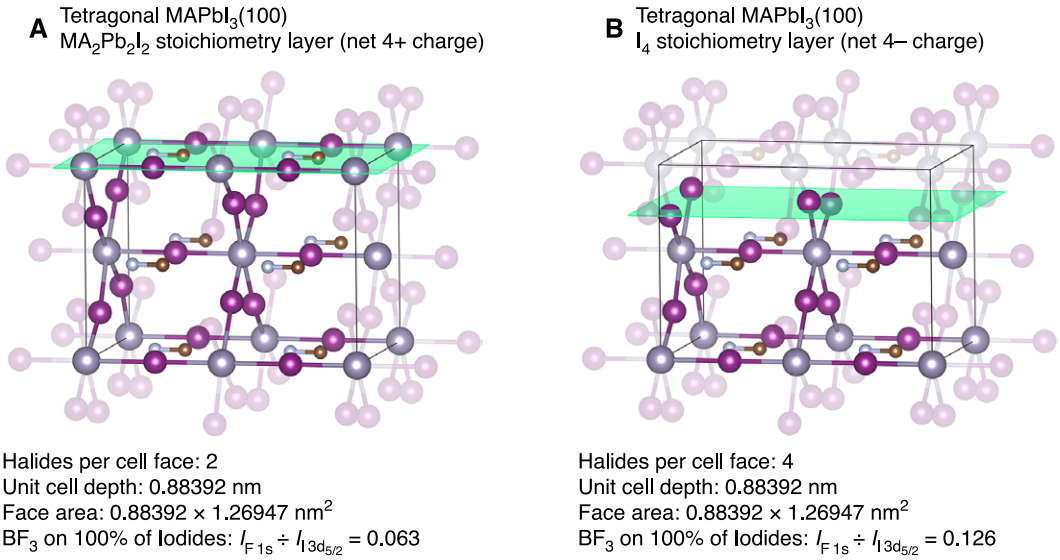

Figure 2. The surface density of interfacial halides within idealized, (100)-parallel layers on tetragonal $MAPbI_3$ vary between two halides per unit-cell face for the layer with $MA_2Pb_2I_2$ stoichiometry (frame A)

and four halides per unit-cell face for the layer with I_4 stoichiometry (frame B). The purple sphere is iodide, the lead is gray, carbon is blue, and nitrogen is brown. Hydrogen atoms are omitted for clarity.

For the two idealized layers on tetragonal $MAPbI_3(100)_t$, we can now reduce and express the $\rho_F \div \rho_I$ ratio. For a layer with $MA_2Pb_2I_2$ stoichiometry à la Fig. 2A, there are two halide atoms per unit cell face. If both of these two halide atoms per unit cell area each had one adsorbed BF_3 molecule above them, then there would be six fluorine atoms per unit cell area. Recognizing that the areas are the same, we can divide the common area out from both ρ_F and from ρ_I. Dividing the perovskite unit cell volume by the area yields the unit cell height and dividing the volume of the fluorine atoms in the BF_3 layer by the area of the unit cell yields the height of a fluorine atom, d_F. Thus, for 100% BF_3 coverage of every iodide anion in a layer such as Fig. 2A where there are 12 iodide anions per unit cell volume, $\rho_F \div \rho_I$ reduces to $d_F^{-1} / \sqrt{2} a_{cubic}^{-1}$ and eq 1 may be simplified as eq 2. Equation 4 collects the Φ in the numerator that is perhaps best expressed with the fluorine density terms, and we include the reciprocals as such to keep overlayer terms in the numerator and substrate terms in the denominator.

Per Fig. 2A:

$$\frac{I_{F\,1s}}{I_{I\,3d_{5/2}}} = \frac{SF_{F\,1s}}{SF_{I\,3d_{5/2}}} \frac{\Phi\, d_F^{-1}}{\sqrt{2} a_{cubic}^{-1}} \frac{1 - \exp \frac{-d_F}{\lambda_{F,\,overlayer} \cos\theta}}{1 - \Phi + \Phi \exp \frac{-d_F + D}{\lambda_{I,\,overlayer} \cos\theta}} \qquad (4)$$

Equation 4 specifies the overlayer sensitivity factor term SF_{Ov} as $SF_{F\,1s}$ referring to fluorine photoelectron signals and the substrate sensitivity factor SF_{Sub} as $SF_{I\,3d_{5/2}}$.

For the coverage of BF_3 molecules if the surface termination were idealized in the fashion of Fig. 2B the analysis follows a similar methodology for Fig. 2A and eq 4. In Fig. 2B there are four halide atoms per unit cell area, so for 100% coverage, ρ_F would double but ρ_I remains 12 iodide anions per unit cell volume. Thus, the $\rho_F \div \rho_I$ ratio would double

relative to the case in Fig. 2A, and we utilize eq 5 to represent fractional fluorine coverages if BF_3 molecules adsorbed to an idealized Fig. S1B surface.

Per Fig. 2B:

$$\frac{I_{\mathrm{F\,1s}}}{I_{\mathrm{I\,3d_{5/2}}}} = \frac{SF_{\mathrm{F\,1s}}}{SF_{\mathrm{I\,3d_{5/2}}}} \frac{\Phi\sqrt{2}\,d_{\mathrm{F}}^{-1}}{a_{\mathrm{cubic}}^{-1}} \frac{1-\exp\frac{-d_{\mathrm{F}}}{\lambda_{\mathrm{F,\,overlayer}}\cos\theta}}{1-\Phi+\Phi\exp\frac{-d_{\mathrm{F}}+D}{\lambda_{\mathrm{I,\,overlayer}}\cos\theta}} \quad (5)$$

As mentioned above parallel layers of idealized, tetragonal $MAPbI_3(100)$ carry net charges as revealed by the different layer stoichiometries in Fig. 2 and this may yield different surface halide ratios and concomitant BF_3 adsorption. We assume that the certain species are added to or dropped from a particular layer with a concomitant rearrangement in bonding and electronic structure. We believe that it is reasonable to assume that the topmost layer would contain the methylammonium cation as this species can have a surfactant-like effect that should lower the overall surface energy. Thus, our idealized picture for a charge-neutral tetragonal $MAPbI_3(100)_t$ surface may qualitatively result in loss of interfacial Pb^{2+} from a surface terminated in a Fig. 2A layer or perhaps increase methylammonium species on a surface terminated as per Fig. 2B. The charge neutralized tetragonal $MAPbI_3(100)_t$ surface may likely be a chemical average of the two idealized layers in Fig. 2 with some number of halide ions per unit cell area that is bounded by a minimum of two and a maximum of four. At best, we can broadly speculate as to these averages, and we further introduce eq 6 that represents a middle value between the extremes of eq 4 and 5 for the estimated photoelectron spectroscopic ratio for BF_3 adsorbed onto a tetragonal $MAPbI_3(100)_t$ surface:

"Average" adsorption on charge-neutral

$$\frac{I_{\mathrm{F\,1s}}}{I_{\mathrm{I\,3d_{5/2}}}} \approx \frac{SF_{\mathrm{F\,1s}}}{SF_{\mathrm{I\,3d_{5/2}}}} \frac{\Phi\,d_{\mathrm{F}}^{-1}}{a_{\mathrm{cubic}}^{-1}} \frac{1-\exp\frac{-d_{\mathrm{F}}}{\lambda_{\mathrm{F,\,overlayer}}\cos\theta}}{1-\Phi+\Phi\exp\frac{-d_{\mathrm{F}}+D}{\lambda_{\mathrm{I,\,overlayer}}\cos\theta}} \quad (6)$$

tetragonal

$MAPbI_3$(100):

Next, we consider adsorption motifs and BF_3 packing densities on other faces of perovskite crystals relevant to the experimental studies.

3.3.11. Adsorption comparison on tetragonal (001), (110), and cubic (100) $MAPbI_3$ faces

We consider together the adsorption of BF_3 on tetragonal (001), tetragonal (110), and cubic (100) faces of $MAPbI_3$, as they follow generally similar structures and ultimately yield a mutually identical functional form for the overlayer model.

Figure 3 explores layer arrangement, stoichiometries, and halide surface densities both for tetragonal (001) and for tetragonal (110) in frames A and B, and for cubic (100) in frames C and D. Of note, the tetragonal (110) face bears strong structural resemblance to the tetragonal (001) with only modest repositioning of the iodide anions. Importantly and in contrast to the tetragonal (100) faces in Fig. 2, each unique layer denoted in green in Fig. 3 is charge neutral.

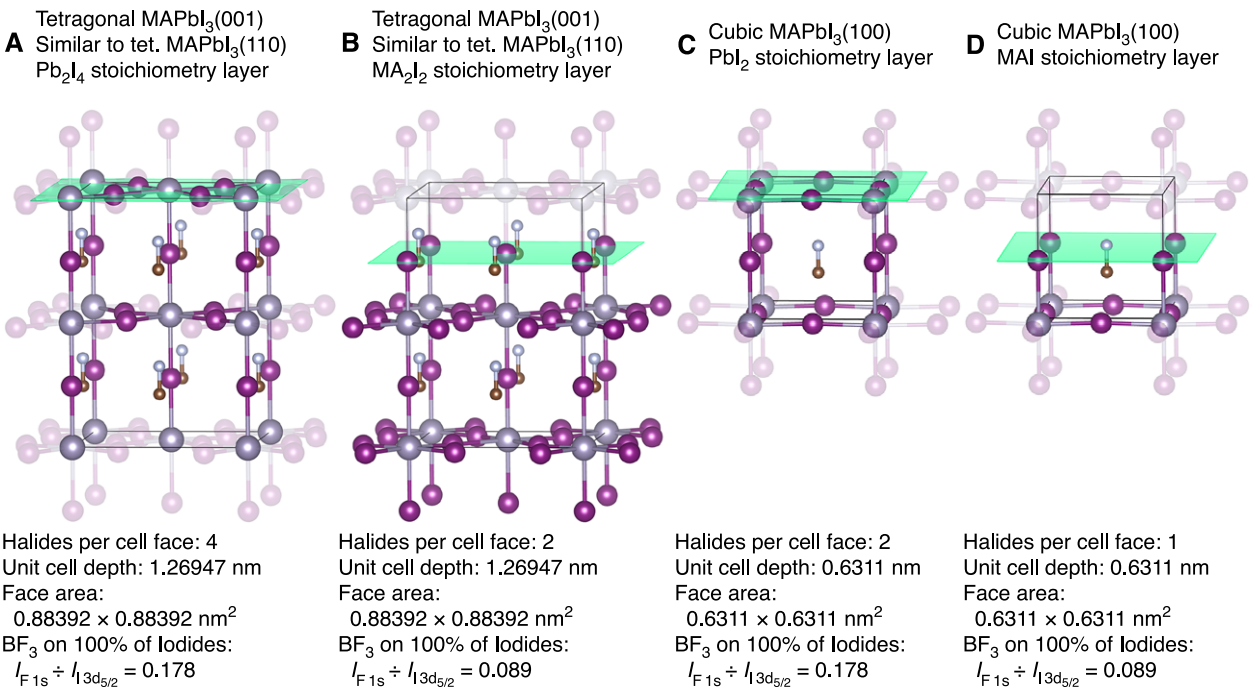

Figure 3. The surface density of interfacial halides within idealized layers for **A**, a tetragonal $MAPbI_3$(001) layer with four halide atoms per unit cell area; **B**, a tetragonal $MAPbI_3$(001) layer with two halide atoms per unit cell area; **C**, a cubic $MAPbI_3$(100) layer with two halide atoms per unit cell area; and **D**, a cubic $MAPbI_3$(100) layer with one halide atoms per unit cell area. Notably, the atomic arrangement and shape of tetragonal ("tet.") (110) faces are very similar to those of tetragonal (001) with only modest repositioning of the iodide anions. All layers are charge neutral with hydrogen atoms omitted.

Analyses of the iodide packing reveals idealized fluorine-to-iodide photoelectron intensity ratios for BF_3 adsorbed to surface-available iodide for each frame of Fig. 3 as above. For the tetragonal (001) in frame A with a surface layer of Pb_2I_4 stoichiometry, adsorption of one BF_3 molecule to each of the four halide anions would yield 12 F atoms per unit cell area for the 12 I^- per unit cell volume. As above, the unit cell areas can cancel out and the $\rho_F \div \rho_I$ ratio from eq 2 reduces to the term $2d_F^{-1}/a_{cubic}^{-1}$ to yield eq 7. For eq 7, recall that the *c* height of the unit cell in Fig. 3A–B is $2a_{cubic}$.

Per Fig. 3A:
$$\frac{I_{\mathrm{F\,1s}}}{I_{\mathrm{I\,3d_{5/2}}}} = \frac{SF_{\mathrm{F\,1s}}}{SF_{\mathrm{I\,3d_{5/2}}}} \frac{\Phi\, 2d_{\mathrm{F}}^{-1}}{a_{\mathrm{cubic}}^{-1}} \frac{1-\exp\frac{-d_{\mathrm{F}}}{\lambda_{\mathrm{F,\,overlayer}}\cos\theta}}{1-\Phi+\Phi\exp\frac{-d_{\mathrm{F}}+D}{\lambda_{\mathrm{I,\,overlayer}}\cos\theta}} \quad (7)$$

If tetragonal $MAPbI_3$(001) terminates in a layer with MA_2I_2 stoichiometry there would be two iodide anions for possible adsorption by BF_3. In this case, 100% coverage of BF_3 on each surface available iodide site would yield six fluorine atoms per unit cell area, and the $\rho_F \div \rho_I$ ratio would reduce to $d_{\mathrm{F}}^{-1}/a_{\mathrm{cubic}}^{-1}$ and eq 8 would describe the fluorine surface coverage.

Per Fig. 3B:
$$\frac{I_{\mathrm{F\,1s}}}{I_{\mathrm{I\,3d_{5/2}}}} = \frac{SF_{\mathrm{F\,1s}}}{SF_{\mathrm{I\,3d_{5/2}}}} \frac{\Phi\, d_{\mathrm{F}}^{-1}}{a_{\mathrm{cubic}}^{-1}} \frac{1-\exp\frac{-d_{\mathrm{F}}}{\lambda_{\mathrm{F,\,overlayer}}\cos\theta}}{1-\Phi+\Phi\exp\frac{-d_{\mathrm{F}}+D}{\lambda_{\mathrm{I,\,overlayer}}\cos\theta}} \quad (8)$$

In the case of BF_3 adsorption onto cubic $MAPbI_3$(100) faces, Fig. 3C–D present two possible layers with PbI_2 stoichiometry in frame C, and methylammonium iodide stoichiometry in frame D. If BF_3 adsorbed to each of the two iodide anions at the surface in frame C, the density $\rho_F \div \rho_I$ ratio would reduce $2d_{\mathrm{F}}^{-1}/a_{\mathrm{cubic}}^{-1}$ considering six fluorine atoms in the unit cell area and three iodide anions in the cubic unit cell volume. Thus, eq 9 describes the photoelectron ratio if BF_3 adsorbs to a PbI_2-termianted, cubic $MAPbI_3$(100) surface as in Fig. 3C, which is the same as eq 6.

Per Fig. 3C:
$$\frac{I_{\mathrm{F\,1s}}}{I_{\mathrm{I\,3d_{5/2}}}} = \frac{SF_{\mathrm{F\,1s}}}{SF_{\mathrm{I\,3d_{5/2}}}} \frac{\Phi\, 2d_{\mathrm{F}}^{-1}}{a_{\mathrm{cubic}}^{-1}} \frac{1-\exp\frac{-d_{\mathrm{F}}}{\lambda_{\mathrm{F,\,overlayer}}\cos\theta}}{1-\Phi+\Phi\exp\frac{-d_{\mathrm{F}}+D}{\lambda_{\mathrm{I,\,overlayer}}\cos\theta}} \quad (9)$$

Lastly, if BF_3 adsorbed to the lone iodide anions at the surface in frame D, the density $\rho_F \div \rho_I$ ratio would reduce to $d_{\mathrm{F}}^{-1}/a_{\mathrm{cubic}}^{-1}$. Thus, eq 10 describes the photoelectron ratio if BF_3 adsorbs to a MAI-terminated, cubic $MAPbI_3$(100) surface as in Fig. S2D, which is the same as eq 7.

Per Fig. 3D:

$$\frac{I_{\mathrm{F\,1s}}}{I_{\mathrm{I\,3d_{5/2}}}} = \frac{SF_{\mathrm{F\,1s}}}{SF_{\mathrm{I\,3d_{5/2}}}} \frac{\Phi\, d_{\mathrm{F}}^{-1}}{a_{\mathrm{cubic}}^{-1}} \frac{1 - \exp\frac{-d_{\mathrm{F}}}{\lambda_{\mathrm{F,\,overlayer}}\cos\theta}}{1 - \Phi + \Phi\exp\frac{-d_{\mathrm{F}}+D}{\lambda_{\mathrm{I,\,overlayer}}\cos\theta}} \qquad (10)$$

Considering the potential surfactant effect of methylammonium species, we believe that the most likely surface terminations are those of Fig. 3B for tetragonal (001) and for tetragonal (110), and Fig. 3D for cubic (100). Thus eqs 8 and 10 likely are the best description for these pseudo-cubic cases.

3.3.12. Interpretation of adsorption motifs and implications for photoelectron spectra

Mentioned above, the tetragonal $MAPbI_3$(100) layers carry alternating charges, and "real" surfaces would rearrange to reach charge neutrality. We posit that eq 6 best represents the ratio of fluorine-to-iodine photoelectron intensities for a charge-neutral but still atomically flat tetragonal $MAPbI_3$(100) surface. It is notable that the functional approximation of eq 6 is identical to the assigned surface coverage equations in eq 8 and 10 that best represent adsorption motifs for BF_3 on the pseudo-cubic faces.

In analyses of adsorption in the manuscript, we utilize eq 10 to interpret the overlayer coverages of BF_3 and of the *p*-trifluoromethyl anilinium cation.

Considering the bonding motifs introduced above, the substrate overlayer model may be solved for 100% coverage values based on experimentally determined peak area ratios. Sub- and super-monolayer coverages are not linear with changes in peak area ratios due to the exponential terms in eqs 1,2,4—10, but comparisons remain qualitatively illustrative and insightful. For bonding motifs associated with BF_3 adsorption on tetragonal $MAPbI_3$(100), eq 4 calculates $I_{\mathrm{F\,1s}} / I_{\mathrm{I\,3d_{5/2}}} = 0.063$ for one BF_3 adsorbed to each of the two exposed halides in Fig. 2A, and eq 4 determines $I_{\mathrm{F\,1s}} / I_{\mathrm{I\,3d_{5/2}}} = 0.126$ for one

adsorbed BF_3 for each of the four exposed halides in Fig. S1B. Due to the surfaces in Fig. 2 carrying a net charge, we use eq 6 to approximate BF_3 coverage on a charge neutral tetragonal $MAPbI_3$(100) surface where $I_{F\ 1s} / I_{I\ 3d_{5/2}} = 0.089$. Notably, the result from eq 6 is not precisely the average of the results from eqs 4–5, however this difference is concomitant with the uncertainty of the exact chemical speciation on tetragonal $MAPbI_3$(100) surfaces that this manuscript aims to elucidate. The pseudo-cubic but actually tetragonal (001) and tetragonal (110) faces in that terminate in methylammonium iodide in Fig. 3B and the actual cubic face with similar termination in Fig. 3D follow the mutually identical eq 8 and 10 formulae. Those equations predict that "complete" BF_3 adsorption to surface-available halides would experimentally yield $I_{F\ 1s} / I_{I\ 3d_{5/2}} = 0.089$, which is the same ratio that we expect in the tetragonal case. Thus, when discussing in the manuscript the BF_3 adsorption and fractional coverage on real tetragonal $MAPbI_3$(100) surfaces, we use the eq 6/8/10 form that quantifies 100% adsorption as yielding $I_{F\ 1s} / I_{I\ 3d_{5/2}} = 0.089$. The cubic approximation using the tetragonal surface is used as the approximation for the $(110)_t$ and $(112)_t$ preliminary experiments.

For *p*-trifluoromethylanilinium cations exchange, a similar analysis follows to the aforementioned analysis for BF_3 adsorption. We expect that the surfaces under study are charge neutral, and assuming a greater surface partitioning would exist for the surfactant-like methylammonium cation as opposed to the pseudo-hard-sphere Pb^{2+} cation. We assume that there are an equal number of methylammonium cations at any single-crystal surface of $MAPbI_3$ to the surface density of iodide anions and that we can thusly employ eqs 6/8/10 to describe the surface coverages for interfacial anilinium

exchange. In those cases we take D = 0.578 nm under the further assumption that the molecule is "standing" aligned with the surface normal. Considering that model, we take a F 1s-to-I 3d peak area ratio of 0.11 as representing 100% exchange of methylammonium on $MAPbI_3(100)_t$. The $(110)_t$ surface did not yield a strong fluorine signal after ammonium exchange unlike the $(100)_t$ surfaces.

3.3.13. Temperature Programmed Desorption

TPD experiments utilize an in-house-modified chamber affixed onto the PHI5600 analysis chamber that is separately turbopumped and isolated from the XPS as needed. A longitudinal transfer arm enables transfer of Phi-style sample pucks from the XPS analysis chamber to a stage within the TPD chamber. Experiments utilize custom-fabricated sample pucks that mimic the shape of the Phi instrument pucks but were fabricated from molybdenum and contain a resistive heating element within the puck body (HeatWave Labs, Inc., Watsonville, CA). Passing current through electrical connections from the sample stage to connections on the custom pucks affords sample heating. The TPD stage raises the custom puck to within 5 mm of the entrance grid of a mass spectrometer. Specific positioning of a K-type, 30-gauge thermocouple enables intimate mechanical contact with the top face of the custom puck for temperature measurements. A 1–200 amu quadrupole mass selector with a 70-eV, electron-impact ionization source and channel-electron multiplier (channeltron) serves as the mass spectrometer (RGA200, Stanford Research Systems, Sunnyvale CA). An in-house designed, LabVIEW-based program acquires mass spectra as a function of time while concurrently controlling a power supply (PGM-2010, GW Instek, New Taipei City, Taiwan) to yield a linear heating

rate of 0.33 K s^{-1}. During heating of BF_3-functionalized perovskites, the mass spectrometer quantifies the intensity of species desorbing at 48, 49, 50 and 51 m/z. The particular masses under observation result from the principal 70 eV electron impact ionization product of BF_3 being BF_2^+,[53] and the associated mass-to-charge values of 48 *m*/*z* corresponding to $^{10}BF_2^+$, 49 *m*/*z* corresponding to $^{11}BF_2^+$, and others serving as a control trace corresponding to no expected desorption products.

Following Redhead, eq. 11 models relates the desorption profile to an interaction energy between the adsorbate and the surface.[54]

$$-\frac{\mathrm{d}N}{\mathrm{d}T} = A\,N^n \beta^{-1} \exp\frac{-E_\mathrm{a}}{RT} \qquad (11)$$

Equation 4 utilizes the surface density of adsorbed species *N*, desorption order *n*, sample temperature *T*, heating rate *β*, and gas constant *R*. Assuming first-order desorption, model parameters include an Arrhenius-like preexponential factor, *A*, that we estimate as 1×10^{13} s^{-1} due to first-order desorption;[21] and an Arrhenius-like activation energy for desorption, E_a. As an experimentally determined mass intensity vs temperature plot should be proportional to –d*N*/d*T*, simulated desorption traces with parameterized E_a values estimate the activation energy for desorption rather than strict fits as employed in photoelectron spectroscopy.

3.3.14. Scanning Electron Microscopy

Scanning Electron Microscopy was conducted using a JEOL JSM-7000F field emission scanning electron microscope (JEOL Ltd., Akishima, Tokyo, Japan). Spectra were collected using a 4.0 kV for the methylammonium lead iodide perovskites. The low voltages were used to minimize beam damage in the organic-containing perovskite.

Samples were mounted vertically and horizontally on a sample puck using conductive copper tape, double-sided adhesive (3M).

3.3.15. Infrared Reflection Absorbance Spectroscopy

The surfaces functionalized with the carboxylic acids were examined using Infrared reflection absorption spectroscopy (IRRAS). IRRAS is a surface sensitive IR technique that can be used to discern the presence and orientation of a molecule or species on surfaces.[55,56] Data was collected on a Vertex 70 IR (Bruker) equipped with a variable angle reflectance IR attachment(Harrick, Auto-seagull, Pleasantville, NY). A liquid nitrogen cooled mercury-cadmium-telluride (MCT) detector was used in all experiments. Data was collected with both s and p polarized light at each angle. In IRRAS, it is important to utilize identical sample orientation for the background and data scans.

3.3.16. Synthesis of Grignard for substituted fluorophenyl boranes

Synthesis of tris(fluorophenyl) boranes is a promising avenue to further quantify the interaction strength of halides at the surface. All glassware used in this synthesis was loaded into the glovebox while hot, and sealed in the glovebox. 1.205 g of magnesium was ground and treated with four drops of lithium aluminum hydride to expose fresh metallic magnesium. Diethyl ether (10 ml) was added to the magnesium. An addition funnel was loaded with 5-bromo-1,2,3-trifluorobenzene (0.6 ml) and diluted with 10 ml diethyl ether. The magnesium-ether solution was cooled to 0 °C in an ice bath. The 5-bromo-1,2,3-trifluorobenzene was added extremely slowly at up to 4 drops per minute. The transfer took over an hour, during which the solution darkened. The reaction was allowed to proceed for one hour. During this time, a three-neck round bottom flask was

prepped with a septum, reflux condenser, and a stopcock. Toluene (5 ml) and BF_3 etherate solution (0.318 ml) were added and freeze-pump-thawed three times to degas. After one hour, a 0.2 ml aliquot of the Grignard reaction was reacted over dry ice to produce the carboxylic acid for ESI-MS analysis. Approximately half of the volume of the Grignard reaction solvent was removed under reduced pressure in a secondary cold trap. The Grignard solution was transferred via canula to the BF_3-toluene flask with the reflux condenser active. The water bath was heated to boiling to ensure 100 °C consistently. Additional hot water to replace the volume lost due to boiling was kept on hand at all times. The reaction mixture changed from a yellow color to black.

Purification proved to be challenging. Initially hot hexane was used to extract the nonpolar components. This yielded a golden yellow solution, leaving behind dark brown-black oils/solids. When the hexane solution was submerged in an ice bath nothing was observed. When submerged in a dry ice acetone bath, brown solids formed on the base and white solids formed on the walls of the flask above the hexane.

The second reaction may be the source of error in the procedure, the temperature (100 °C) was not as consistent as intended. The toluene used was considered “dry” since it was purchased as a dry solvent over sieves, but it was not specifically prepped to ensure dryness. In the purification steps, reduce the volume to improve crystallization. ESI-MS analysis of the Grignard reagent was compelling for successful synthesis.

Future synthesis attempts may take advantage of another synthetic strategy published after this was attempted found in Soltani et al..[57]

3.3.17. Computational Modeling

Methylammonium lead iodide pseudocubic perovskites were computationally explored using the Vienna Ab-Initio Simulation Package (VASP) to learn more about the perovskite structure and its interactions with adsorbates. The work done thus far has been able to uncover preliminary parameters for the $MAPbI_3$ structure inputs. The initial end goal of this experiment is to provide additional support to the iodine-boron interaction in $MAPbI_3$ surfaces. This would also provide additional support for different halide compositions and adsorbates in a straightforward manner. VASP is accessed through the terminal in MacOS or linux or PuTTy on Windows computers. Windows computers also need a SSH client to log into the WPI Turing computer cluster. The software uses the command line, there are many online sources for how to operate the command line if one is unfamiliar with using it. The initial parameters for the fundamental calculations were examined and suitable values were determined. The parameters that were examined included the E_{cut} which is the kinetic energy cutoff in electron volts for the system, higher cutoff values are “better” but increase the computational cost. The ideal E_{cut} is identified when the ΔE is less than 0.1 but greater than 0.05. The k-points are the dimensions of the system in inverse space. The important user defined components in VASP include the POSCAR, INCAR, KPOINTS, and POTCAR files. The POSCAR contains the position parameters for the system for one unit cell in either absolute (cartesian) or relative (direct) units. POSCAR files can be generated in the proper format in VESTA. The INCAR contains the input parameters. This contains variables and most have not yet been modified for these preliminary tests.

The important parameters to investigate are E_{cut} for the system energy cutoff, IVDW for the dispersion force influence, and ISPIN to model if electron spin is significant in the system. It is a good practice to utilize input files that are known to work and modify them for the experiment of interest. KPOINTS define the system in inverse space. The number of points effectively breaks the system into smaller sections. This enables "better" results, but significantly increases computational cost. These are changed with respect to the importance of that dimension in the system, balanced with computational cost and favorable energy results. The POTCAR input models the valence electrons with a defined core. The data is written to the OUTCAR file and can be accessed by viewing it. The calculation is complete when the line "reached required accuracy" and has been completed in the job queue. If the "reached required accuracy" is not present, the calculation is invalid and needs to be refined or changed to allow the calculation to

eV cut-off	energy without entropy (eV)
550	-50.75402
525	-50.75176
500	-50.72342
475	-50.72342
450	-50.72216
400	-50.73228
350	-50.63271
300	-50.52150
250	-50.21488
200	-49.63414
150	-45.08510
100	71.68040
50	292.64993

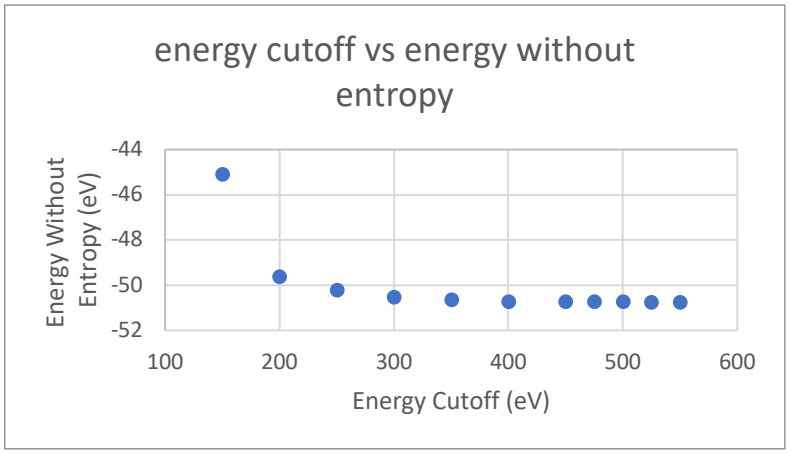

Figure 4. Energy cutoff value versus energy without entropy for the first set of experiments. The energy drops sharply as it approaches 300 eV and levels out by 400 eV. After 400 eV, the change between each step is marginal. 100 and 50 eV were omitted from the graph.

converge. Convergence is the term used to describe the energetic trend of the calculation as it approaches a ΔE of zero. The energy value of interest is “energy without entropy”.

The initial parameters that give the best overall energy without entropy and computational efficiency is a cutoff value of 450 eV, KPOINTS of 444, and lattice parameter of 6.45 Å. The first cutoff experiments used a KPOINTS parameter of 333, ands lattice parameter of 6.15 Å. The data supporting the first experiment yielding the optimal 400 eV cutoff can be seen in Figure 4.

Using the identified value of 400 eV as the cutoff energy, the KPOINTS were examined to determine that 444 will provide the best balance of computational quality, efficiency, and energy. The data for this experiment is in Table 1.

K-points	Energy without entropy (eV)
111	-54.40202
222	-51.32759
333	-50.73281
444	-50.73281
555	-50.70413
666	-50.69785

Table 1. The K-points for the MAPbI3 pseudocubic perovskite utilizing the 400 eV cutoff from the prior experiment. When making the decision to go with the 444 k-points, the overall time of the calculation and

The energy cutoff was again examined with the new k-point parameter of 444 to confirm if 400 eV was still optimal. 450 eV was confirmed as being an acceptable cutoff parameter after this experiment. The second cutoff experiment data can be seen in Figure 5.

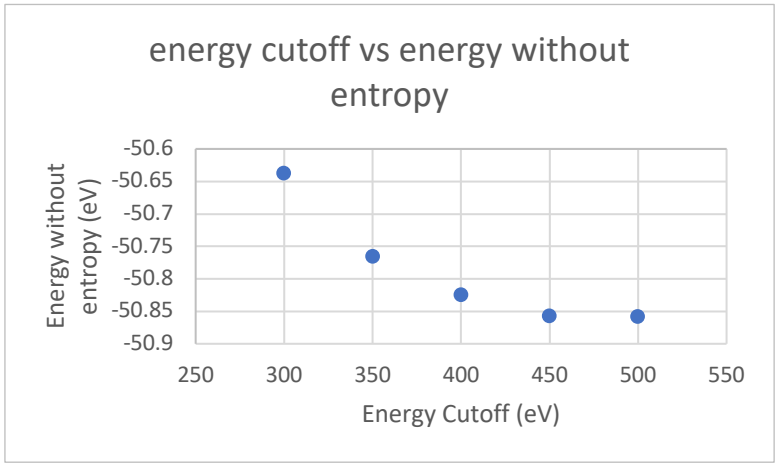

eV cut-off	Energy without entropy (eV)
300	-50.63688
350	-50.76482
400	-50.82422
450	-50.85695
500	-50.85756

Figure 5. The energy cutoff was examined again after choosing a new k-point parameter. Using the new parameter, 450 eV appears to be a better cutoff.

The final experiment that was completed was done to examine the lattice parameter of the sample. The standard lattice value from the crystal structure was varied in 0.1 Å increments with a range of ±0.7 Å. Contrary to the expected result, 6.45 Å is the optimal lattice parameter for the selected inputs. The data for the lattice optimization can be seen in Figure 6.

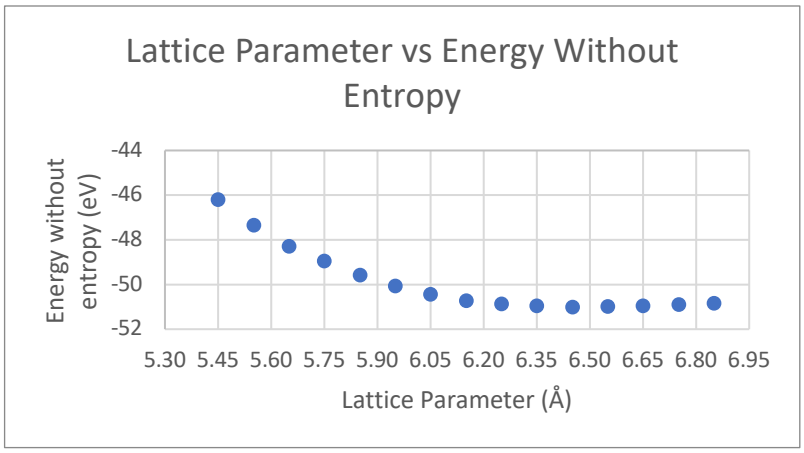

Figure 6. The lattice optimization was done using a 400 eV cutoff and a k-points parameter of 444. The experiment shows that 6.45 Å produces the minimum on the curve.

Lattice Parameter (Å)	Energy without entropy (eV)
5.45	-46.20822
5.55	-47.36657
5.65	-48.30639
5.75	-48.96446
5.85	-49.59267
5.95	-50.07945
6.05	-50.44656
6.15	-50.73330
6.25	-50.89050
6.35	-50.97556
6.45	-51.01399
6.55	-51.00349
6.65	-50.96310
6.75	-50.91356
6.85	-50.86291

These experiments can be repeated to learn the methods and confirm the results. The next steps following optimization is to create a tetrahedral BF_3 molecule and compare the energy without entropy values of the bare surface, lone BF_3 molecule, and a surface with BF_3 bonded to the iodine at varying distances. This will help to gain a greater understanding of the energetics at the surface and to provide additional support to the desorption energy experiments.

In addition to introductory VASP calculations, Gaussian calculations were performed using the WPI Solar-9 server through the WebMO web browser interface. WebMO is a user friendly, simple to pick up method of generating jobs for computational modeling. This can be used in numerous occasions to help support a hypothesis or visualize a challenging concept. Within WebMO, IR calculations are incredibly valuable from a qualitative standpoint to see relative intensities of different absorption modes along with animations for visualization.

3.3.18. Single Crystal Synthesis Using Perfluorooctyl Silane Coated Glassware

The use of perfluorooctyl silanes to functionalize the glassware is an attractive concept for the growth of large, high-quality single crystal perovskites. The procedure for functionalizing glassware still requires optimization and refinement. Up until now, solutions between 1 and 50 mM in ethanol and methanol have been examined using perfluorooctyl silanes (trichloro(1H,1H,2H,2H-perfluorooctyl)silane and 1H,1H,2H,2H-perfluorooctyltriethoxysilane). These two silanes are chemically similar, care should be used when diluting the chlorinated silane due to the evolution of hydrochloric gas and heat. The glassware is prepared with a thorough piranha cleaning and dried in an oven. The glassware is filled with the silane solution, covered tightly with aluminum foil, and allowed to sit overnight. The solution is drained and the glass is thoroughly rinsed. A drop of water should readily bead up due to the hydrophobic nature of the functionalization.

The functionalization does not however appear to be compatible with perovskite growing conditions with the inverse temperature GBL solution-based method. This may be due to the high temperature in combination with the nature of GBL being an extremely

effective solvent for “greasy” substances. There appears to be significant fluorine contamination in perovskites examined using XPS following synthesis with fluorosilane functionalized glassware. The single crystal quality and size are significant benefits to this method, but contamination is not permissible. XP spectra of a perovskite synthesized using the fluorocarbon glassware can be seen in Figure 7.

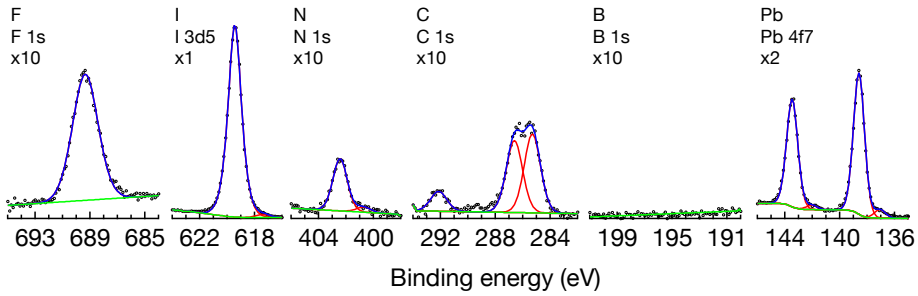

Figure 7. XP spectra of a perovskite using fluorosilane functionalized glassware. There is a significant fluorine signal and an easily identifiable signal at about 292 eV in the carbon spectrum indicative of fluorinated carbon species.

Chapter 4. Determination of the Surface Species of Tetragonal $MAPbI_3$ (100)

This chapter details the results of the fundamental studies on the tetragonal methylammonium lead iodide $(100)_t$ surface. The topics covered in this chapter detail the results of the BF_3 adsorption on the halide, TPD desorption of the BF_3, ammonium exchange with the *p*-trifluoromethyl anilinium, and 4,4'-bis(trifluoromethyl)-2,2'-bipyridine ligation studies for exposed lead at the surface.

4.1. BF_3 Adsorption

X-ray photoelectron spectroscopy quantifies the presence of fluorine on $MAPbI_3$(100) surfaces following exposure to an ethereal BF_3 solution. No attempt was made via heating or ion sputtering to minimize signals at 284.8–285.0 eV ascribed to adventitious carbon adsorption. Figure 8 presents the F 1s, I $3d_{5/2}$, N 1s, C 1s, B 1s, and Pb 4f regions of characteristic photoelectron spectra for a $MAPbI_3(100)_t$ face following a 60 min 40 °C exposure to the BF_3 solution (frame A, top); spectra following a 5 min, 25 °C exposure (frame B), and a face with no BF_3 exposure (frame C, bottom). For both the BF_3-exposed and non-exposed $MAPbI_3(100)_t$ samples in Fig. 6, the I 3d, N 1s, C 1s, and Pb 4f spectral regions resemble previously reported photoelectron spectra of methylammonium lead iodide surfaces. Scans quickly acquired data in the Pb 4f region to minimize beam-damage-induced observation of Pb^0 features, however some spectra demonstrate a small quantity of low-binding-energy features as in the Pb 4f region of frame C. Importantly for the adsorption models discussed below, the Pb 4f region demonstrates no quantifiable feature towards higher binding energy that could be ascribable to highly oxidized lead cations. O 1s spectra corresponding to each Pb 4f region demonstrate no features ascribable to metal oxides (not shown). Unique to the BF_3-exposed surface in frames A and B, we ascribe the feature at ~687 eV to BF_3 adsorption that is absent in the F 1s region for frame C and well matches that from prior

reports of BF_3-containing compounds.[51] The 1:3 boron-to-fluorine atom ratio, a 0.159:1 boron-to-fluorine sensitivity factor ratio, and the lower F 1s signal in frame B as compared to frame A contributes to no observation of B 1s in frame B over a signal background. For five samples exposed to BF_3 for 60 min at 40 °C similarly to those in frame A, the average F 1s-to-I 3d peak area ratio was 0.12 ± 0.06. For five samples exposed to BF_3 for 5 min at 25 °C similarly to those in frame B, the F 1s-to-I 3d peak area ratio was 0.032 ± 0.004.

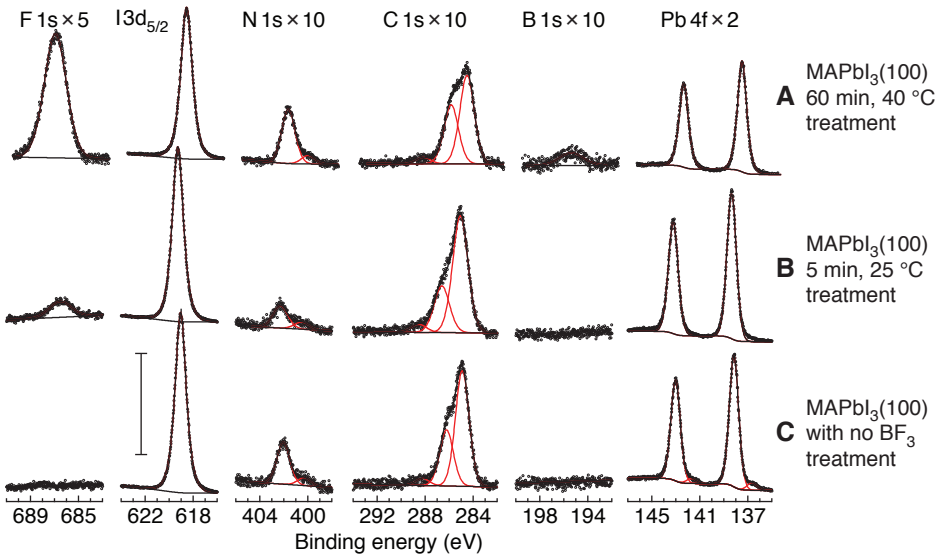

Figure 8. XP spectra of (A) a $MAPbI_3(100)_t$ face following an ethereal BF_3 treatment for 60 min at 40 °C, (B) a $MAPbI_3(100)_t$ face following a 5-min, 25 °C-BF_3 treatment, and (C) an untreated $MAPbI_3(100)_t$ sample. A correlation between F 1s feature areas and treatment conditions indicates a reaction between BF_3 and the perovskite. The scale bar denotes 5000 cps for the I $3d_{5/2}$ region with others magnified as indicated.

A substrate overlayer model further interprets the XP spectra in Fig. 6. For a model in which one BF_3 molecule adsorbs to a $MAPbI_3$ $(100)_t$ surface per cubic unit cell or two per tetragonal unit cell, one complete monolayer would have a F 1s-to-I $3d_{5/2}$ peak area ratio of 0.089. Based on this "ideal" fluorine-to-iodide monolayer ratio, we interpret the

results for the 60 min exposures at 40 °C (similar to Fig. 6A) to be well in excess of monolayer adsorption. This interpretation considers the comparably smooth but not atomically flat MAPbI3(100)$_t$ SEM included. We discount the possibility of multilayer formation due to weak intermolecular forces between adjacent BF_3 molecules that would likely not survive evacuation in an XPS load lock. With such strong F 1s signals due to 60-min-40-°C exposures, we do not utilize the overlayer equation to assign a coverage but assume near-surface infiltration of BF_3 as discussed below. In contrast to the 60-min-40-°C exposures, a 5 min exposure at room temperature (similar to Fig. 6B) yields a limited, sub-monolayer coverage of BF_3. From the overlayer model, the average F 1s-to-I 3d peak area ratio of 0.032 ± 0.004 corresponds to a coverage of 40 ± 5% on a model $MAPbI_3$(100) surface. Considering that "real" $MAPbI_3(100)_t$ surfaces have step edges, pits, and defects that should lead to an increased amount of interfacial halide sites and opportunistic BF_3 bonding opportunities, we assume that this 40% value represents an upper bound for "real" surface adsorption for the given reaction conditions.

Boron trifluoride exposures show that the majority of BF_3 adsorption occurs quickly at high temperature (40 °C) in the DCM/n-hexane mixture. Each experiment utilizing the high temperature reaction results in above 100% coverage, increasing with time. The effect is more profound with the DCM/n-hexane than it is with toluene and this may be attributed to varying solubilities of the BF_3 etherate. The effect of time on the relative fluorine can be seen in Figure 9.

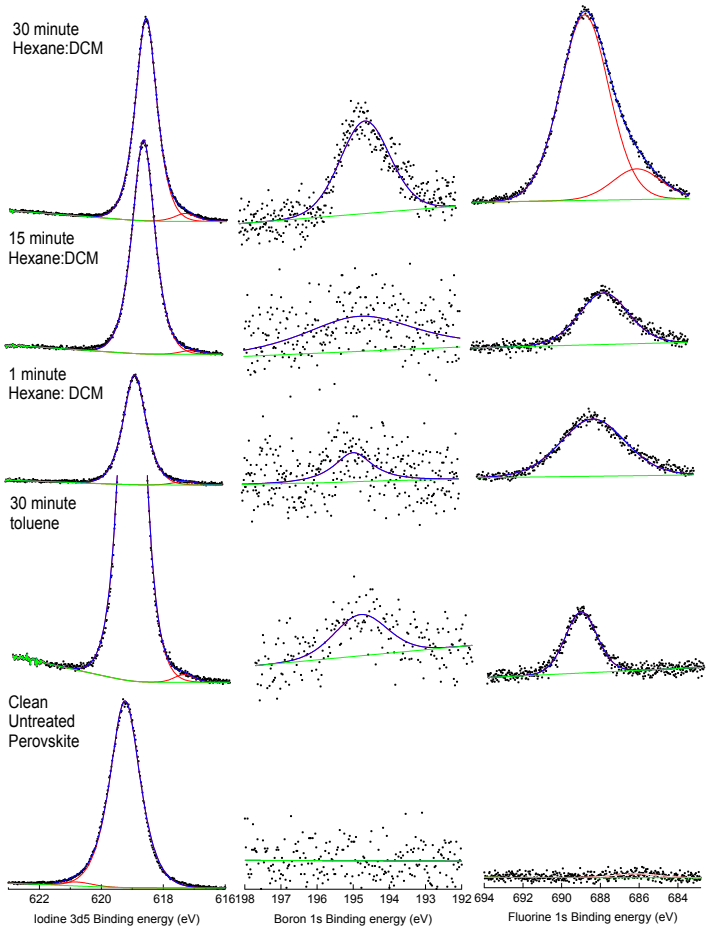

Figure 9. XP spectra of iodine 3d5, boron 1s, and fluorine 1s photoelectrons indicating greater than monolayer coverages as defined by the substrate overlayer model. This is hypothesized to be due to BF_3 infiltration that occurs due to the small size of BF_3 in combination with increased lattice vibrations at elevated temperatures.

4.2. TPD Determination of BF_3 Adsorbate Interaction Energy

Temperature-programmed desorption elucidates the interaction energy of BF_3 with $MAPbI_3(100)_t$ surfaces. Desorption experiments were conducted on at least three samples for each specific exposure/perovskite combination. Figure 10 presents

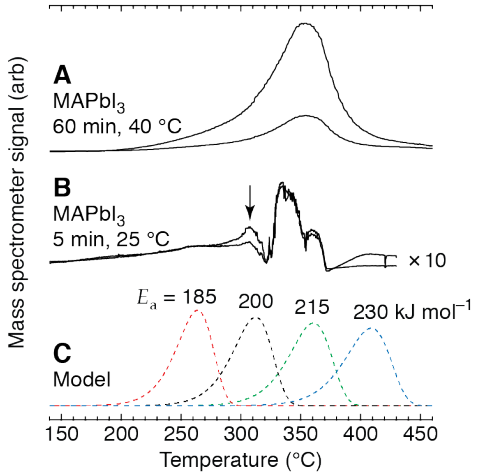

Figure 10. Desorption traces of 48 and 49 m/z following BF3 treatment. The broad desorption traces from MAPbI3 following a 60 min, 40 °C exposure is characteristic of multilayer, infiltrated BF3 that desorbs concomitantly with perovskite breakdown (frame A). For $MAPbI_3$ with a 5 min BF_3 treatment at 25 °C, a small, arrow-highlighted feature at 310 °C in frame B follows the naturally occurring isotopic pattern of BF_2^+ indicative of BF_3 desorption prior to crystal decomposition above 320 °C. Frame C presents dashed traces for modeled first-order desorption with activation energy values of 185 (red), 200 (black), 215 (green), and 230 kJ mol^{-1} (blue).

representative desorption traces for (frame A) $MAPbI_3(100)_t$ following a 60-min, 40-°C exposure to ethereal BF_3 and (frame B) $MAPbI_3(100)_t$ following a 5-min, 25-°C exposure. In frames A and B, the larger trace corresponds to the desorption signal at 49 *m*/*z* and the smaller trace corresponds to the desorption signal at 48 *m*/*z*. Frame B magnifies the desorption traces 10× relative to the traces presented in frames A and C. For comparison to Redhead-style desorption,[54] frame C includes model first-order desorption traces for the experimentally utilized 0.33 K s^{-1} heating rate and a 10^{13} s^{-1} preexponential factor. The red, black, green, and blue dashed traces in Fig. 11C respectively correspond to desorption with E_a values of 185, 200, 215, and 230 kJ mol^{-1}. For clarity, Figure 10 does

not include the acquired traces at 50 and 51 *m*/*z* that serve as controls for the presented data which do not demonstrate the same shape as the traces at 48 and 49 *m*/*z*.

The results in Figure 10 support the desorption of BF_3 from the perovskites. The ~4:1 signal intensity ratios for the 49 *m*/*z* vs 48 *m*/*z* traces correspond to terrestrial ratios of ^{11}B to ^{10}B, and matches the expected intensities for BF_2^+ that is the primary ionization product of BF_3 electron impact.[53] Comparing the desorption from $MAPbI_3$ surfaces in frames A and B, the stronger intensity in frame A vs frame B corroborates the higher relative BF_3 signals in the photoelectron spectra in Figure 8A–B. The traces in frame A demonstrate maximum desorption intensity at ~350 °C and shapes that are significantly broader than the model traces in frame C. The trace in frame B only demonstrates the expected isotopic pattern over a narrow temperature range between 260 and 320 °C with a peak at ~310 °C as highlighted by the arrow. Importantly for frame B, control traces at 50 and 51 m/z demonstrate the similarly erratic behavior observed between 320 and 380 °C indicating that the spectral features in that temperature range do not correspond to BF_3 detection. We interpret the arrow-highlighted spectral feature in frame B to result from BF_3 desorption with other features resulting from the breakdown of the $MAPbI_3$ sample. Thermogravimetric studies reported the decomposition of $MAPbI_3$ and evolution of methylammonium iodide in a process that initiates at <300 °C with peak desorption intensity at ~360 °C.[58] In the context of substrate decomposition, we interpret the desorption trace in frame A to correspond with the liberation of infiltrated BF_3 concomitant with $MAPbI_3$ breakdown. We further interpret the steadily rising baseline below 300 °C and the erratic behavior between 320 and 380 °C in frame B to result from $MAPbI_3$

decomposition. Indeed, following desorption traces from $MAPbI_3$ only a visibly yellow crystal remains that is likely principally PbI_2, which further agrees with previous results of methylammonium iodide desorption from the decomposing perovskite.[58] As a 5-min 25-°C treatment of BF_3 yields sub-monolayer coverage from Figure 8, we interpret the traces in frame B to best represent the desorption of surface-adsorbed BF_3. Comparison between the model traces in frame C with the thermal location of the desorption traces suggest an activation energy for desorption of 200 ± 10 kJ mol^{-1}. We conservatively estimate the uncertainty in desorption activation energy as 10 kJ mol^{-1} based on non-overlap with adjacent modeled peaks that are separated by 15 kJ mol^{-1}.

4.3. p-trifluoromethylanilinium Chloride Exchange

Exposure of the perovskite surfaces to a DCM-based solution of *p*-trifluoromethylanilinium chloride probed the viability of interfacial A-type perovskite cation exchange, methylammonium on $MAPbI_3$. The trifluoromethyl group provided the basis for observing F 1s photoelectron spectral features. Acquisition in the Cl 2p region elucidated whether the anilinium chloride molecule simply deposited on the surface in a reaction that should yield observable Cl 2p features, or whether some other reaction mechanism occurred that results in no observable Cl 2p.

Figure 11 presents representative F 1s, I $3d_{5/2}$, N 1s, C 1s, Cl 2p, and Pb 4f regions of XP photoelectron spectra that explore the interaction of $MAPbI_3(100)_t$ with *p*-trifluoromethylanilinium chloride. Frame A, top, presents spectra for $MAPbI_3$ following a 60-min, 25-°C treatment of *p*-trifluoromethylanilinium chloride in DCM. Frame B, bottom, contains spectra for $MAPbI_3(100)_t$ following a 60-min, 25-°C DCM exposure with no anilinium species added. The F 1s and Cl 2p regions in frame A demonstrate the

presence of fluorine on the anilinium-treated $MAPbI_3$ surface, but no chloride feature within the limits of detection. The ~689 eV location of the F 1s is consistent with fluorine atoms that are covalently bound to carbon. For interpretation of the Cl 2p results, if one chloride anion had adsorbed for every *p*-trifluoromethylanilinium cation, the solid trace above the dotted Cl 2p raw data represents an anticipated Cl 2p signal in frame A. The 269 eV cps peak area in the F 1s feature, the 3:1 F:Cl atomic ratio in *p*-trifluoromethylanilinium chloride, and the 1:0.770 sensitivity-factor ratio for F 1s vs Cl 2p yields the 69.1 eV cps size of the anticipated Cl 2p feature. While small, the anticipated Cl 2p trace has a comparable intensity to the signal-to-noise ratio and thus should be observable if present. We ascribe the lack of observable Cl 2p features to the absence of chloride following the surface treatment of $MAPbI_3(100)_t$ with *p*-trifluoromethylanilinium chloride. Notably, both the spectra of a sample treated by *p*-trifluoromethylanilinium chloride in DCM in frame A and the sample exposed to DCM with no anilinium species in frame B demonstrate no quantifiable signals in the Cl 2p region. The absence of quantifiable Cl 2p signals in either spectrum indicates that dichloromethane also interacts only weakly with the $MAPbI_3(100)_t$ substrate surface.

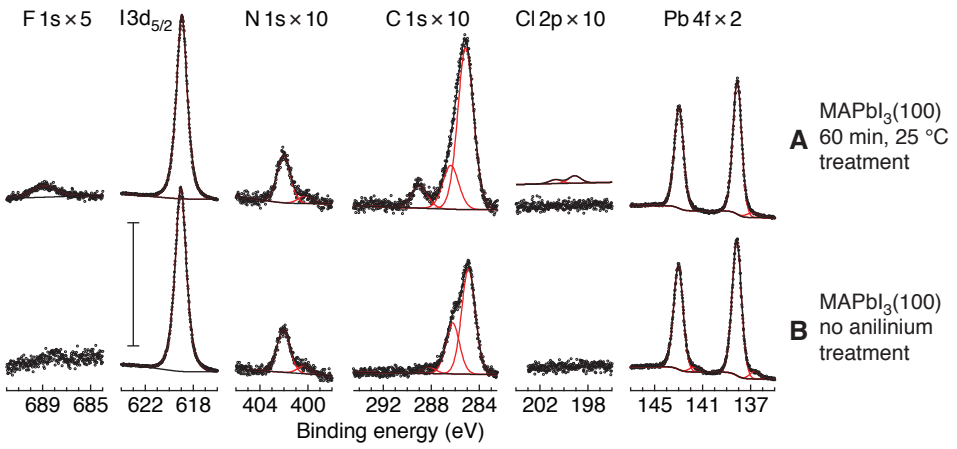

Figure 11. XP spectra of $MAPbI_3(100)_t$ samples that were (A) exposed to a 60-min, 25-°C treatment of *p*-trifluoromethylanilinium chloride in DCM, and (B) similarly exposed to DCM with no added anilinium species. The traced spectral Cl 2p feature atop the raw data in frame A indicates an expected feature based on the observed F 1s spectrum. The I $3d_{5/2}$ scale bar denotes 5000 cps.

From a substrate overlayer model that assumes the adsorption of one *p*-trifluoromethylanilinium per cubic unit cell area or two per tetrahedral unit cell area, complete interfacial exchange for methylammonium on idealized $MAPbI_3(100)_t$ would yield a F 1s-to-I $3d_{5/2}$ area ratio of 0.112 as detailed in the supporting information. For six trials consisting of a 60 min treatment at 25 °C, XP spectra yielded a F 1s-to-I $3d_{5/2}$ area ratio of 0.020 ± 0.007, corresponding to a 20 ± 5% coverage. For three trials consisting of 60 min treatment at 40 °C, XP spectra demonstrated a F 1s-to-I $3d_{5/2}$ area ratio of 0.043 ± 0.036, corresponding to a 40 ± 30% coverage (calculated coverages do not scale linearly with changes in the peak ratios). While 40 °C treatments of BF_3 lead to significantly increased signals vs 25 °C reactions, increased temperatures demonstrate only modestly increased anilinium coverage values that remain below those of one "perfect" monolayer. We straightforwardly attribute higher coverages to a 40 °C vs 25 °C reaction temperature, however increased reaction times do not significantly affect

coverage values. Notably, the significantly larger *p*-trifluoromethylanilinium cation is unlikely to infiltrate the perovskite crystal relative to the smaller, neutral BF_3.

4.3.1. *p*-Trifluoromethyl Anilinium Chloride Doped Synthesis

Perovskites synthesized using the GBL inverse temperature crystallization method doped with 10 mM of *p*-trifluoromethylanilinium chloride definitively contain fluorine but do not show any sign of chlorine. This is a significant observation since it has been noted that mixed halide perovskites exhibit a segregation of the chloride from iodide to the edges as opposed to an even distribution.[59] The fluorine signal is indicative of above 100% coverage based on the substrate overlayer model. This may be due to *p*-trifluoromethylanilinium molecules being trapped within the perovskite while at the same time excluding the chloride. XP spectra of the doped synthesis can be seen in Figure 12.

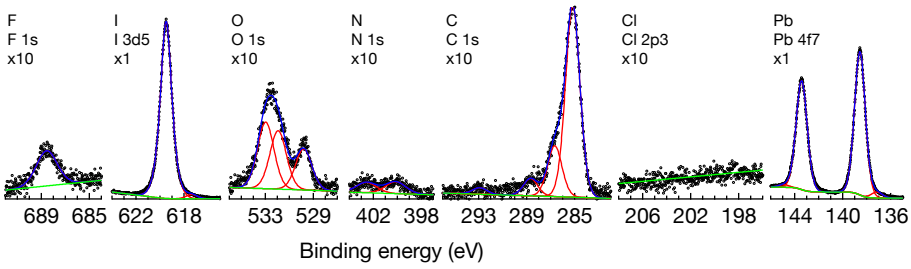

Figure 12. XP spectra of a p-trifluoromethylanilinium chloride doped synthesis perovskite specimen. The experiment used a 10 mM doping concentration. There is a clearly defined fluorine signal and no appreciable chlorine. The absence of chlorine further supports the exchange mechanism presented earlier.

4.4. Metal Ligation with 4,4'-bis(trifluoromethyl)-2,2'-bipyridine

Figure 13 presents representative spectra following an (A) 60-min, 25-°C treatment of the fluorinated bpy compound in DCM with $MAPbI_3(100)_t$, and a (B) commensurate exposure of DCM to a $MAPbI_3(100)_t$ sample DCM in the absence of the tagged bpy compound. Within the limits of detection, no observable difference exists in the F 1s

region for a sample treated with the fluorinated bpy compound as compared to a sample with no fluorinated bpy exposure. As above, the absence of features in the Cl 2p region indicates no strong adsorption of the dichloromethane solvent in either instance. We attribute the absence of F 1s signals to at most trace adsorption of the fluorinated bpy compound.

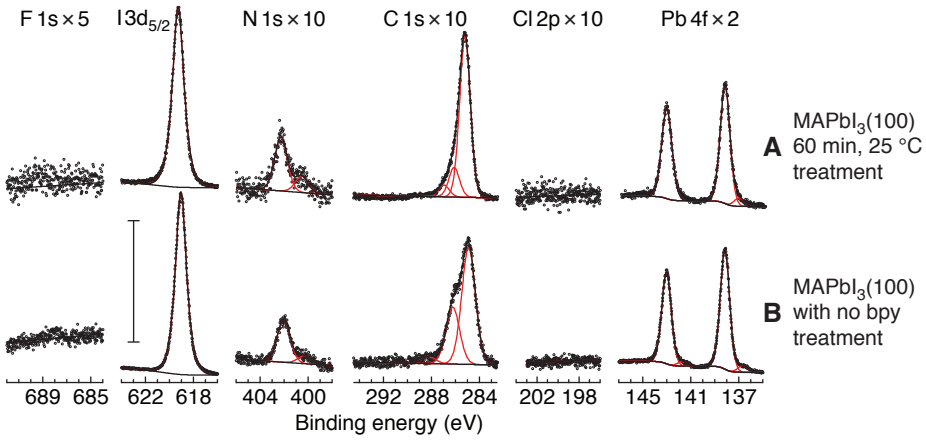

Figure 13. XP spectra $MAPbI_3(100)_t$ samples that were (A) exposed to a 60-min, 25-°C treatment of 4,4'-bis(trifluoromethyl)-2,2'-bipyridine in DCM, and (B) similarly exposed to DCM with no added bpy species. Only nominal signals in the F 1s region above background signals implies at most trace adsorption of the fluorinated bpy. The I $3d_{5/2}$ scale bar denotes 5000 cps.

The 4,4'-bis(trifluoromethyl)-2,2'-bipyridine reaction solutions were examined using total x-ray reflectance fluorescence spectroscopy (TXRF) to observe any quantifiable changes in the lead fingerprint. The relative areas were compared from one spectrum to another to gain a qualitative understanding of how the solutions behaved and their lead content trends. Figure 14 shows the TXRF spectra. Frame A shows the blank and at 10.5 KeV the lead signal is indistinguishable from the noise. Frame B is of the solution after a normal experiment and the lead at 10.5 KeV is significantly higher than the blank in Frame A. This indicates that there is lead that can be ligated from the surface,

whether that is from a facet with exposed lead or from a surface defect which leaves lead open to ligation. Frame C shows the same experiment utilizing a crushed perovskite. This would open up many more sites, exposing lead that can be ligated by the bpy compound.

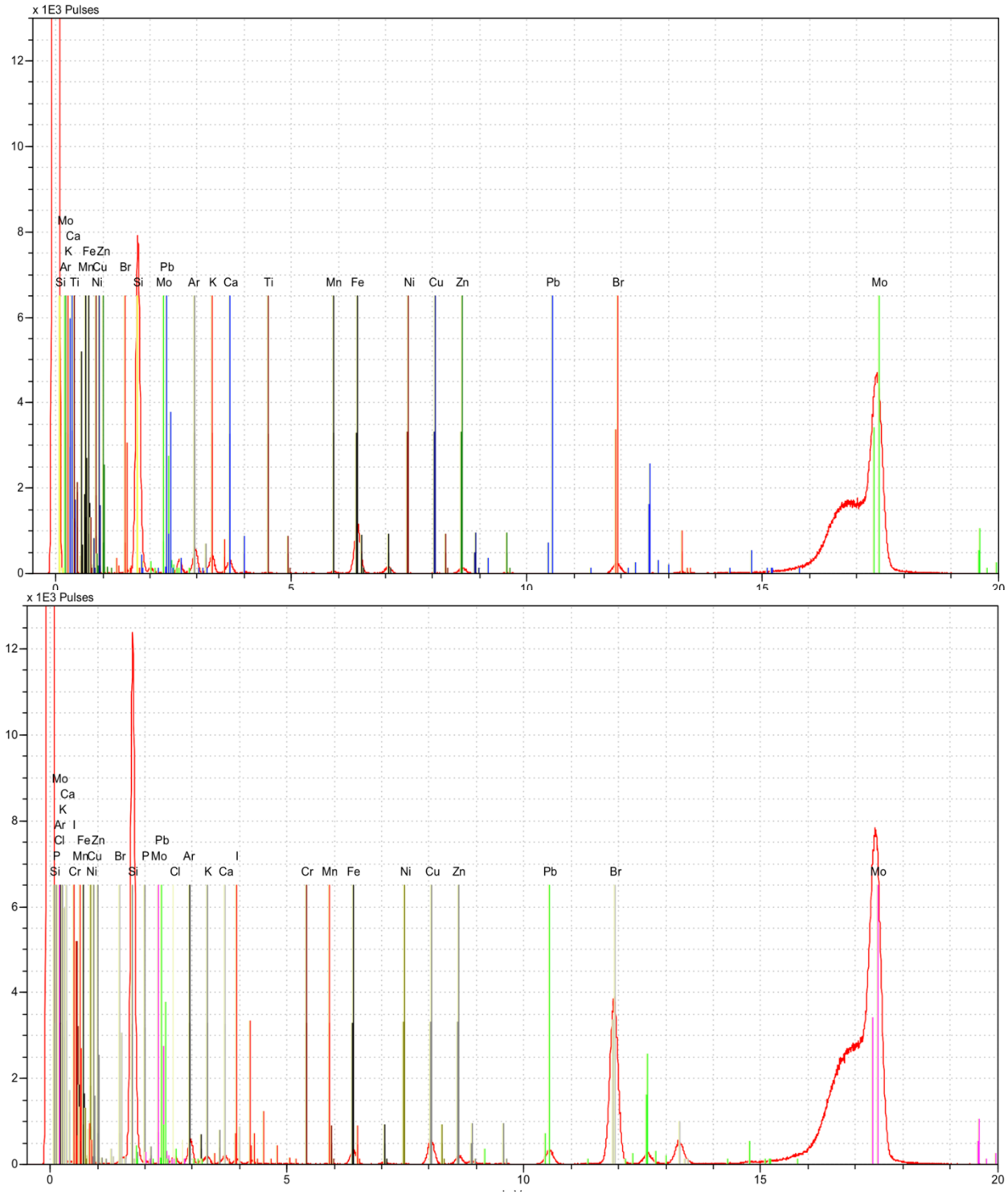

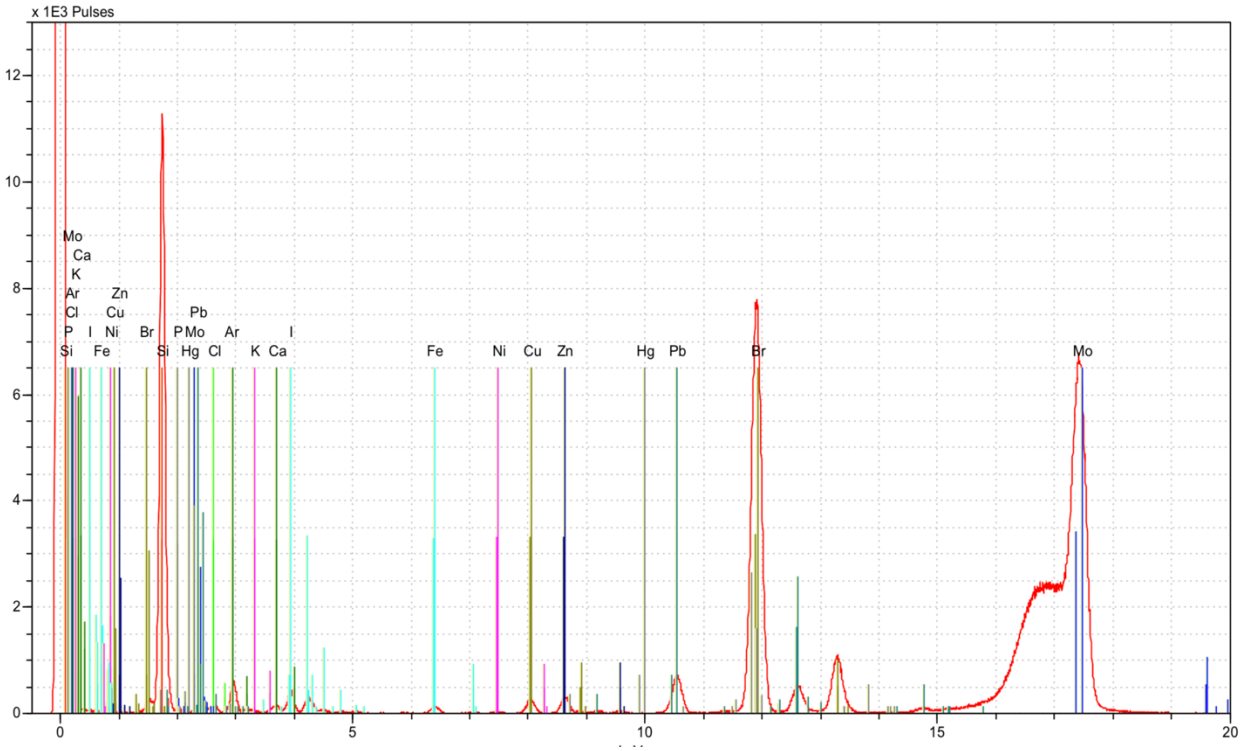

Figure 14. TXRF spectra showing an increased signal from lead at about 10.5 KeV in solution from frame A (blank), to frame B (normal experiment), and finally to frame C (crushed perovskite). The data presented in these specra is qualitatively useful to see the change from one experiment to the next. This would indicate that lead is indeed able to be ligated from the surface with the bpy ligand, but this interaction is strong enough to be solvated back into solution, taking the lead with it. This signal increase is more profound in the crushed perovskite experiment, which is likely due to increased surface area and other exposed facets.

The lead signal at 10.5 KeV is much higher than in either Frame A or B and its relative ratio from Frame B is approximately two times as great.

4.5. 2,2,2-trifluoroethylammonium Chloride Exchange

Exposure to 2,2,2-trifluoroethylamine hydrochloride probed for expansion of ammonium exchange reagent scope. The experiment was attempted once using DCM and once in chlorobenzene-based solutions. The ideal ratios are similar to the *p*-trifluoromethyl anilinium experiments with fluorine to iodine ratio of about 0.11 as 100%. There is a trace fluorine signal in the dichloromethane procedure. The ratio of fluorine to iodine in the DCM procedure is 0.008 or approximately 7% coverage. The chlorine is

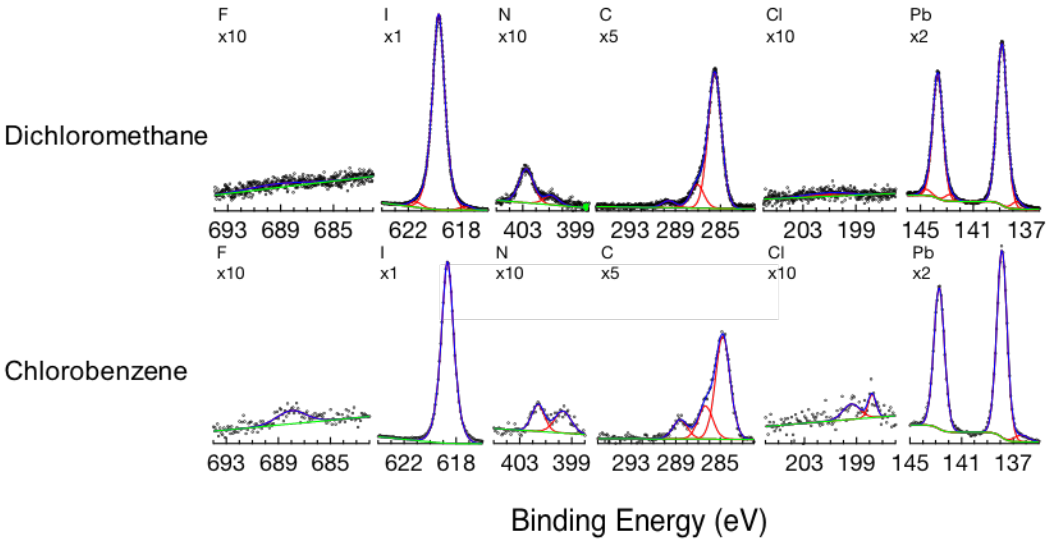

Figure 15. 2,2,2-trifluoroethylamine hydrochloride XP spectral data in dichloromethane (top) and chlorobenzene (bottom). In both cases there is fluorine and chlorine present but to a much greater extent in the chlorobenzene experiment. The ratio of fluorine to chlorine is significant since it indicates a greater chlorine than substitution ratio. This may indicate no exchange while solvent is infiltrating the sample.

disproportionately high with a ratio using the sensitivity factor, area under the curve, and stoichiometric abundance with a ratio of about 2 chlorine atoms per fluorine. The anomalous signal does not line up with chlorine at 201 and 199 eV respectively and instead shows up at around 198 and 200 The chlorobenzene experiment has a fluorine to iodine ratio of 0.015, which works out to about 14%. The fluorine to chlorine ratio is higher than expected and is roughly 1.2 chlorine atoms per fluorine. The XP spectra can be seen in Figure 15.

4.6. Triphenylborane Functionalization

Triphenylborane did not show any evidence of adsorption using XPS on the methylammonium lead iodide perovskites. Detection and quantification of triphenylborane on the surface would have been observed using the boron spectrum at 193 eV. The other spectra appear as usual for a clean perovskite, the carbon is significantly higher than usual. The lead 4f spectrum shows no sign of any metallic lead or lead oxides. A representative of the XP spectra for triphenylborane on $MAPbI_3$ can be seen in Figure 16.

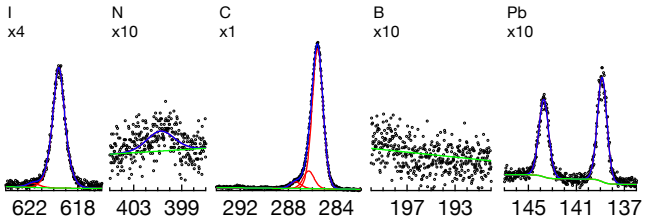

Figure 16. XP spectra of triphenylborane adsorption on methylammonium lead iodide. The spectra appear as if it were an unmodified sample. The triphenylborane would be detected primarily through boron at about 193 eV.

4.7. Tris(pentafluorophenyl)borane Functionalization

Tris(pentafluorophenyl)borane exhibited adsorption on the perovskite surface. The fluorine signal is much more intense than boron trifluoride as expected due to the stoichiometric abundance being 5 times greater per mole. The boron is comparable to previously examined BF_3 samples. Lead displays minimal metallic character, indicative of minimal x-ray damage. There is a significant fluorine signal and the CF carbon is

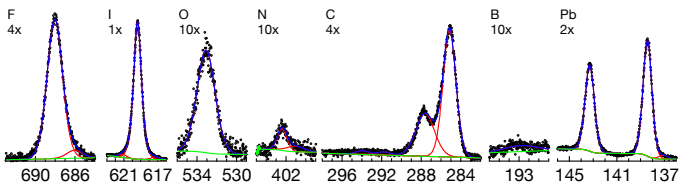

Figure 17. XP spectra of methylammonium lead iodide following tris(pentafluorophenyl)borane exposure. The fluorine signal is very strong as is expected. Carbon involved in the C-F bond can be seen at about 292 and 294 eV, the signals are very small relative to the bulk and adventitious carbon. Based on the relative ratio of fluorine to iodine being 0.409, using the overlayer model, yields a coverage of about 90%.

detectable between 292 and 294 eV. Boron is also just above the baseline, which becomes observable as coverages increase. The XP spectra for the representative tris(pentafluorophenyl)borane experiment can be seen in Figure 17. The fluorine to iodine ratio of about 0.409 correlates with roughly 90% surface coverage.

4.8. SEM Imaging

Methylammonium lead iodide single crystals include small defects and pinholes. Defects include crystal deformations, which may be up to a few microns in size. A cross-sectional SEM micrograph in Figure 18 shows a triangular inclusion that is approximately a 2 μm wide by 2 μm across by 3 μm tall in size, although this makes up a clear minority of the surface. Top down SEM micrographs in Figure 19 shows the pinhole style defects, which exist on the nanometer scale. Most pinoles are below 100 nm with few being larger than 100 nm in diameter.

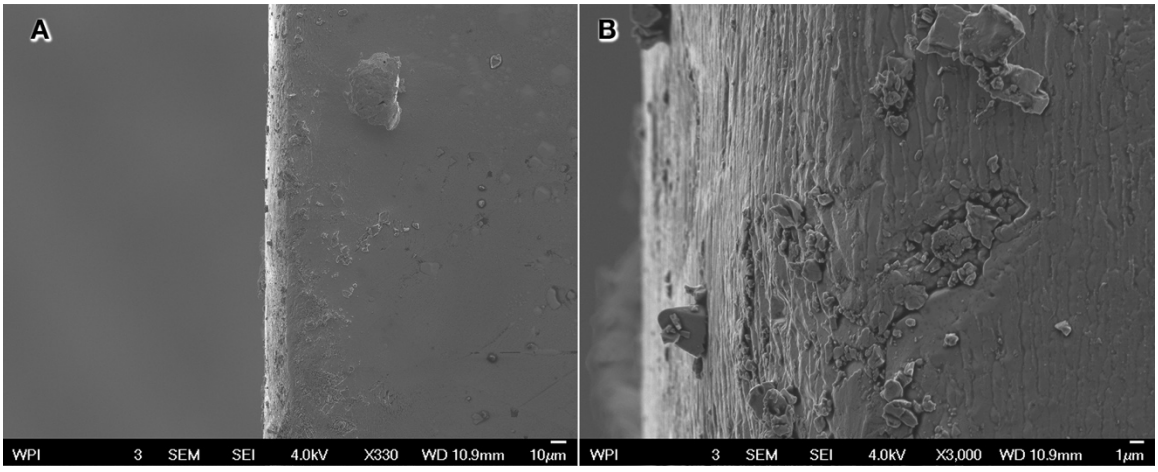

Figure 18. Cross sectional SEM micrographs at 330X and 3000X magnification (left and right respectively) of a typical $MAPbI_3(100)_t$ sample showing cross-sectional surface over a large range and on a smalls scale. The surface defects are small and the surface is primarily flat.

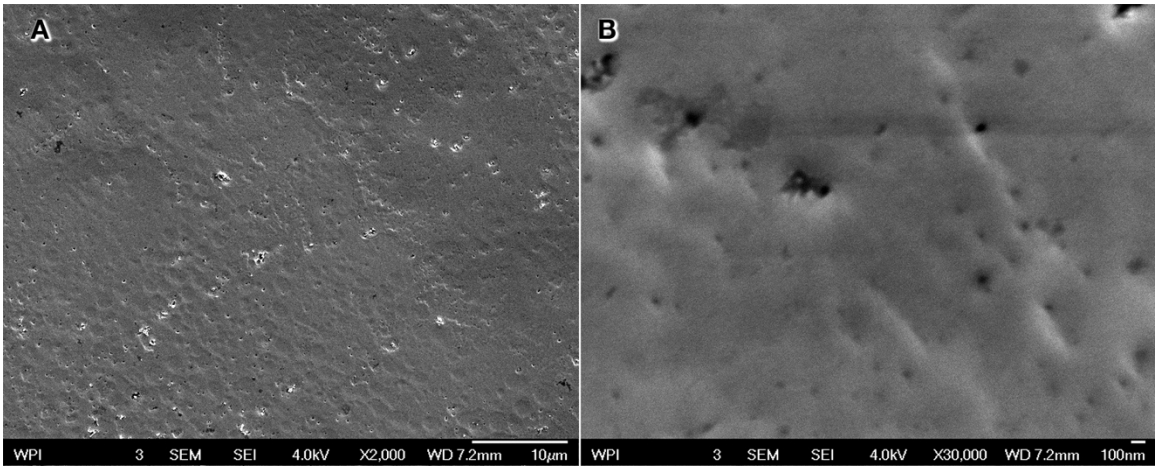

Figure 19. Top-down SEM micrographs at 2000X and 30000X magnification (left and right respectively) show pinhole defects and the overall surface texture in a typical $MAPbI_3(100)_t$ sample. Features visible on the surface are generally sub-100-nm in size. The micrograph on the right shows a typical pinhole site where most are well below 100 nm in diameter and few are larger than 100 nm in diameter.

Chapter 5. Leveraging $MAPbI_3$ $(100)_t$ Surface Chemistry for Selective Adsorption of Chemical Handles

This chapter details the attempts at utilizing the fundamental knowledge gained form the prior studies towards applying functional chemical groups. The halide site is targeted with both boric acid and 4-trifluoromethylphenyl boronic acid, pinacol ester and the ammonium site is targeted with 2-thiophene methylammonium and 4-ammonium benzoic acid.

5.1. Boric Acid

Boric acid posed a simple, yet quite possibly effective chemical hook on the surface for subsequent functionalization with three hydroxy groups. There was no appreciable boron in in the hexane, toluene, or anisole mixtures when conducted using meticulously prepped material including three freeze-pump-thaw cycles and drying over molecular sieves for at least three days. These experiments can be seen in Figure 20. In

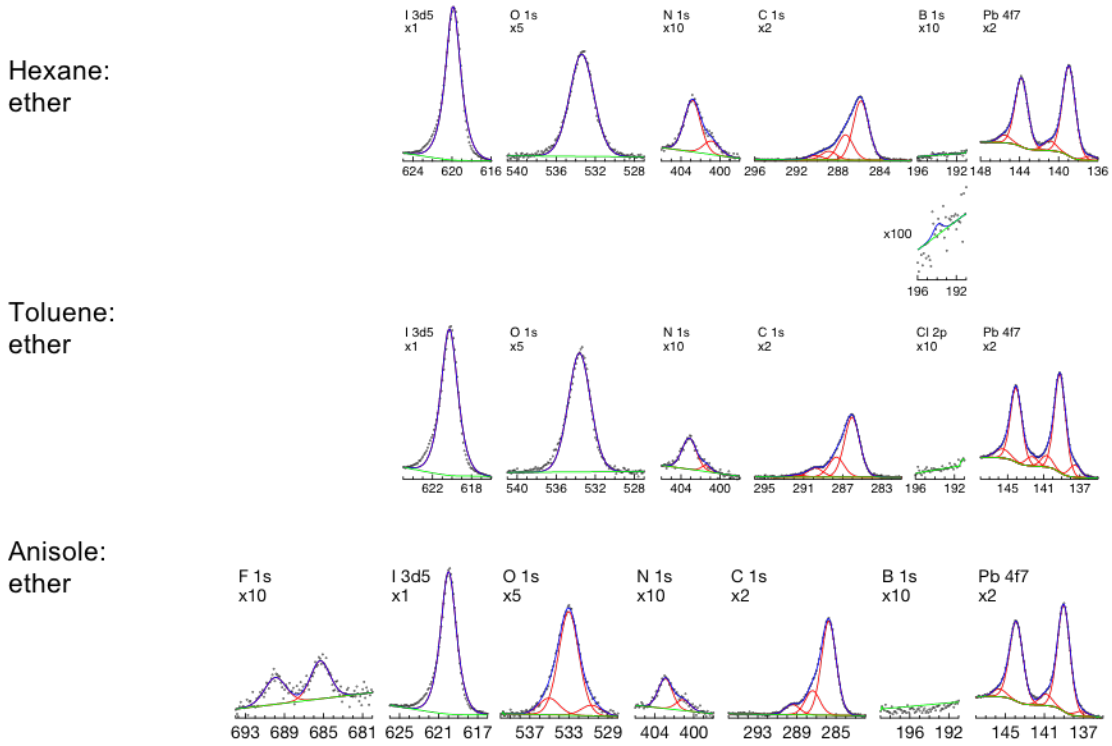

Figure 20. Hexane, toluene, and anisole solvent mixtures (top to bottom) XP spectra for the boric acid functionalization. In these experiments, the oxygen and boron spectra are the important markers. There would be a signal at 193 eV if boron was present. In the experiment utilizing anisole, there was a significant fluorine signal that appears to be consistent with both organic and inorganic fluorine.

the anisole mixture, there was a significant fluorine contaminant consistent with both organic and inorganic fluorine. The hypothesis is that this came from contaminated glassware.

The first experiment was conducted using hexane: diethyl ether as the solvent but was completed using an expedited procedure without the extended rest over activated sieves or multiple freeze-pump-thaw cycles to remove dissolved gasses. Deposition of boron oxide films were observed in 24 hour reactions with increasing thickness over time. A one hour reaction (not shown) did not produce any measurable boron oxide. The boron signal at 193 eV is consistent with past boron signals and with a literature study on boron oxide surface coverage.[60] The XP spectra for these cases can be seen in Figure 21.

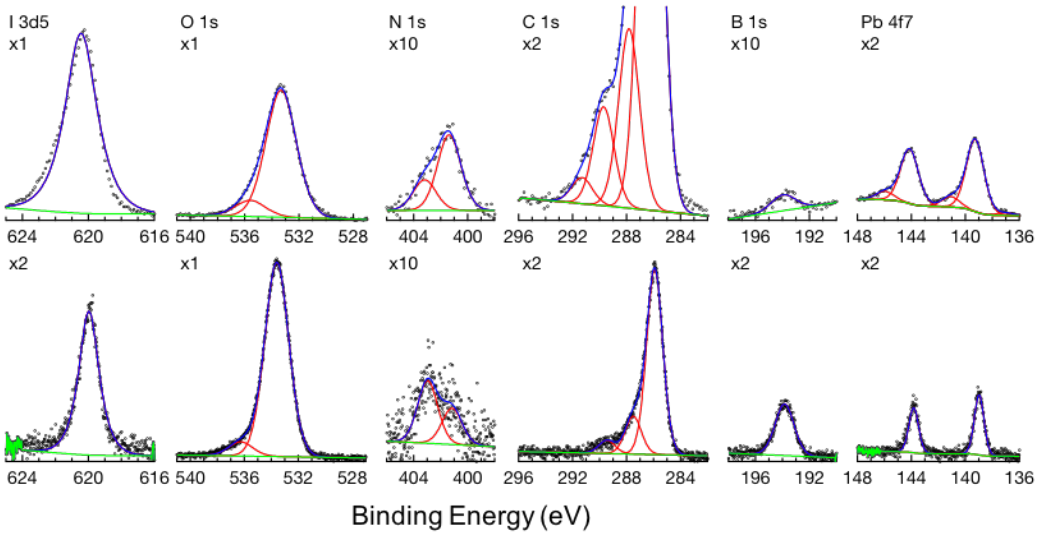

Figure 21. XP spectra of a perovskite after hexane: diethyl ether boric acid mixture exposure 24 hour (bottom) reaction and the same sample two weeks later after exposure to ambient atmosphere under dark conditions. There is a significant boron signal at 193 eV and the oxygen is significantly higher. This is believed to be from boron oxide on the surface. After two weeks, the perovskite appeared to be normal and not degraded. The XP spectra does hoever show a massive increase in carbon, likely the result of adventitious carbon deposition from the air.

5.2. 4-Trifluoromethylphenyl Boronic Acid, Pinacol Ester

The 4-Trifluoromethylphenylboronic acid, pinacol ester did not successfully functionalize the surface in any case. The room temperature diethyl ether reaction had a significantly higher carbon and oxygen signal than usual in XPS. Other than the anomalous carbon and oxygen it appeared to have no interaction. The XP spectra can be seen in Figure 22.

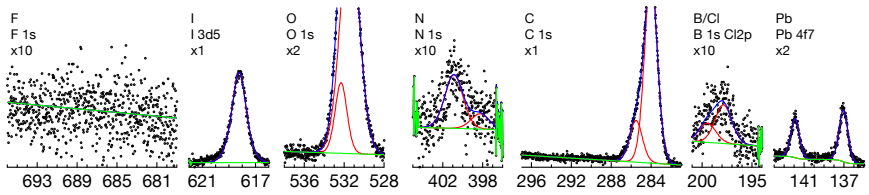

Figure 22. 4-trifluoromethylphenylboronic acid, pinacol ester 10 mM in diethyl ether for 5 hours resulted in no fluorine signal. There was a significantly higher carbon and oxygen signal. This is believed to be due to adventitious carbon deposits. There is also a chlorine signal and is believed to be residual from the starting material.

The 40 mM, refluxing dichloromethane and diethyl ether reactions produced similar results. There was no discernable fluorine. The same sample was examined using a high pass energy scan on fluorine and iodine in an effort to pick up on trace quantities of fluorine. The XP spectra can be seen in Figure 23

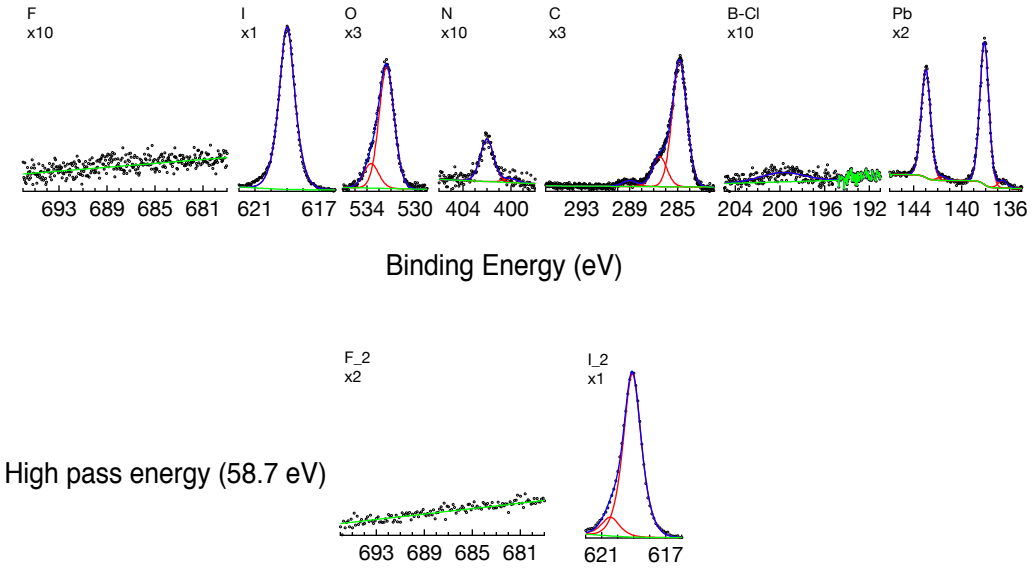

Figure 23. Refluxing dichloromethane resulted in no discernable fluorine signal. There is however, a discernable chlorine signal. This may be from the dichloromethane or as a residual byproduct in the boron compound. The high pass energy scan at 58.7 eV further supports a lack of surface functionalization by the acid.

The final experiment utilized an 80 mM solution in refluxing chlorobenzene to provide additional energy to the reaction in an effort to make the reaction more favorable. There is no discernable fluorine signal, which would be the indicator of unsuccessful

surface functionalization. The XP spectra from the refluxing chlorobenzene experiment can be seen in Figure 24.

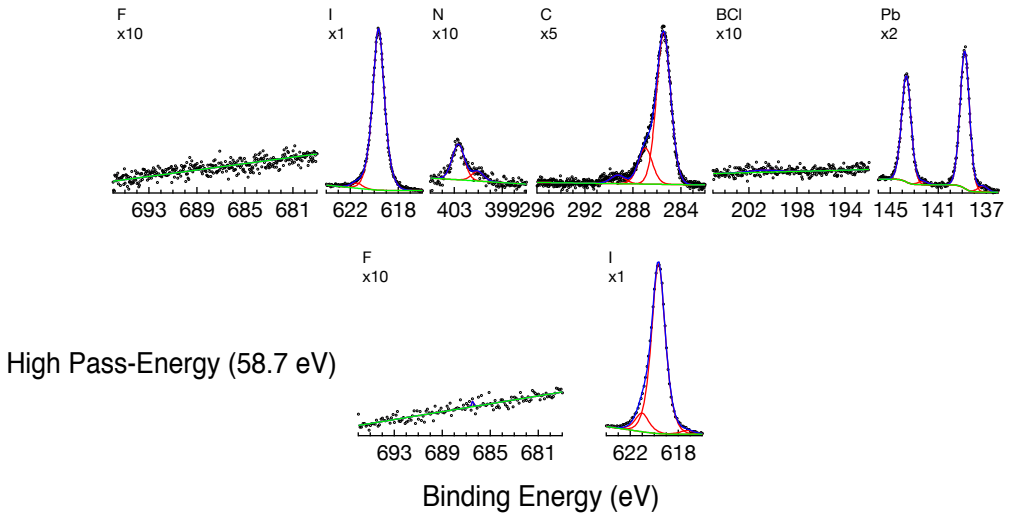

Figure 24. 4-trifluoromethylphenylboronic acid, pinacol ester experiment in refluxing chlorobenzene for 5 hours resulted in no discernable fluorine signal in XPS analysis. A high pass energy scan was additionally conducted on fluorine and iodine in an effort to see any fluorine present on the surface.

5.3. 2-Thiophene Methylammonium Surface Exchange

Solubility studies attempted to elucidate suitable solvents for the chloride salt in a variety of solvents including thiophene, tetrahydrothiophene, anisole, ethyl acetate, chlorobenzene, acetonitrile, DCM, and toluene. 2-thiophenemethylammonium chloride is marginally soluble in thiophene, tetrahydrothiophene, and DCM; and very soluble in acetonitrile.

Exposure to saturated 2-thiophene methylammonium chloride in DCM resulted in no discernable sulfur in XPS analysis seen in Figure 25. There is an abnormally high proportion of reduced lead in the spectra. It is not known if this is in-part responsible for the unsuccessful exchange.

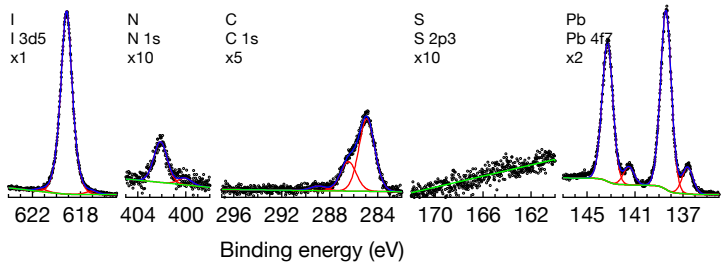

Figure 25. XP spectra of a 2-thiophene methylammonium chloride treated $MAPbI_3$ perovskite in DCM for one hour at room temperature. There is no discernable sulfur from the sulfur 2p3 photoelectron spectrum.

Exposure of a $MAPbI_3$ perovskite to a saturated solution of 2-thiophene methylammonium chloride in acetonitrile resulted in a hazy surface with no sulfur in XP analysis. The flask was notably left with a white residue. The acetonitrile bath deposition of 2-thiophene methylammonium chloride can be seen in Figure 26.

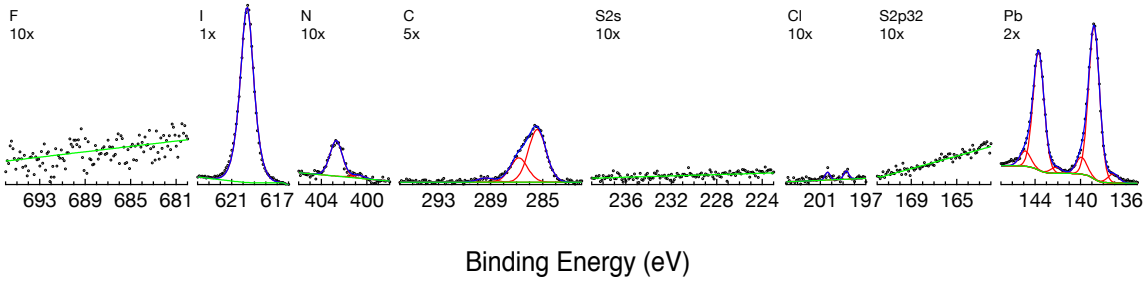

Figure 26. XP spectra of a $MAPbI_3$ perovskite exposed to a saturated solution of 2-thiophene methylammonium chloride in acetonitrile. No discernable sulfur can be seen in either the 2s or 2p3 spectra.

Exposure to 2-thiophenemethylammonium hexafluorophosphate in DCM for one hour did not appear to have any appreciable sulfur on the surface. There was some residual fluorine that may come from the hexafluorophosphate counteranion. XP spectra can be seen in Figure 27. The broad signal for fluorine at about 686 eV is consistent with fluorophosphate salts.[61] A phosphorous spectrum was not collected during this analysis.

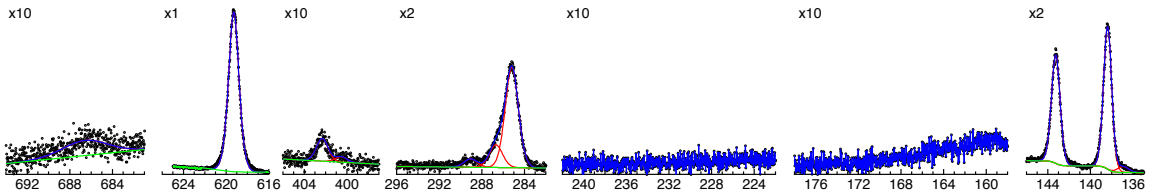

Figure 27. 2-methylammonium thiophene hexafluorophosphate reaction with a methylammonium lead iodide perovskite results in no discernable sulfur signal. There was however a broad fluorine signal. This is believed to be a result of the hexafluorophosphate counteranion. From left to right the spectra are fluorine 1s, iodine $3d_{5/2}$, nitrogen 1s, carbon 1s, sulfur 2s, sulfur 2p, and lead 4f.

Exposure of a perovskite $(100)_t$ face to 10 mM 2-thiophenemethylamine hydrochloride dissolved in warm hydroiodic acid resulted in no appreciable sulfur deposition. The dip in warm hydroiodic acid did result in a "fresh" polish appearance on the surface similarly to its use as a chemical polish. The XP spectra from the hydriodic acid dip application can be seen in Figure 28

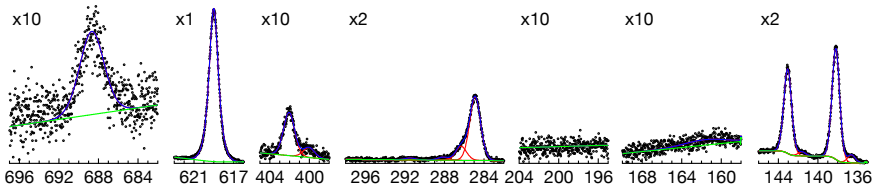

Figure 28. XP spectra of a perovskite $(100)_t$ face after a dip exposure to a 10 mM solution of 2-thiophenemethylamine hydrochloride in warm hydroiodic acid. There is no discernable sulfur signal, but there is however significant fluorine from an unknown source. From left to right the spectra are fluorine 1s, iodine $3d_{5/2}$, nitrogen 1s, carbon 1s, chlorine 2p, sulfur 2p, and lead 4f.

5.4. 4-Ammonium Benzoic Acid Exchange

The 4-ammonium benzoic acid chloride has been examined on the surface with some indication of success but without certainty. IRRAS experiments show indeterminant results but indicate that there has been deposition on the surface. There is a lot of water contamination, which is concatenate with water adsorption on the surface. This may be expected due to the hydrophilicity of the carboxylic acid groups. The IRRAS data from the first experiment can be seen in Figure 29. XPS analysis on a perovskite treated with 4-

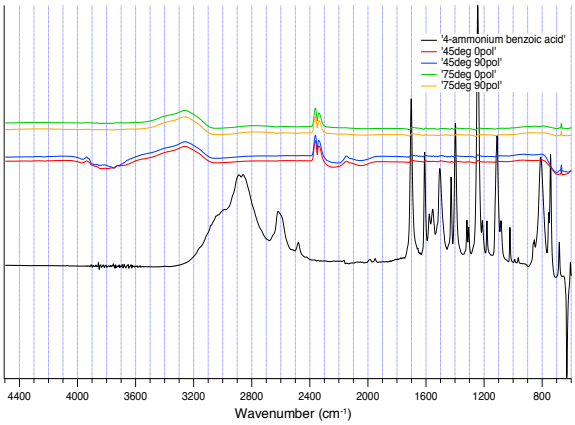

Figure 29. 4-ammonium benzoic acid at 45- and 75-degree reflection with s and p polarized light (red, blue, yellow, and green lines respectively) with the pure salt examined with the golden gate IR accessory (black line). The pure salt contains an aromatic C-H stretch, which shows up as a shoulder at about 3000-3100. The trace also has either the broad ammonium trace or carboxylic OH trace between 2500 and 3000. If the data is examined closely, the regions between 1100-1700 are similar and additionally line up with the NIST Webbook for 4-aminobenzoic acid.[61] On the perovskite surface, surface adsorbed water may inhibit some signal.

ammonium benzoic acid exhibited an expected spectrum with little to no chlorine and a strong carbon signal. The carbon spectrum contains a higher energy carbon at about 289.5 eV which makes sense for a carboxylic acid carbon.[62] The chlorine may be interpreted as an artifact of the solvent used and has been seen in prior data using a dichloromethane bath. Further studies can support or refute the trace level signal. Fluorine was examined as a check for contamination. A small amount of metallic lead

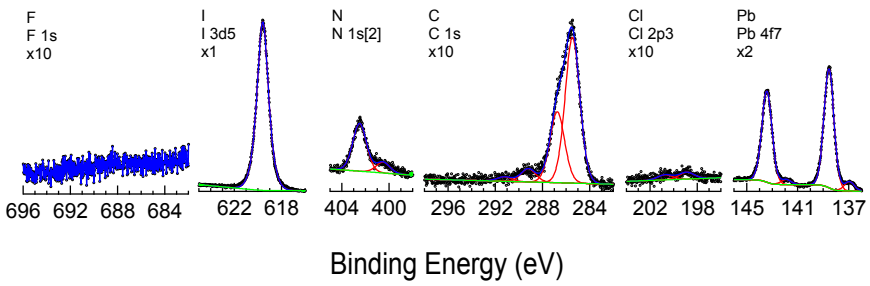

Figure 30. XPS of a 4-ammonium benzoic acid treated perovskite showing a spectrum that looks as would be expected. The carbon signal is clean and has a higher energy carbon at about 289.5 eV which is characteristic of a carboxylic acid.

was present and occurs as a result of extended x-ray exposure. Representative XPS data of a 4-ammonium benzoic acid functionalize perovskite can be seen Figure 30.

5.4. Functionalization of the tetragonal $MAPbI_3$ (100) summary

Functionalizing the $MAPbI_3$ $(100)_t$ facet has proven to be not as straightforward as initially anticipated. Boric acid was a tantalizing opportunity due to its simplicity and low cost. The boronic acid did not appear to have sufficient acidity to react with the perovskite even at high temperature. Boron centers with greater acidity or less steric encumbrance are likely to improve surface functionalization. Ammonium thiophene substitution is also proving to be a challenge. This may be due to the extremely low solubility in perovskite stable solvents. Perhaps longer thiophene chains will enable this reactivity due to the greater solubility in non-polar solvents, which are better for the perovskites. It is also worth noting that a gaseous amine may be capable of exchange at the surface similar to the methylamine grain reformation. Controlled exposures of functional amine gas may be a plausible surface ammonium exchange procedure. The outlook for functionalization and surface examinations is further examined in the final concluding chapter.

Chapter 6. Reactivity of $MAPbI_3$ On non$(100)_t$ Facets

This chapter details all of the aforementioned experiments to varying degrees on the $(112)_t$ facet, $(110)_t$ cuboid, and thin-film perovskite.

6.1. BF_3 Adsorption

The boron trifluoride surface experiments were examined using thin-film substrates on fluorine doped tin oxide (FTO). The experiment did yield a strong fluorine signal which may indicate significant adsorption on thin-film surfaces.

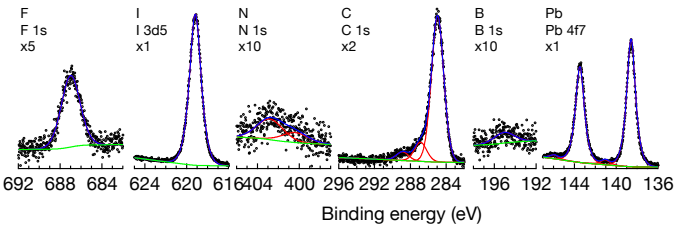

Figure 31. XP spectra of a thin-film methylammonium lead iodide treated with a boron trifluoride solution. There is a significant fluorine signal but further experimentation must be conducted in order to determine if this comes from the BF_3 or from the FTO substrate.

This experiment however does need a background to account for the fluorine present in the FTO substrate. The XP spectra of a representative thin-film perovskite sample treated with the BF_3 procedure on FTO can be seen in Figure 31.

Exposure of the $(112)_t$ face of $MAPbI_3$ demonstrates quantifiable BF_3 after exposure to an ethereal solution at room temperature. This was done as an exploratory reaction and has been estimated. The fluorine to iodine ratio is 0.087, which would correspond with roughly 100% coverage. Exposure of a $MAPbI_3$ 112 surface can be seen in Figure 32.

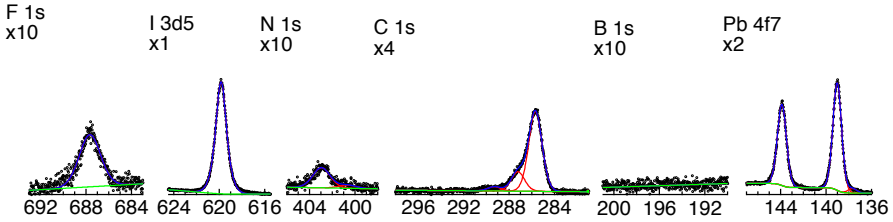

Figure 32. XP spectra of a $(112)_t$ methylammonium lead iodide perovskite facet that was exposed to the boron trifluoride solution for one hour at room temperature. There is minimal to no reduced lead species, which further supports the fluorine adsorption on iodide at the surface.

Exposure of $MAPbI_3$ $(110)_t$ facets grown on cuboid perovskites yields fluorine in XP spectra similar to both the $(100)_t$ and $(112)_t$ facets. A 60-minute 25 °C exposure in an ethereal solution of BF_3 results in BF_3 adsorption on the perovskite surface. A BF_3 exposed and untreated blank sample were run side-by-side to observe the difference. The fluorine to iodine ratio in the treated perovskite is 0.062 based on a single experiment, which translates to roughly 70% surface coverage. The surfaces are not as smooth as the $(100)_t$ facets as examined later in the SEM images. This may cause the fluorine signal to be more pronounced than what would be expected for an ideal, smooth surface. The cuboid perovskites BF_3 treated and blank XP spectra can be seen in Figure 33.

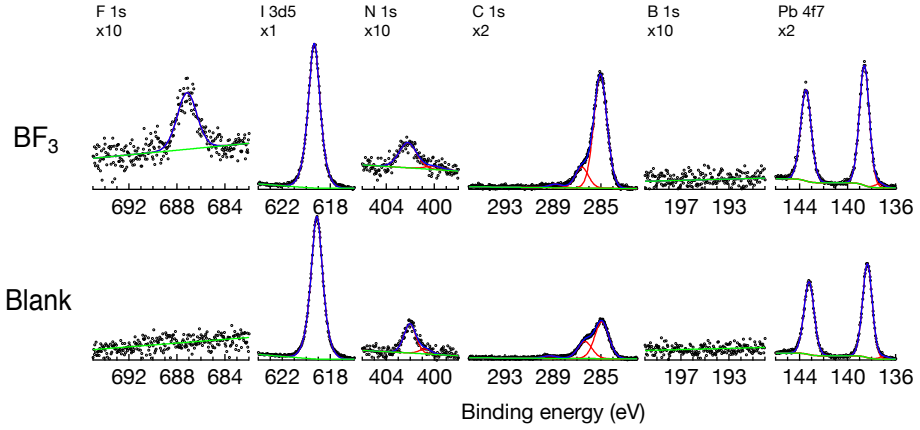

Figure 33. XP spectra of $MAPbI_3$ cuboid $(110)_t$ facets that were exposed to 0.1 M ethereal BF_3 solutions for one hour at 25 °C. The BF_3 treated perovskite (top) exhibits significant differences in the fluorine region when compared to the blank (bottom), indicative of BF_3 adsorption similar to prior experiments on other facets. The blank perovskite was treated similarly to the BF_3 sample but excluding the BF_3. The fluorine to iodine signal ratio is about 0.062, which works out to roughly 70% surface coverage.

6.2. p-Trifluoromethyl Anilinium Exchange

Exposure of the $MAPbI_3$ $(112)_t$ facet to *p*-trifluoromethylanilinium chloride results in a distinguished fluorine spectrum. The $MAPbI_3$ $(112)_t$ facet was examined from an exploratory standpoint to determine if this is another accessible reactive facet for surface functionalization chemistry. The $(112)_t$ facet does successfully undergo surface exchange as seen in the fluorine signal in XPS analysis. The surface exhibits a F/I ratio of 0.07, which can be estimated to approximately a coverage of 60%. The XP spectra can be seen in Figure 34.

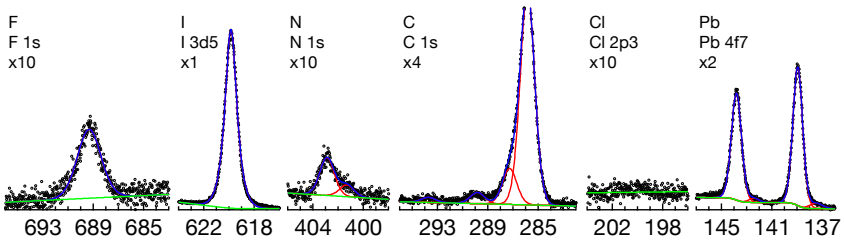

Figure 34. XP spectra of a $MAPbI_3$ perovskite $(112)_t$ facet exposed to p-trifluoromethylanilinium chloride. There is a clearly defined fluorine signal. The chlorine is difficult to distinguish from the baseline, but it may show a trace quantity when examined closely. This may be due to insufficient rinsing.

Exposure of the $MAPbI_3$ $(110)_t$ facet on the cuboid perovskites to a saturated solution of *p*-trifluoromethylanilinium chloride results in a fluorine spectrum that is barely distinguishable from the noise in XPS analysis. The sample was also examined using a

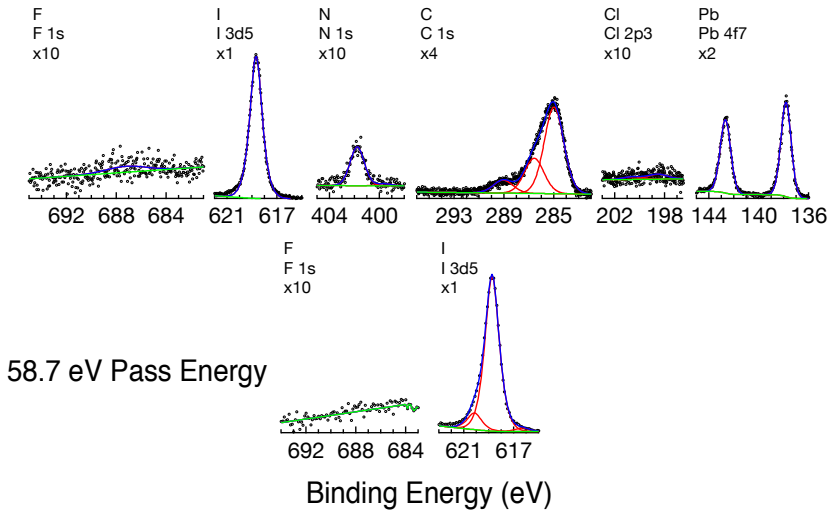

Figure 35. XP spectra of a perovskite cuboic $(110)_t$ surface after exposure to a concentrated solution of p-trifluoromethylanilinium chloride for one hour at room temperature. A very small fluorine signal is possibly distinguishable from the noise in the 23.5 eV scan but indistinguishable in the 58.7 eV pass energy scan. If the signal is considered, It would correspond to a coverage of roughly 10%.

high pass energy scan at 58.7 eV in an effort to see trace fluorine more clearly. This resulted in similar results to the scan at 23.5 eV and did not yield distinguishable fluorine.

If the barely discernable fluorine signal is considered, the ratio of fluorine to iodine of 0.012 is indicative of roughly 10% surface coverage. The XP spectra can be seen in Figure 35.

As a result of the unsatisfactory deposition on the perovskite $(110)_t$ surface the experiment was tried again with solvents prepped to remove more residual water, which may have been the cause of the prior unsatisfactory results. The experiment was conducted on two separate samples with one showing some deposition and the other showing no fluorine, which would indicate exchange at the surface. Based on the fluorine to iodine ratio of about 0.010 F/I, the coverage is estimated to be roughly 9%. The XP spectra for the repeated *p*-trifluoromethylanilinium experiment can be seen in Figure 36.

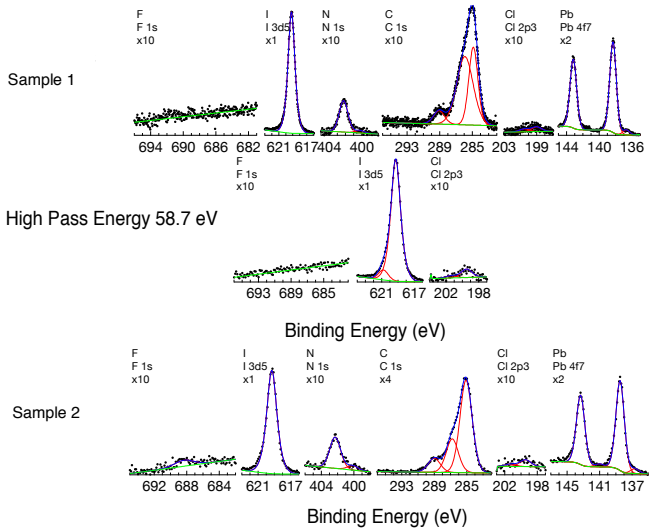

Figure 36. XP spectra of two perovskite $(110)_t$ facet samples after exposure to a saturated TFMA solution. Both samples have a defined chlorine spectrum. This may support the hypothesis that the chlorine is from the solvent and not the ammonium counteranion. The first sample shows no evidence of surface exchange while the second sample corresponds to roughly 9% coverage.

6.3. 4,4'-Bis(trifluoromethyl)-2,2'-Bipyridine Ligation

Exposure of a $MAPbI_3$ 112 facet to the same 60-minute, 25 °C treatment of 4,4'-bis(trifluoromethyl)-2,2'-bipyridine results in trace to no fluorine signal as observed in XPS. The absence of chlorine 2p photoelectrons indicates that there was no residual dichloromethane that became trapped within the structure, this is expected of an ambient temperature reaction. Figure 37 is an example showing the lack of a fluorine signal, which would be indicative of bpy ligation on the surface.

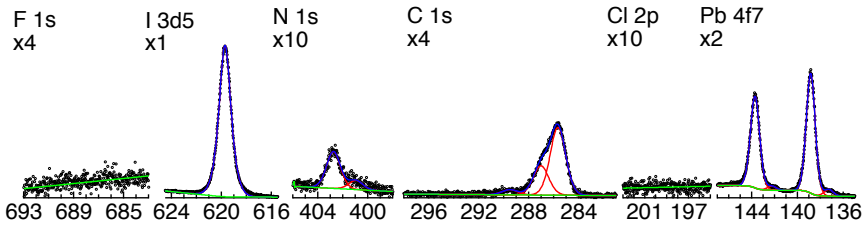

Figure 37. XP spectra of a MAPbI perovskite $(112)_t$ facet after exposure to 4,4'-bis(trifluoromethyl)-2,2'-bipyridine results in no discernable fluorine. There is additionally, no measurable chlorine 2p signal indicative of no DCM infiltration into the crystal structure.

Results on the $(110)_t$ cuboid perovskites include the 4,4'-bis(trifluoromethyl)-2,2'-bipyridine adsorption and ligation with surface lead. Based upon data fitting in CasaXPS and rough estimation using the area under the curve for each fluorine and iodine of 82 and 3812 cps ev, gives a signal ratio of 0.022. This points to an approximate surface coverage of 10%. This is significantly higher than results on either the $(100)_t$ or $(112)_t$ facets. The XP spectra from the bpy adsorption on the cuboid $(110)_t$ perovskite can be seen in Figure 38

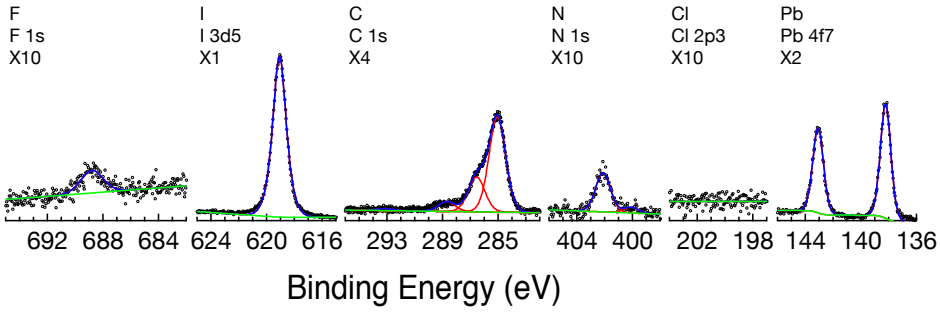

Figure 38. XP spectra of a $MAPbI_3$ cuboid perovskite $(110)_t$ surface after exposure to a solution of 4,4'-bis(trifluoromethyl)-2,2'-bipyridine. This distinct fluorine signal is indicative of adsorption on the surface due to lead exposure. The lead spectrum shows no reduced or oxidized lead and appears as expected.

6.4. SEM Imaging

The cuboid perovskite $(110)_t$ facets are significantly more textured and varied than the $(100)_t$ facet seen in the prior SEM. This is hypothesized to be the source of the heightened signal intensity and calculated coverage of the BF_3 adsorption experiments. Cuboid perovskite SEM can be seen in Figure 39. Similarly, these perovskites exhibit defects over the surface.

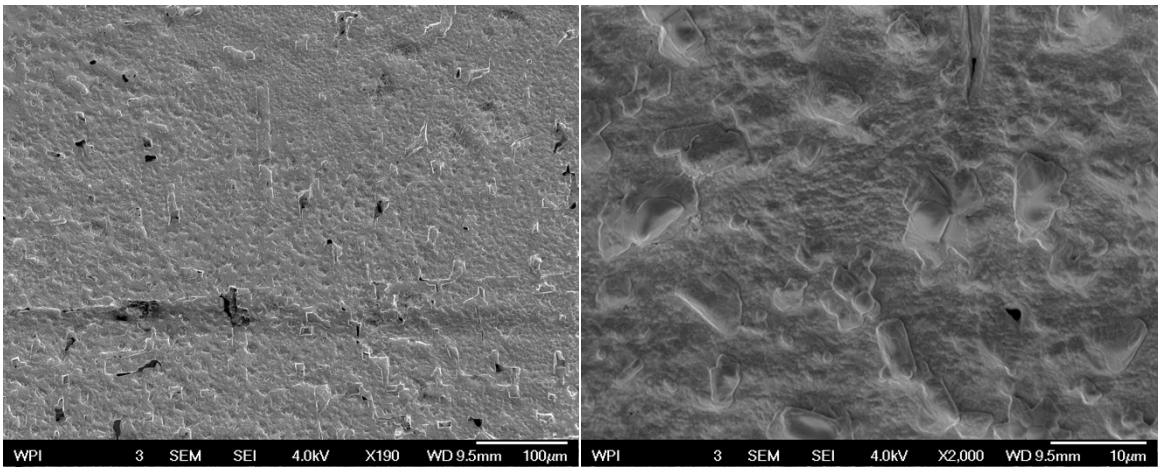

Figure 39. Top-down SEM images at. 190X and 2000X magnification (left and right respectively) show texturing on the cuboid perovskite $(110)_t$ surfaces. Features range from several microns to sub-micron in size.

Chapter 7. Discussion

7.1. Basicity and Surface Halide Reactivity

XP spectra indicate a reaction between solution-phase BF_3 and the perovskites under study. As a Lewis acid, BF_3 forms adducts with Lewis bases with electron donating species, which should herein be the respective halide in each perovskite but could additionally be oxygen due to a deleterious formation of interfacial metal oxides. Notably, the Pb 4f regions of each $MAPbI_3$ utilizing a halide targeting reagent sample in Figures 8, 9, 16, 17, 21-24, and 31-33 show no chemical features ascribed to highly oxidized lead that would indicate interfacial lead oxide or lead hydroxide species. This is important since an oxide or hydroxide species would provide an additional handle for BF_3 adsorption, resulting in a false positive when probing the halide site.

A model consistent with the data for BF_3 adsorption on oxide-free or minimally oxidized perovskite surfaces involves the formation of a Lewis adduct between adsorbed BF_3 and surface-exposed halides. Figure 9 presents cartoon representations for BF_3 adsorption via Lewis-adduct formation to an iodide on a $MAPbI_3(100)_t$ surface. Both the cubic and tetragonal forms of these ABX_3 perovskites have alternating $(100)_t$ -parallel layers consisting of AX stoichiometry and of BX_2 stoichiometry. This model assumes that the perovskites “end” with an AX layer presented at the surface, which would be consistent with the surfactant effects of a methylammonium cation on $MAPbI_3$. This, the model in Figure 40 is consistent with an adsorption of one BF_3 per perovskite unit cell area that we define as one complete monolayer of adsorption on a perovskite $(100)_t$ face.

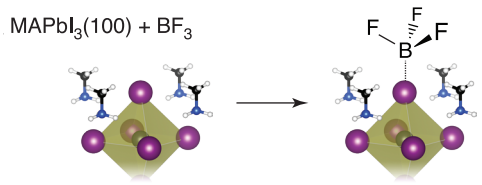

Figure 40. The proposed model for the adsorption of BF_3 at perovskite surfaces involves the formation of a Lewis adduct of the adsorbed BF_3 with interfacial iodide on $MAPbI_3$. Atom colors follow C: black, N: blue, H: white, I: purple, Pb: gray.

Importantly, the interaction with BF_3 and $MAPbI_3$ demonstrated significantly different behavior between exposures at 25 °C and at 40 °C. The substrate overlayer model discussed above assumes one "perfect" monolayer as presented in Figure 40, and the results for BF_3 at 25 °C are consistent with sub-monolayer adsorption of 40 ± 5% on $MAPbI_3(100)$. In contrast to a 25 °C reaction, the interaction between BF_3 and $MAPbI_3$ at 40 °C yielded significantly more fluorine than would be expected for one monolayer of adsorption. The increased BF_3 coverage for 40 vs 25 °C treatments is notable as the single-crystal $MAPbI_3(100)_t$ samples are very smooth as noted in the SEM imaging mentioned later in the paper. As mentioned above, we discount the possibility of BF_3 multilayer formation due to the weak interactions between BF_3 molecules. An alternative pathway to strong F 1s signals is the near-surface infiltration of BF_3 into the $MAPbI_3$ crystal. Notably, the 40 °C reaction temperature remains below the ~54 °C tetragonal-to-cubic phase change temperature,[63–65] however BF_3 is a small, flat molecule (certainly compared to the other reagents presently under study) and some nominal solvent-assisted surface restructuring may occur near this phase change temperature. Quantification of such phenomena merits future study. We do not utilize the overlayer equation to assign a BF_3 coverage for the 40 °C treatment as infiltration creates a

nonbounded problem for an overlayer models with unknown BF_3 quantities and distributions below the surface. The possibility of near-surface structural rearrangements for $MAPbI_3$ at temperatures approaching its phase-transition temperature is supported by findings in the related publication.[66]

The experiments on alternate surfaces are exploratory and present additional challenges and area to investigate further as has been done on the $(100)_t$ surface. The $(112)_t$ experiments show that this surface is also terminated with iodide similarly to the $(100)_t$. The thin films are likely terminated with iodide. These surfaces should be compared to untreated films deposited on FTO. These were not extensively examined, but do provide the foundation and initial data to proceed with a precedent in place.

The cuboid $(110)_t$ perovskite surface exhibits very similar behavior to the $(100)_t$ surface. Direct comparisons between the untreated and the BF_3 treated surface display adsorption. The easily accessed $(110)_t$ perovskite facet on the cuboids is ideal to work with for its relevancy in thin-film materials.[67] The surfaces are textured to a higher extent than the GBL, inverse temperature crystallization method perovskites compared in this document. The GBL perovskites are however processed with sequential mechanical and chemical polishing steps to produce smooth, low defect surfaces. The mechanical polishing has not been applied to the cuboid perovskites yet and it would likely result in similar surface feature profiles.

Desorption results elucidate the nature of the interfacial Lewis adduct on the perovskite surfaces. Desorption likely follows first order kinetics as one bond needs breaking with no bond reformation as occurs in second-order desorption (*e.g.* hydrogen

from metal surfaces). The roughly monolayer quantities likely discount the possibility of zero-order desorption as occurs from large, thick samples (*e.g.* multilayer adsorbed water). Thus, the estimated activation energy for BF_3 thermal desorption serves as a direct proxy for adsorbate-substrate bond strengths.[54] At ~200–215 kJ mol^{-1}, the BF_3–X^- adduct bond strengths quantified herein are roughly half as strong as the average strength of a C–H covalent bond and significantly stronger than a typical hydrogen bond. Of note, the proximity of the BF_3 desorption signal to the decomposition feature of the $MAPbI_3$ in Fig. 3B suggests that the BF_3–I^- adduct has a bond strength that is comparable to the ionic bonds holding $MAPbI_3$ together itself.[58] The large desorption signal in frame A that aligns more closely to features in frame B associated with substrate decomposition in contrast to the sub-monolayer BF_3 desorption feature supports a model of infiltrated BF_3 that is liberated concomitantly with $MAPbI_3$ decomposition.

The fundamental adsorbate interaction strength experiments with the phenylborane compounds is the next area of study for these materials. The problem has been bounded between tris(pentafluorophenyl)borane and triphenyl borane. Synthesis and application of various substituted fluorophenyl borane compounds to “fine-tune” the activation energy between these molecules will be useful to determine how reactive the iodide at the surface is. Grignard reagents and techniques can be used to synthesize the compounds. These will be applied to the surface using the same techniques as done in the BF_3 experiments. The analysis using XPS and TPD will proceed similarly to the BF_3 experiments as well. The fragmentation of the phenylborane may need to be identified using the “analog” scan program on the TPD instrumentation. The

tris(pentafluorophenyl)borane ionization fragmentation is on file in the TPD data files or in Sasha's Thesis. The fragment that is visible in the TPD aligns with a pentafluorophenyl cation. It is hypothesized that the less substituted phenylboranes will fragment similarly, but should be identified experimentally. The manual temperature control and analog scan programs are used separately and the LabView program to sew the data together is used to interpret the data.

7.2. Ammonium exchange

Photoelectron spectra following the reaction of *p*-trifluoromethylanilinium chloride with $MAPbI_3$ demonstrated observable F 1s signals but no corresponding Cl 2p features. Accounting for the anticipated Cl 2p features shown in the traced spectra for Cl 2p in Figure 11, the absence of interfacial chlorine is important for the mechanism of reaction. This implies that step-wise synthesis, processing, and functionalization without detrimental compositional changes is possible. Figures 11, 12, 15, 25-30, and 34-36 all show the various ammonium exchange experiments.

We propose a model in which *p*-trifluoromethylanilinium cations exchange for the A-type cations on each perovskite surface, *i.e*. interfacial methylammonium on $MAPbI_3$. A-type cation substitution during crystal growth has yielded interesting and altered perovskite structures.[68–70] Here, if *p*-trifluoromethylanilinium species simply adsorb to a surface with no cation exchange, we would expect chloride anions to counter the anilinium cation charge. Rather, the absence of detectable Cl 2p features is consistent with an exchange in which a given amount of A-type cations exchange for anilinium species with the solution-phase chloride anions that serve to counter the charge of the newly dissolved

methylammonium or cesium. That such an anilinium exchange occurs further implies that there are A-type cations available at each perovskite surface for possible exchange.

Figure 41 presents a cartoon representation of the *p*-trifluoromethylanilinium model for $MAPbI_3$. As with the model in Fig. 38, if a $(100)_t$ -parallel face is terminated by a layer with AX stoichiometry, then exchange for one anilinium cation per cubic unit cell or two per tetragonal unit cell corresponds to complete monolayer coverage. Yields of A-type cation exchange for the fluorinated anilinium species are sub-monolayer for $MAPbI_3$.

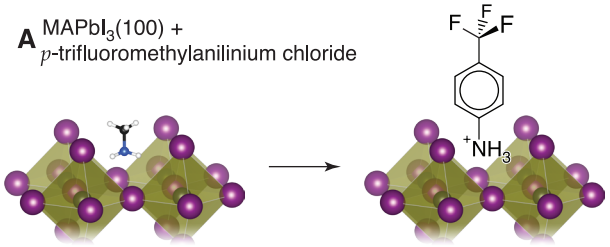

Figure 41. The proposed model for the reaction of *p*-trifluoromethylanilinium chloride with $MAPbI_3(100)_t$ (frame A). In the model, reactive adsorption yields an exchange for the A-type cation in the ABX3 perovskite surface, to yield a *p*-trifluoromethylanilinium cation at the surface.

Photoelectron spectra of perovskite $(112)_t$ surfaces after exposure to *p*-trilfuoromethylanilinium chloride demonstrate observable fluorine 1s electron signal without significantly discernable chlorine 2p electrons indicating that this facet is also capable of undergoing surface exchange.

Interestingly, photoelectron spectra indicate that the $(110)_t$ facet does not exchange ammonium groups, or at least not in comparable quantities to the $(110)_t$ or $(112)_t$ facets. This is interesting and will need further study to understand the makeup of this facet in greater detail. When this reaction has been tried at elevated temperatures for extended periods of time, the chlorine spectrum increasingly exhibits a clear chlorine

doublet not commensurate with any increase in fluorine. This increase is hypothesized to be from dichloromethane diffusing into the crystal at higher temperatures due to increased molecular vibrations as it approaches the lattice transition at about 56 °C.

Photoelectron spectra of perovskite $(100)_t$ facets after exposure to 2,2,2-trifluoroethylammonium chloride demonstrate observable fluorine 1s electrons with minimal if any discernable chlorine 2p electrons. This indicates that other ammoniums are able to exchange at the surface. This is significant for functionalization strategies involving the ammonium site. Both phenyl and alkyl ammoniums are implicated as being capable of exchange without anion exchange. The combination of these results presents a useful route to functionalize the surface after the material has been synthesized and processed.

Thiophene functionalized ammonium compounds have been unsuccessful as functional groups on the surface. The 2-thiophene methylamine hydrochloride has an extremely low limit of solubility in perovskite-safe solvents and this may be the source the lack of surface exchange. Acetonitrile is the only tested solvent with significant ability to dissolve the 2-thiophene methylamine hydrochloride but this resulted in the partial dissolution of the perovskite. Alternative counteranion salts were unsuccessful for surface exchange with the hexafluorophosphate salt showing no observable sulfur and tetrafluoroborate salts proving difficult to isolate. Varying the alkyl chain bridge length or number of thiophenes in the chain may impart enough nonpolar solubility to allow for perovskite-safe solvents to dissolve the material for surface exchange. Exchange may also be possible using a similar technique to the methylamine gas induced defect healing

method.[32] The 2-thiophene methylamine is a liquid with a low volatility, the liquid can be volatilized using reduced pressure and elevated temperature if necessary for sufficient gas phase exchange.

7.3. Metal Ligation

$MAPbI_3$ demonstrates minimal if any adsorption of the 4,4'-bis(trifluoromethyl)-2,2'-bipyridine ligand. XP spectra detects no fluorine signal for the reaction of the fluorinated bpy compound with $MAPbI_3(100)_t$, suggesting at most a trace adsorption of the bpy species below the limits of detection. Separate experiments on $MAPbI_3(110)_t$ demonstrate adsorption of this fluorinated bpy in small quantities in preliminary investigations, which obviates a concern that the fluorinated bpy simply ligates too weakly with interfacial Pb^{2+} for observation with the presently employed methodology and additionally there is precedent in the literature that bipyridines ligate with Pb^{2+}.[71,72] The bpy experiments on the different facets in Figure 13, 37, and 38 show representative spectra for each of the examined facets. Figure 42 is a carton representation of the bpy ligation on the $(100)_t$ $MAPbI_3$ surface.

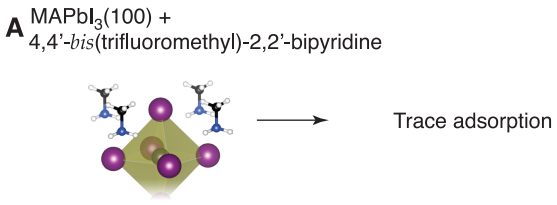

Figure 42. Exposure of $MAPbI_3(100)_t$ to the fluorinated bpy compound yields at most trace adsorption with no significant reaction.

The bpy ligation model above is further consistent with the absence of observed ligation at $MAPbI_3(100)_t$ surfaces. With the expectation of $MAPbI_3(100)_t$ presenting an AX layer that in practical terms would be rich in methylammonium iodide and deficient in lead iodide, near-interfacial lead cations should be ideally octahedrally coordinated as in the bulk. Further, the methylammonium species itself should demonstrate a mild surfactant effect that would decrease the driving force for methylammonium iodide dissolution to reveal Pb^{2+} for ligation.

The bpy ligand did not adsorb onto the perovskite $(112)_t$ facet similarly to the $(100)_t$. XP spectra do not detect any fluorine, supporting no reaction or surface adsorption. This result is contrary to the expected outcome since it is expected that lead will be exposed on part of the surface. When considering the TXRF experiments and the increased lead signal when compared to the blank. This may imply that the exposed lead on the surface when ligated with the bpy compound, is dissolved back into solution. The higher signal in the crushed perovskite experiment is expected due to the much greater surface area and exposed corners and edges.

The preliminary examinations of the bpy ligation with the $(110)_t$ facet demonstrate a small, yet straightforwardly definitively measurable fluorine signal, which is unique to the $(110)_t$ facet. This is indicative of some bpy reactive lead on the antisolvent synthesized $(110)_t$ facets.

7.4. Atomic Layer Deposition Handles

Multiple reagents were examined as potential chemical handles for atomic layer deposition on the $MAPbI_3$ perovskites. Boric acid, 4-trifluoromethylphenyl boronic acid, pinacol ester, and 4-aminobenzoic acid hydrochloride were all examined as

functionalization strategies. Boric acid and 4-trifluoromethylphenyl boronic acid, pinacol ester were both targeting the halide and the 4-aminobenzoic acid hydrochloride utilizes the ammonium exchange mechanism. As seen in the results, neither strategy targeting the halide was successful. We believe that this is due to insufficient acidity of the boric acid and that the 4-trifluoromethylphenyl boronic acid, pinacol ester is either not acidic enough or both too sterically encumbered to react with the surface. The 4-aminobenzoic acid hydrochloride is likely able to exchange. The XPS data shows no chlorine which is expected based on the exchange mechanism. The IRRAS data shows that there is a definite change on the surface following exposure to a solution of the ammonium salt for exchange. There is however a water signal that would appear to overshadow the signals that are desired. This is likely due to the hydrophobicity of the carboxylic acid groups. One option to try remedying this issue is to carefully heat the sample in an oven to desorb some of the water, which may allow the desired signals to rise above the adsorbed water.

The unsuccessful reagents used in this section provide valuable data for planning more successful functionalization route in the future. Boric acid appears to be not useful as a single layer reagent but could deposit boron oxide films if the solvent isn't specially prepared to be dry and degassed. The 4-trifluoromethylphenyl boronic acid, pinacol ester did not have sufficient reactivity to adsorb on the surface. This indicates that a sufficiently strong reagent is needed to interact at the surface. A more fluorinated substituent can be used to increase the acidity of the boron center. This would be a possible route to make this reaction more favorable. Ammonium substitution with carboxylic acid functionalized groups would be useful chemical handles for ALD. Further refinement of the method,

perhaps different conditions will help the exchange to achieve higher coverage to produce unambiguous results. Heating the sample to desorb any adsorbed water prior to analysis in the IRRAS may improve the results. Exchange using 5-ammonium isophthalic acid also presents a straightforward method to significantly increase the available carboxylic acid groups to observe in both XPS and IRRAS. Depending upon the rotation of the molecule and carboxylic acid group, this may significantly help or hinder the visibility in the IR.

7.5. Implications

The presented reaction chemistry enables several routes through which solution-phase treatments may yield improved atmospheric stability, minimization of surface states, and dipole-based control of band edges. Lewis adduct formation, interfacial A^+-type exchange, and B^{2+}-type cation-ligand complex formation each represent a chemical handle for subsequent reaction chemistry. One application of present interest may be the post-synthesis formation of Ruddlesden-Popper phases on wide-area, single-crystal substrates enabled by exchange of a methylammonium cation for a long-chain diamine onto which 2D perovskites may be synthetically grafted. A deeper understanding of chemical conversions within and initiated at adsorbates represents one particularly underexplored area worthy of future study. The ability to graft a polymer-initiating species for cross-linking an atmospheric stabilizer or for chemically growing a conducting polymer contact remains tantalizing.

The $MAPbI_3$ perovskites have demonstrated reactivity at the A^+, B^{2+} and X^- sites with many experiments targeting the $(100)_t$ face, preliminary studies were carried out on the $(112)_t$ facet, and BF_3 was observed on the $(110)_t$ facet. Substitution at the A site can be accomplished using ammonium halide reagents without disrupting the sub-surface

composition of the perovskite. Adsorption of a Lewis and the subsequent formation of Lewis adducts revealed adsorbate bond strengths that are comparable to the strength of interactions holding $MAPbI_3$ together itself. This is implicated in TPD experiments and the observation of a thick lead iodide layer post-heating. The loss of methylammonium is hypothesized to be the driving force for the BF_3 desorption. Reactions with a bipyridine-based ligand demonstrated no observable reaction on $MAPbI_3(100)_t$ that would be consistent with a lead-deficient and methylammonium iodide-rich surface. The adsorption of the bpy ligand on the $(110)_t$ facet would indicate that this crystal face has a greater degree of lead rich termination and in combination with the anilinium exchange, poor in surface exchangeable methylammonium.

Chapter 8. Bilayer Graphene Dye Sensitized Solar Cell

This chapter details progress made during the rotation in the group when preliminary work on the dye-sensitized graphene solar cell was conducted and developed. This work focuses on creating a polymer coating on the monolayer graphene on copper foil, transfer from the foil onto a silicon wafer, then initial experiments at doping the graphene with benzyl viologen and zinc phthalocyanine dye.

8.1. Overview

Graphene possesses many interesting and superior electronic, optical, and physical properties. These properties may be tapped to produce a dye-sensitized solar cell (DSSC). Solar energy is a strong contender to be at the forefront of next generation energy production and DSSC's have the capability to be inexpensive, scalable, and highly tunable.[23,24,73] Low-cost, tunable, safe solar power will be a revolutionary force in both the energy and economic landscape.[74] The benefits and broad societal goals inspire this work to develop DSSC based on a graphene architecture. Graphene's electronic properties involve the Dirac Cone, which describes the electron behavior, and methods of doping to shift the electronic properties of the material to be either p or n type.[24–26] Doped graphene that is stacked has been shown to make successful lateral type p-n junctions, showing asymmetric rectifying behavior.[23] This combination of prior work and knowledge exposes the knowledge gap of a DSSC comprised of a graphene p-n junction combined with a dye sensitizer.

Graphene doping is a core aspect of this project as this is what will impart the p or n-type behavior to the graphene. Raman spectroscopy has precedent in observing graphene shifts in the G band and 2D band on a Si/SiO_2 (300 nm) substrate, interpreted as a ratio (I_{2D}/I_G) where the intensity of the G band decreases with either type of doping.[25]

This is in part due to the Dirac point shift away from zero, which is where the graphene either gains its n or p characteristics. The charge separation when combined with the dye excitation is hypothesized to be a capable solar cell.

8.2. Experimental

8.2.1. Materials

Materials unique to this project include single-layer chemical vapor deposited graphene on copper foil (Graphene Supermarket, Calverton, NY), ferric chloride hexahydrate ($FeCl_3$, Sigma-Aldrich, 98%), and zinc phthalocyanine (ZnPc, Aldrich, 98%), pyrrole (Alfa Aesar, 98+%), benzaldehyde (Alfa Aesar, 99+%), propionic acid (Acros Organics, ACS reagent), polymethylmethacrylate 550K (Alfa Aesar), polymethylmethacrylate 35K (Acros Organics),benzyl viologen dichloride (Alfa Aesar 97%), sodium borohydride, tetrahydrofuran.

8.2.2. Methods

8.2.2.1. Transfer

Polymethylmethacrylate was examined in a series of solvents for the optimal coating mixture for the graphene transfer. A 4% by weight solution in methanol, toluene, diethyl ether, acetonitrile, chlorobenzene, and anisole were all examined with chlorobenzene being the best choice. Anisole and toluene are suitable although toluene only works with the 550 K polymer.

The graphene transfer steps closely follow work published by Nielander et al..[22] The 550 K polymethylmethacrylate in chlorobenzene solution was drop-cast onto a

square of graphene on copper foil. A spincoater was used to achieve even polymer coating at 2000 RPM, 500 acceleration, for 60 seconds. The graphene sample was annealed on a 185 °C hotplate for 10 minutes. The sample was allowed to cool briefly before being coated a second time using the same process. The second polymer coating results in a more uniform and visible film, which simplifies the transfer step. The copper foil was dissolved in a 40% by weight ferric chloride solution- 1% hydrochloric acid solution in a shallow petri dish. The time varies widely with most dissolutions taking 1-2 hours. The graphene was then transferred to n-type single-side-polished silicon that had been etched with hydrofluoric acid (Caution! Dangerous reagent). Three successive rinses in 18 MΩ deionized water to rinse the iron chloride solution and a final submersion in acetone to remove the polymethylmethacrylate coating. The silicon was dried on an 80° C hotplate for 10 minutes. The graphene on silicon was transferred to a glass tube sealed with ultra-torr fittings. A gentle stream of forming gas (5% H_2:95% N_2) was passed over the sample to reduce the graphene for 8 hours at 300 °C.

8.2.2.2. Doping

Benzylviologen in its dichloride form is not suitable to dope the graphene surface. Benzylviologen dichloride (0.041 g, 0.0001 mol, 1 eq.) was dissolved in 10 mL of deionized water, 10 mL of toluene was added making a biphasic solution. Sodium borohydride (0.0757 g, 0.002 mol, 20 eq.) was added to the biphasic benzylviologen dichloride solution, mixed and allowed to react overnight. The reaction immediately turned

maroon and shifted towards orange and finally golden yellow the next day. The aqueous phase was bubbling initially and ceased the next day.

The reduced benzylviologen was dropcast onto the reduced graphene on silicon using the same spincoating procedure as the polymethylmethacrylate. The sample was annealed at 100 °C for 10 minutes. The appearance became hazier following the annealing step.

The following experiments were planned but not conducted. The dyed-doped-graphene layer will be capped with a second graphene layer creating the graphene bilayer structure. This second layer of graphene will examine the same procedure used previously. This second layer will be p-type and doped with a gold trichloride solution in nitromethane.

8.2.2.3. Dyeing

Tetraphenylporphyrin was synthesized using a commonly available preparation used in many synthesis laboratory courses. In a three-neck flask, 300 mL of propionic acid was added two necks were stoppered with rubber septa and one stoppered with a condenser. The acid was heated to reflux after which, benzaldehyde (10.5 mL, 10.96 g, 0.103 mmol, 1eq.) was added. Pyrrole (10 mL, 9.67 g, 0.144 mmol, 1.4 eq.) was added dropwise. A color change to golden-brown was observed. The reaction was allowed to proceed at reflux for 30 minutes. The mixture was vacuum filtered and washed with 10 mL of methanol and 300 mL of boiling water, yielding 2.312 g of bright blue

tetraphenylporphyrin (14.5% yield). This material was not used for dyeing the graphene, but served as a valuable synthetic experience in making porphyrin materials.

Zinc phthalocyanine was examined in anisole at its saturation point. The benzylviologen doped graphene samples were examined using both 30 minute and overnight bath depositions of zinc phthalocyanine.

8.2.2.4. Tips

Working with the graphene presents its own challenges and hurdles due to the low optical absorption and flexibility of the copper substrate. Cutting the copper foil with the graphene should be done using a clean razor specific for the graphene to prevent any cross-contamination. Mounting the sample on the spin coater also requires an additional valve to leak vacuum due to the fact that the house vacuum is too strong and can damage the foil, folding it inwards. This is undesirable for producing a uniform PMMA layer. A valve can be connected between the vacuum port and the house vacuum outlet and can be adjusted from there to produce the proper suction to hold the sample down during the spin coating without damaging the sample.

Etching the silicon wafers is hazardous as it uses hydrofluoric acid solutions. Proper training and technique should be in place prior to use. Alert others to the use of hydrofluoric acid and know both where the emergency calcium gluconate gel for topical application and the calcium gluconate eye wash for the eyes. These should be checked regularly and alert the environmental health and safety office when they are within 3 months of expiration since it is important to have on hand.

8.3. Results

8.3.1. Transfer

Graphene transfer was tested using both 35K and 550K polymethylmethacrylate in methanol, toluene, diethyl ether, acetonitrile, chlorobenzene, and anisole. Chlorobenzene is the best overall solvent with good solubility forming a viscous solution at 4% by weight. The 550K forms better films that are easier to handle and see during the

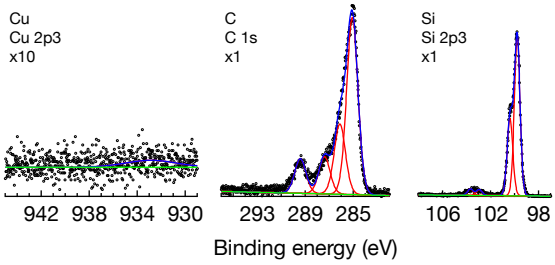

Figure 43. XP spectra of copper, carbon, and silicon for a sample that had undergone the aforementioned transfer procedure. No discernable copper from the foil is visible meaning that it was completely removed. There are multiple carbon sources from adventitious carbon and graphene. The silicon with some oxide is present.

transfer and processing. The second application increases the uniformity of the film, this is likely due to dissolving and reforming of the polymer layer. Chlorobenzene is additionally more volatile than anisole, which is beneficial in producing thin films. A single spin coat of the polymer is uneven and does not provide adequate visibility for transfer stages. XP spectra of graphene deposited and annealed in the forming gas furnace can be seen in Figure 43. No residual copper is visible and there is a large amount of carbon as expected.

8.3.2. Doping

Reduced benzylviologen treatment on graphene over silicon did not yield an appreciable nitrogen signal. This may be due to insufficient intermolecular attraction to connect with the surface. The XP spectra from the reduced benzyl viologen experiment can be seen in Figure 44. Reduced Benzyl Viologen treated graphene on silicon exhibits

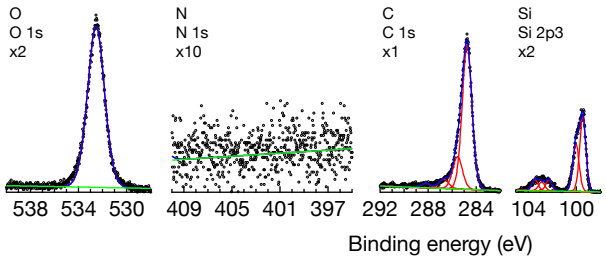

Figure 44. Reduced Benzyl Viologen treated graphene on silicon exhibits no discernable nitrogen signal, which should be discernable albeit small. The carbon, silicon, and oxygen signals are as expected.

no discernable nitrogen signal, which should be discernable albeit small. The carbon, silicon, and oxygen signals are as expected.

8.3.3. Dyeing

Three different attempts to deposit zinc phthalocyanine on the reduced graphene on a silicon substrate yielded successful results. One trial with a 30-minute deposition had nominal zinc signal and a clear nitrogen signal. The overnight depositions possess a distinguished zinc signal and very clear nitrogen. This implies that the zinc phthalocyanine dye molecule can adsorb strongly enough onto graphene to survive pumping into a UHV environment and will likely be able to have a second layer of graphene stacked onto it. The two overnight exposures both have stronger zinc and nitrogen signals. The XP

spectra for the 30-minute and overnight exposures can be seen in Figure 45. Longer deposition time results in increased coverage as clearly seen in the XPS data.

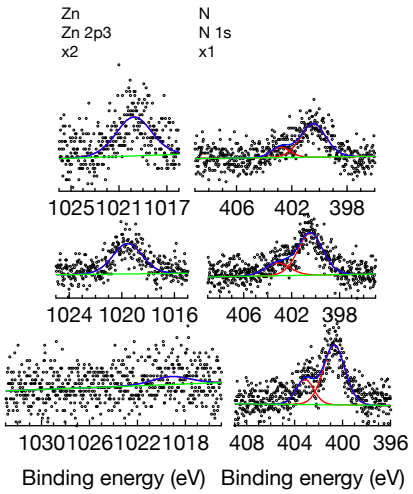

Figure 45. Zinc phthalocyanine dye depositions for overnight (top and middle) and 30-minutes (bottom). The zinc signal significantly increases in the overnight samples. The nitrogen becomes more defined in the overnight experiments when compared to the 30-minute sample.

8.4. Discussion

The progress made on the doped graphene DSSC will serve as a stepping stone towards further development and refinements. The benzylviologen doping will likely be aided by larger substituents beyond the benzyl group including pyrene or other polycyclic aromatic hydrocarbons to increase the pi stacking interactions with the graphene. Porphyrin, phthalocyanine, and substituted bipyridine dyes will be examined for their adsorption on the graphene and impact on the electronic properties of the dye sensitized p-n graphene bilayer photocell. The gold trichloride (p-type) doping was not attempted

but can be examined in a straightforward manner These studies will aid in the proof that DSSC doped graphene can make a thin, highly tunable solar cell for niche applications. These cells may find practical application as tandem absorbers or as a value-added substitute in niche applications while producing electricity.

8.5. Conclusion

Thin-film graphene-based dye-sensitized solar cells would be a strong contender as a form of DSSC technology. Improvements in graphene production and processing would open this material up as a low cost, highly tunable material that would see use in diverse applications where graphene's unique properties are needed.

Chapter 9. Conclusions and Outlook

Photovoltaic technology is poised to be one of the most significant sources of energy as demand continues to increase. The work presented in this thesis stands as groundwork pointing forward towards the next generation of photovoltaic technology including the broad perovskite class of semiconductor and beginning exploratory work on graphene-based techniques. The $MAPbI_3$ perovskites have demonstrated reactivity with a variety of reagents without deleterious effects causing compositional changes or degradation. There are inherent issues with the $MAPbI_3$ perovskites such as long-term environmental stability and its lead content however, there are techniques to remedy these flaws and are the target of future investigations related to this work. Utilizing the research in this paper to understand the surface and apply suitable functional groups that are chemically compatible.

Surface chemistry utilizing similar orthogonal reaction techniques can be used to further understand this material and does merit future investigation. From a fundamental standpoint, the same techniques applied extensively on the $(100)_t$ facet can be applied to the $(112)_t$ and $(110)_t$ surfaces that have been given preliminary studies. This will provide data on surface termination conditions and reactivities on each facet respectively. This will provide an interesting vantage point to compare and contrast the surface termination and the impact that it has on the properties observed. The facet planes can be seen in Figure 46. The different crystal lattice planes under examination in this paper ($(100)_t$, $(110)_t$, and $(112)_t$ from left to right). The $(100)_t$ is the predominant facet that was examined with preliminary work done on both the $(112)_t$ and $(110)_t$ facets. There is a lot of room to

examine the $(112)_t$ and $(110)_t$ by fully examining their facets with the same reactions used on the $(100)_t$ and developing new techniques using the knowledge gained. These crystal planes exhibit different surface terminations and it could be hypothesized that they will exhibit different results. A tetragonal unit cell is outlined.

Figure 47. XP spectra for both a (100) and a (112) perovskite (first two rows and second two rows respectively). Both perovskites exhibit ammonium exchange as seen in prior experiments at ambient temperatures. The difference in this case is the elevated temperature and the appearance of a significant signal in the chlorine region. These scans were not scaled relative to iodine as other figures have been.

Figure 48. XP spectra for both a (100) and a (112) perovskite (first two rows and second two rows respectively). Both perovskites exhibit ammonium exchange as seen in prior experiments at ambient temperatures. The difference in this case is the elevated temperature and the appearance of a significant signal in the chlorine region.Figure 49. The different crystal lattice planes under examination in this paper (100, 110,and 112 from left to right). The 100 is the predominant facet that was examined with preliminary work done on both the 112 and 110 facets. There is a lot of room to examine the 112 and 110 by fully examining their facets with the same reactions used on the 100 and developing new techniques using the knowledge gained. These crystal planes exhibit different surface terminations and it could be hypothesized that they will exhibit different results. A tetragonal unit cell is outlined.

Figure 50. XP spectra for both a $(100)_t$ and a $(112)_t$ perovskite (first two rows and second two rows respectively). Both perovskites exhibit ammonium exchange as seen in prior experiments at ambient temperatures. The difference in this case is the elevated temperature and the appearance of a significant signal in the chlorine region. These scans were not scaled relative to iodine as other figures have been.

Figure 51. The different crystal lattice planes under examination in this paper ($(100)_t$, $(110)_t$, and $(112)_t$ from left to right). The $(100)_t$ is the predominant facet that was examined with preliminary work done on both the $(112)_t$ and $(110)_t$ facets. There is a lot of room to examine the $(112)_t$ and $(110)_t$ by fully examining their facets with the same reactions used on the $(100)_t$ and developing new techniques using the knowledge gained. These crystal planes exhibit different surface terminations and it could be hypothesized that they will exhibit different results. A tetragonal unit cell is outlined.

Figure 52. XP spectra for both a (100) and a (112) perovskite (first two rows and second two rows respectively). Both perovskites exhibit ammonium exchange as seen in prior experiments at ambient temperatures. The difference in this case is the elevated temperature and the appearance of a significant signal in the chlorine region. These scans were not scaled relative to iodine as other figures have been.

Figure 53. XP spectra for both a (100) and a (112) perovskite (first two rows and second two rows respectively). Both perovskites exhibit ammonium exchange as seen in

prior experiments at ambient temperatures. The difference in this case is the elevated temperature and the appearance of a significant signal in the chlorine region.Figure 54.

Additionally, ultraviolet photoelectron spectroscopy can be used to examine the band edge shift that occurs when different surface functionalization groups are employed. The significance here is that it will open up a deeper fundamental knowledge of band gap engineering the material for specific future applications. Applied functionalization will take advantage of the techniques investigated in this paper in addition to new techniques to achieve a specific goal. The first route that I propose is utilizing the 4-aminobenzoic acid and 5-aminoisophthalic acid as functional groups. The carboxylic acid groups are hypothesized to be viable chemical handles for atomic layer deposition. In conjunction

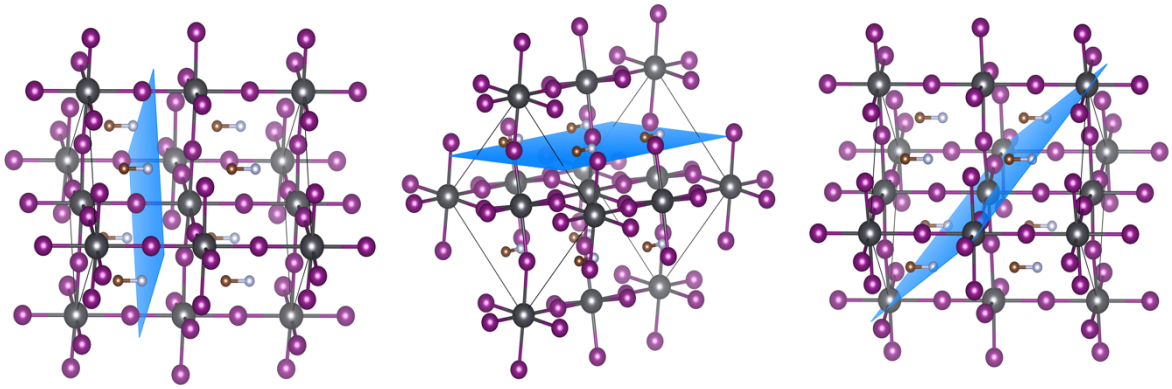

Figure 46. The different crystal lattice planes under examination in this paper ($(100)_t$, $(110)_t$, and $(112)_t$ from left to right). The $(100)_t$ is the predominant facet that was examined with preliminary work done on both the $(112)_t$ and $(110)_t$ facets. There is a lot of room to examine the $(112)_t$ and $(110)_t$ by fully examining their facets with the same reactions used on the $(100)_t$ and developing new techniques using the knowledge gained. These crystal planes exhibit different surface terminations and it could be hypothesized that they will exhibit different results. A tetragonal unit cell is outlined.

with this study, the 3-aminobenzoicanhydride will be a valuable addition to gain insight into the surface orientation of adsorbed species making use of IRRAS. These strategies pose an interesting first look into a functional molecule towards direct ALD chemical handles. Exploring expanded bridges to connect diagonal and spaced out sites also

poses an interesting are of study. A possible avenue for a molecule could be based on benzene propanoic acid, β-hydroxy-3-nitro, following similar coupling and reduction techniques. The synthesis of this molecule has a reasonably high yield, stereoselective on the alcohol and uses a biocatalyst.[75] Another possible reagent is a double bond containing 2-propenoic acid, 2-hydroxy-3-(-nitrophenyl)- molecule for coupling and has been synthesized in the following citation.[76] A naphthalene system with amine and carboxylic acid may also present a useful system with a possible target of 2-napthalenecarboxylic acid, 5-amino- as the functionalizing molecule. There are functional groups that can be examined on the ring system. The shorter bridge can be accomplished using 3-nitro-benzene acetic acid. Functionalization through the ammonium site with terminal double-bonds and subsequent polymerization may form protective layers over the perovskite surface. Electronic contacts utilizing substituted thiophenes through the ammonium site has promise as a hole transporter. This would be advantageous as a more efficient direct contact in comparison to more traditional hole transport layers such as Spiro-OMaTAD, which do not form direct chemical bonds with the surface. As mentioned in Chapter 5, thiophene functionalization has been unsuccessful thus far, but there are many promising routes to try making it work. Varying the substituent length, on both the amine side and thiophene chain can impart solubility changes that may be beneficial. Controlled gas phase exposure of the amine may also be a viable option to functionalize the surface in a manner similar to how methylamine can be used for grain reformation.[32] The hypothesized increased uniformity, stability, and efficiency would greatly benefit the application of these materials. The formation of Ruddlesden-Popper

phases is another interesting avenue to examine. Layered perovskites exhibit different bandgaps and in combination with bandgap tuning as elucidated by fundamental UPS research, may expand the already versatile tunability of perovskite semiconductors. These methods can also be applied to methylammonium lead bromide ($MAPbBr_3$) to compare the reactivity of another material with a single compositional change. In particular, this would present a valuable opportunity to examine the interaction strength between the halide and BF_3 to identify trends in surface reactivity with varying X site components. The direct comparison by varying a single component will prove to be valuable as an expansion on the fundamental understanding of surface reactivity. The culmination and expansion of the surface understanding to include greater tunability and structural knowledge may enhance the position that perovskites occupy as a promising next-generation photovoltaic material.

Additional Data and Recent Work

High temperature reaction conditions for the $MAPbI_3$ perovskites (such as 40 °C and above) can yield undesired results when using DCM as the solvent. Chlorine has been observed on numerous occasions when DCM is employed as the solvent at elevated temperatures. Contrary to the earlier figures that oftentimes use DCM but under ambient conditions. One example of such data, despite not being scaled, can be seen in Figure 52. Numerous experiments have shown the absence of chlorine in XP spectra. When a perovskite is heated in DCM, chlorine becomes increasingly intense with time. This in and of itself presents an interesting scientific pursuit from a fundaments standpoint to gain a greater understanding of solvent diffusion through the perovskite crystal lattice with regards to the effective size and properties of the solvent as well as temperature and time. This fundamental pursuit may give clarity to the BF_3 experiments utilizing high temperatures and why these experiments yield >100% coverage. BF_3 and DCM are small molecules relative to the perovskite lattice.

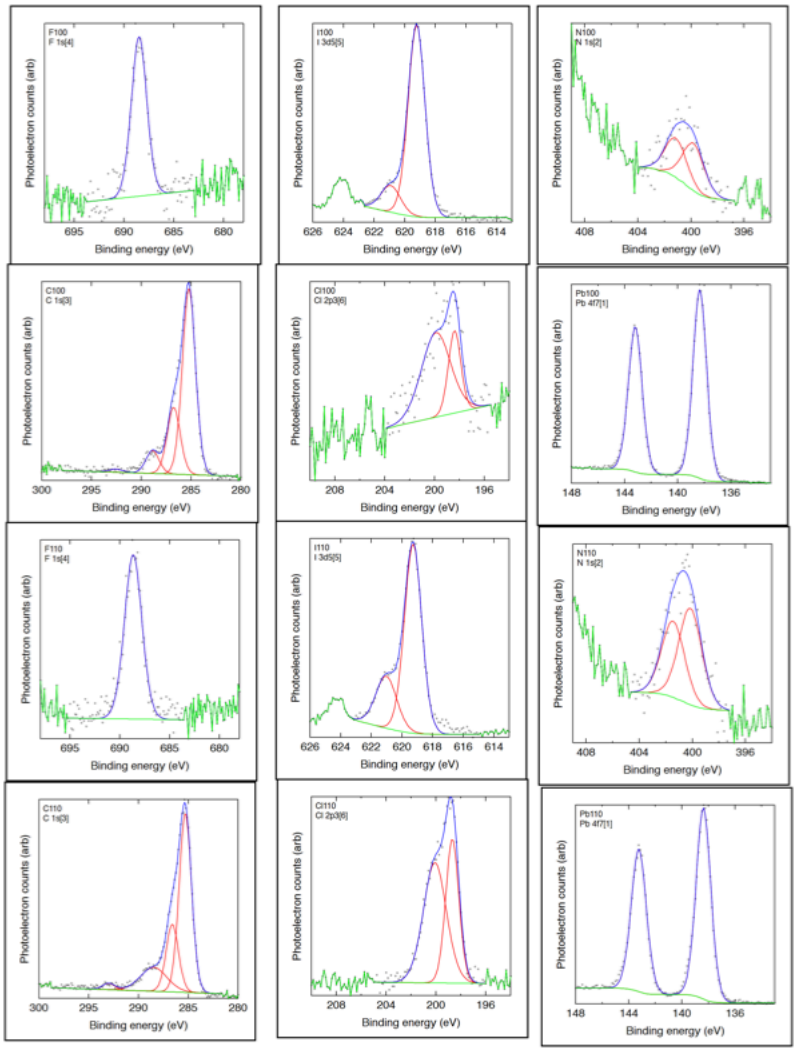

Figure 55. XP spectra for both a $(100)_t$ and a $(112)_t$ perovskite (first two rows and second two rows respectively). Both perovskites exhibit ammonium exchange as seen in prior experiments at ambient temperatures. The difference in this case is the elevated temperature and the appearance of a significant signal in the chlorine region. These scans were not scaled relative to iodine as other figures have been.

References

(1) Oga, H.; Saeki, A.; Ogomi, Y.; Hayase, S.; Seki, S. Improved Understanding of the Electronic and Energetic Landscapes of Perovskite Solar Cells: High Local Charge Carrier Mobility, Reduced Recombination, and Extremely Shallow Traps. *J. Am. Chem. Soc.* **2014**, *136* (39), 13818–13825.

(2) Steirer, K. X.; Schulz, P.; Teeter, G.; Stevanovic, V.; Yang, M.; Zhu, K.; Berry, J. J. Defect Tolerance in Methylammonium Lead Triiodide Perovskite. *ACS Energy Lett.* **2016**, *1* (2), 360–366.

(3) Yin, W.; Shi, T.; Yan, Y. Unique Properties of Halide Perovskites as Possible Origins of the Superior Solar Cell Performance. *Adv. Mater.* **2014**, *26* (27), 4653–4658.

(4) Bush, K. A.; Palmstrom, A. F.; Zhengshan, J. Y.; Boccard, M.; Cheacharoen, R.; Mailoa, J. P.; McMeekin, D. P.; Hoye, R. L. Z.; Bailie, C. D.; Leijtens, T. 23.6%-Efficient Monolithic Perovskite/Silicon Tandem Solar Cells with Improved Stability. *Nat. Energy* **2017**, *2* (4), 17009.

(5) De Vos, A. Detailed Balance Limit of the Efficiency of Tandem Solar Cells. *J. Phys. D. Appl. Phys.* **1980**, *13* (5), 839.

(6) Tan, Z.-K.; Moghaddam, R. S.; Lai, M. L.; Docampo, P.; Higler, R.; Deschler, F.; Price, M.; Sadhanala, A.; Pazos, L. M.; Credgington, D. Bright Light-Emitting Diodes Based on Organometal Halide Perovskite. *Nat. Nanotechnol.* **2014**, *9* (9), 687–692.

(7) Pathak, S.; Sakai, N.; Wisnivesky Rocca Rivarola, F.; Stranks, S. D.; Liu, J.; Eperon, G. E.; Ducati, C.; Wojciechowski, K.; Griffiths, J. T.; Haghighirad, A. A. Perovskite Crystals for Tunable White Light Emission. *Chem. Mater.* **2015**, *27* (23), 8066–8075.

(8) Frost, J. M.; Butler, K. T.; Brivio, F.; Hendon, C. H.; Van Schilfgaarde, M.; Walsh, A. Atomistic Origins of High-Performance in Hybrid Halide Perovskite Solar Cells. *Nano Lett.* **2014**, *14* (5), 2584–2590.

(9) Conings, B.; Drijkoningen, J.; Gauquelin, N.; Babayigit, A.; D'Haen, J.; D'Olieslaeger, L.; Ethirajan, A.; Verbeeck, J.; Manca, J.; Mosconi, E. Intrinsic Thermal Instability of Methylammonium Lead Trihalide Perovskite. *Adv. Energy Mater.* **2015**, *5* (15).

(10) Müller, C.; Glaser, T.; Plogmeyer, M.; Sendner, M.; Döring, S.; Bakulin, A. A.; Brzuska, C.; Scheer, R.; Pshenichnikov, M. S.; Kowalsky, W.; et al. Water Infiltration in Methylammonium Lead Iodide Perovskite: Fast and Inconspicuous. *Chem. Mater.* **2015**, *27* (22), 7835–7841.

(11) Tong, C.-J.; Geng, W.; Tang, Z.-K.; Yam, C.-Y.; Fan, X.-L.; Liu, J.; Lau, W.-M.; Liu, L.-M. Uncovering the Veil of the Degradation in Perovskite CH3NH3PbI3 upon Humidity Exposure: A First-Principles Study. *J. Phys. Chem. Lett.* **2015**, *6* (16), 3289–3295.

(12) Back, H.; Kim, G.; Kim, J.; Kong, J.; Kim, T. K.; Kang, H.; Kim, H.; Lee, J.; Lee, S.; Lee, K. Achieving Long-Term Stable Perovskite Solar Cells via Ion Neutralization. *Energy Environ. Sci.* **2016**, *9* (4), 1258–1263.

(13) Manser, J. S.; Saidaminov, M. I.; Christians, J. A.; Bakr, O. M.; Kamat, P. V. Making and Breaking of Lead Halide Perovskites. *Acc. Chem. Res.* **2016**, *49* (2), 330–338.

(14) Nie, W.; Blancon, J.-C.; Neukirch, A. J.; Appavoo, K.; Tsai, H.; Chhowalla, M.; Alam, M. A.; Sfeir, M. Y.; Katan, C.; Even, J. Light-Activated Photocurrent Degradation and Self-Healing in Perovskite Solar Cells. *Nat. Commun.* **2016**, *7*, 11574.

(15) Cao, J.; Yin, J.; Yuan, S.; Zhao, Y.; Li, J.; Zheng, N. Thiols as Interfacial Modifiers to Enhance the Performance and Stability of Perovskite Solar Cells. *Nanoscale* **2015**, *7* (21), 9443–9447.

(16) Salim, K. M. M.; Koh, T. M.; Bahulayan, D.; Harikesh, P. C.; Jamaludin, N. F.; Febriansyah, B.; Bruno, A.; Mhaisalkar, S.; Mathews, N. Extended Absorption Window and Improved Stability of Cesium-Based Triple-Cation Perovskite Solar Cells Passivated with Perfluorinated Organics. *ACS Energy Lett.* **2018**, *3*, 1068–1076.

(17) Zheng, X.; Chen, B.; Dai, J.; Fang, Y.; Bai, Y.; Lin, Y.; Wei, H.; Zeng, X. C.; Huang, J. Defect Passivation in Hybrid Perovskite Solar Cells Using Quaternary Ammonium Halide Anions and Cations. *Nat. Energy* **2017**, *2* (7), 17102.

(18) Zardetto, V.; Williams, B. L.; Perrotta, A.; Di Giacomo, F.; Verheijen, M. A.; Andriessen, R.; Kessels, W. M. M.; Creatore, M. Atomic Layer Deposition for Perovskite Solar Cells: Research Status, Opportunities and Challenges. *Sustain. Energy Fuels* **2017**, *1* (1), 30–55.

(19) Di Giacomo, F.; Zardetto, V.; Lucarelli, G.; Cinà, L.; Di Carlo, A.; Creatore, M.; Brown, T. M. Mesoporous Perovskite Solar Cells and the Role of Nanoscale Compact Layers for Remarkable All-Round High Efficiency under Both Indoor and Outdoor Illumination. *Nano Energy* **2016**, *30*, 460–469.

(20) Yang, D.; Yang, R.; Zhang, J.; Yang, Z.; Liu, S. F.; Li, C. High Efficiency Flexible Perovskite Solar Cells Using Superior Low Temperature TiO 2. *Energy Environ. Sci.* **2015**, *8* (11), 3208–3214.

(21) Kaloni, T. P.; Giesbrecht, P. K.; Schreckenbach, G.; Freund, M. S. Polythiophene: From Fundamental Perspectives to Applications. *Chem. Mater.* **2017**, *29* (24),

10248–10283.

(22) Nielander, A. C.; Bierman, M. J.; Petrone, N.; Strandwitz, N. C.; Ardo, S.; Yang, F.; Hone, J.; Lewis, N. S. Photoelectrochemical Behavior of N-Type Si(111) Electrodes Coated With a Single Layer of Graphene. *J. Am. Chem. Soc.* **2013**, *135* (46), 17246–17249.

(23) Kim, S.; Shin, D. H.; Kim, C. O.; Kang, S. S.; Kim, J. M.; Jang, C. W.; Joo, S. S.; Lee, J. S.; Kim, J. H.; Choi, S.-H.; et al. Graphene p–n Vertical Tunneling Diodes. *ACS Nano* **2013**, *7* (6), 5168–5174.

(24) Johannsen, J. C.; Ulstrup, S.; Crepaldi, A.; Cilento, F.; Zacchigna, M.; Miwa, J. A.; Cacho, C.; Chapman, R. T.; Springate, E.; Fromm, F.; et al. Tunable Carrier Multiplication and Cooling in Graphene. *Nano Lett.* **2015**, *15* (1), 326–331.

(25) Liu, H.; Liu, Y.; Zhu, D. Chemical Doping of Graphene. *J. Mater. Chem.* **2011**, *21* (10), 3335–3345.

(26) Miao, X.; Tongay, S.; Petterson, M. K.; Berke, K.; Rinzler, A. G.; Appleton, B. R.; Hebard, A. F. High Efficiency Graphene Solar Cells by Chemical Doping. *Nano Lett.* **2012**, *12* (6), 2745–2750.

(27) Hagfeldt, A.; Boschloo, G.; Sun, L.; Kloo, L.; Pettersson, H. Dye-Sensitized Solar Cells. *Chem. Rev.* **2010**, *110* (11), 6595–6663.

(28) Stoumpos, C. C.; Malliakas, C. D.; Kanatzidis, M. G. Semiconducting Tin and Lead Iodide Perovskites with Organic Cations: Phase Transitions, High Mobilities, and Near-Infrared Photoluminescent Properties. *Inorg. Chem.* **2013**, *52* (15), 9019–9038.

(29) Glaser, T.; Müller, C.; Sendner, M.; Krekeler, C.; Semonin, O. E.; Hull, T. D.; Yaffe, O.; Owen, J. S.; Kowalsky, W.; Pucci, A.; et al. Infrared Spectroscopic Study of Vibrational Modes in Methylammonium Lead Halide Perovskites. *J. Phys. Chem. Lett.* **2015**, *6* (15), 2913–2918.

(30) Taufique, M. F. N.; Mortuza, S. M.; Banerjee, S. Mechanistic Insight into the Attachment of Fullerene Derivatives on Crystal Faces of Methylammonium Lead Iodide Based Perovskites. *J. Phys. Chem. C* **2016**, *120* (39), 22426–22432.

(31) Geng, W.; Tong, C.-J.; Tang, Z.-K.; Yam, C.; Zhang, Y.-N.; Lau, W.-M.; Liu, L.-M. Effect of Surface Composition on Electronic Properties of Methylammonium Lead Iodide Perovskite. *J. Mater.* **2015**, *1* (3), 213–220.

(32) Zhou Wang Zhou, Y., Pang, S., Wang, D., Xu, H., Liu, Z., Padture, N. P. and Cui, G., Z, Z. Methylamine-Gas-Induced Defect-Healing Behavior of CH3NH3PbI3 Thin Films for Perovskite Solar Cells. . *Angew. Chem. Int. Ed* **2015**, *54* (33), 9705–9709.

(33) Hunger, R.; Fritsche, R.; Jaeckel, B.; Jaegermann, W.; Webb, L. J.; Lewis, N. S. Chemical and Electronic Characterization of Methyl-Terminated Si (111) Surfaces by High-Resolution Synchrotron Photoelectron Spectroscopy. *Phys. Rev. B* **2005**, *72* (4), 45317.

(34) Li, Y.; O'Leary, L. E.; Lewis, N. S.; Galli, G. Combined Theoretical and Experimental Study of Band-Edge Control of Si through Surface Functionalization. *J. Phys. Chem. C* **2013**, *117* (10), 5188–5194.

(35) Johansson, E.; Boettcher, S. W.; O'Leary, L. E.; Poletayev, A. D.; Maldonado, S.; Brunschwig, B. S.; Lewis, N. S. Control of the Ph-Dependence of the Band Edges of Si (111) Surfaces Using Mixed Methyl/Allyl Monolayers. *J. Phys. Chem. C* **2011**, *115* (17), 8594–8601.

(36) Saidaminov, M. I. et al. High-Quality Bulk Hybrid Perovskite Single Crystals within Minutes by Inverse Temperature Crystallization. . *Nat. Commun.* **2015**, *6*.

(37) Zhang, Y.; Huang, F.; Mi, Q. Preferential Facet Growth of Methylammonium Lead Halide Single Crystals Promoted by Halide Coordination. *Chem. Lett.* **2016**, *45* (8), 1030–1032.

(38) O'Donnell, R. M.; Sampaio, R. N.; Li, G.; Johansson, P. G.; Ward, C. L.; Meyer, G. J. Photoacidic and Photobasic Behavior of Transition Metal Compounds with Carboxylic Acid Group(S). *J. Am. Chem. Soc.* **2016**, *138* (11), 3891–3903.

(39) Benson, E. E.; Grice, K. A.; Smieja, J. M.; Kubiak, C. P. Structural and Spectroscopic Studies of Reduced [Re (Bpy-R)(CO) 3]– 1 Species Relevant to CO 2 Reduction. *Polyhedron* **2013**, *58*, 229–234.

(40) Al-Azani, M.; al-Sulaibi, M.; al Soom, N.; Al Jasem, Y.; Bugenhagen, B.; Al Hindawi, B.; Thiemann, T. The Use of BrCCl3-PPh3 in Appel Type Transformations to Esters, O-Acyloximes, Amides, and Acid Anhydrides. *Comptes Rendus Chim.* **2016**, *19* (8), 921–932.

(41) Gowda, D. C.; Mahesh, B.; Gowda, S. Zinc-Catalyzed Ammonium Formate Reductions : Rapid and Selective Reduction of Aliphatic and Aromatic Nitro Compounds. *Indian J. Chem.* **2001**, *40* (B), 75–77.

(42) Ebel, M. F. Zur Bestimmung Der Reduzierten Dicke D/λ Dünner Schichten Mittels XPS. *J. Electron Spectros. Relat. Phenomena* **1978**, *14* (4), 287–322.

(43) Seah, M. P. Quantification of AES and XPS. In *Practical Surface Analysis*; Briggs, D., Seah, M. P., Eds.; John Wiley & Sons, 1990; p 201–255.

(44) Carl, A. D.; Kalan, R. E.; Obayemi, J. D.; Zebaze Kana, M. G.; Soboyejo, W. O.; Grimm, R. L. Synthesis and Characterization of Alkylamine-Functionalized Si(111)

for Perovskite Adhesion With Minimal Interfacial Oxidation or Electronic Defects. *ACS Appl. Mater. Interfaces* **2017**, *9* (39), 34377–34388.

(45) Fadley, C. S. Solid State—and Surface—Analysis by Means oF Angular-Dependent x-Ray Photoelectron Spectroscopy. *Prog. solid state Chem.* **1976**, *11*, 265–343.

(46) Wagner, C. D.; Davis, L. E.; Zeller, M. V; Taylor, J. A.; Raymond, R. H.; Gale, L. H. Empirical Atomic Sensitivity Factors for Quantitative Analysis by Electron Spectroscopy for Chemical Analysis. *Surf. Interface Anal.* **1981**, *3* (5), 211–225.

(47) Moulder, J. F.; Chastain, J. *Handbook of X-Ray Photoelectron Spectroscopy: A Reference Book of Standard Spectra for Identification and Interpretation of XPS Data*; Physical Electronics Division, Perkin-Elmer Corporation, 1992.

(48) Scofield, J. H. Hartree-Slater Subshell Photoionization Cross-Sections at 1254 and 1487 EV. *J. Electron Spectros. Relat. Phenomena* **1976**, *8* (2), 129–137.

(49) Yamada, Y.; Yamada, T.; Phuong, L. Q.; Maruyama, N.; Nishimura, H.; Wakamiya, A.; Murata, Y.; Kanemitsu, Y. Dynamic Optical Properties of CH3NH3PbI3 Single Crystals as Revealed by One-and Two-Photon Excited Photoluminescence Measurements. *J. Am. Chem. Soc.* **2015**, *137* (33), 10456–10459.

(50) Ferraria, A. M.; da Silva, J. D. L.; do Rego, A. M. B. XPS Studies of Directly Fluorinated HDPE: Problems and Solutions. *Polymer (Guildf).* **2003**, *44* (23), 7241–7249.

(51) Cumpson, P. J.; Seah, M. P. Elastic Scattering Corrections in AES and XPS. II. Estimating Attenuation Lengths and Conditions Required for Their Valid Use in Overlayer/Substrate Experiments. *Surf. Interface Anal. An Int. J. devoted to Dev. Appl. Tech. Anal. surfaces, interfaces thin Film.* **1997**, *25* (6), 430–446.

(52) Gray, H. B. *Chemical Bonds: An Introduction to Atomic and Molecular Structure*, 2nd ed.; University Science Books: Sausalito, CA, 1996.

(53) Linstrom, P. J.; Mallard, W. G. NIST Chemistry Webbook; NIST Standard Reference Database No. 69. **2001**.

(54) Redhead, P. A. Thermal Desorption of Gases. *Vacuum* **1962**, *12* (4), 203–211.

(55) Ozensoy, E.; Meier, D. C.; Goodman, D. W. Polarization Modulation Infrared Reflection Absorption Spectroscopy at Elevated Pressures: CO Adsorption on Pd(111) at Atmospheric Pressures. *J. Phys. Chem. B* **2002**, *106* (36), 9367–9371.

(56) Finke, S. J. Infrared Reflection-Absorption Spectroscopy of Thin Film Structures, Iowa State University, 1988.

(57) Soltani, Y.; Wilkins, L. C.; Melen, R. L. Stoichiometric and Catalytic C–C and C–H Bond Formation with B(C6F5)3 via Cationic Intermediates. *Angew. Chemie Int. Ed.* **2017**, *56* (39), 11995–11999.

(58) Dualeh, A.; Gao, P.; Seok, S. Il; Nazeeruddin, M. K.; Grätzel, M. Thermal Behavior of Methylammonium Lead-Trihalide Perovskite Photovoltaic Light Harvesters. *Chem. Mater.* **2014**, *26* (21), 6160–6164.

(59) Colella, S.; Mosconi, E.; Pellegrino, G.; Alberti, A.; Guerra, V. L. P.; Masi, S.; Listorti, A.; Rizzo, A.; Condorelli, G. G.; De Angelis, F.; et al. Elusive Presence of Chloride in Mixed Halide Perovskite Solar Cells. *J. Phys. Chem. Lett.* **2014**, *5* (20), 3532–3538.

(60) Wang, Y.; Trenary, M. *Surface Chemistry of Boron Oxidation. 2. The Reactions of Boron Oxides B2O2 and B2O3 with Boron Films Grown on Tantalum(110)*; 1993; Vol. 5.

(61) Linstrom, P. J.; Mallard, W. G. NIST Chemistry Webbook. National Institute of Standards and Technology Gaithersburg, MD 2001.

(62) Elisabeth, J.; Lars, N. XPS Study of Carboxylic Acid Layers on Oxidized Metals with Reference to Particulate Materials. *Surf. Interface Anal.* **2003**, *35* (4), 375–381.

(63) Poglitsch, A.; Weber, D. Dynamic Disorder in Methylammoniumtrihalogenoplumbates (II) Observed by Millimeter-wave Spectroscopy. *J. Chem. Phys.* **1987**, *87* (11), 6373–6378.

(64) Saidi, W. A.; Choi, J. J. Nature of the Cubic to Tetragonal Phase Transition in Methylammonium Lead Iodide Perovskite. *J. Chem. Phys.* **2016**, *145* (14), 144702.

(65) Whitfield, P. S.; Herron, N.; Guise, W. E.; Page, K.; Cheng, Y. Q.; Milas, I.; Crawford, M. K. Structures, Phase Transitions and Tricritical Behavior of the Hybrid Perovskite Methyl Ammonium Lead Iodide. *Sci. Rep.* **2016**, *6*, 35685.

(66) Gao, W.; Zielinski, K.; Drury, B. N.; Carl, A. D.; Grimm, R. L. Elucidation of Chemical Species and Reactivity at Methylammonium Lead Iodide and Cesium Tin Bromide Perovskite Surfaces via Orthogonal Reaction Chemistry. *J. Phys. Chem. C* **2018**.

(67) Li, S.; Zhang, F.; Sun, Q.; Li, Z.; Cui, Y.; Ji, T.; Qin, W.; Zhu, F.; Hao, Y. Entire Mirror-like Perovskite Films for High-Performance Perovskite Solar Cells: The Role of Polar Anti-Solvent Sec-Pentyl Alcohol. *Org. Electron.* **2018**, *57*, 133–139.

(68) Jeon, N. J.; Noh, J. H.; Yang, W. S.; Kim, Y. C.; Ryu, S.; Seo, J.; Seok, S. Il. Compositional Engineering of Perovskite Materials for High-Performance Solar Cells. *Nature* **2015**, *517* (7535), 476.

(69) Li, Z.; Yang, M.; Park, J.-S.; Wei, S.-H.; Berry, J. J.; Zhu, K. Stabilizing Perovskite Structures by Tuning Tolerance Factor: Formation of Formamidinium and Cesium Lead Iodide Solid-State Alloys. *Chem. Mater.* **2015**, *28* (1), 284–292.

(70) Rolston, N.; Printz, A. D.; Tracy, J. M.; Weerasinghe, H. C.; Vak, D.; Haur, L. J.; Priyadarshi, A.; Mathews, N.; Slotcavage, D. J.; McGehee, M. D.; et al. Effect of Cation Composition on the Mechanical Stability of Perovskite Solar Cells. *Adv. Energy Mater.* **2018**, *8* (9).

(71) Marandi, F.; Nikpey, Z.; Khosravi, M.; Hosseini, S.; Fun, H.-K.; Hemamalini, M. Synthesis and Characterization of Lead(II) Complexes with Substituted 2,2′-Bipyridines, Trifluoroacetate, and Furoyltrifluoroacetonate. *J. Coord. Chem.* **2011**, *64* (17), 3012–3021.

(72) Gray, P. A.; Krause, K. D.; Burford, N.; Patrick, B. O. Cationic 2, 2′-Bipyridine Complexes of Germanium (Ii) and Tin (Ii). *Dalt. Trans.* **2017**, *46* (26), 8363–8366.

(73) Zhang, D. W.; Li, X. D.; Li, H. B.; Chen, S.; Sun, Z.; Yin, X. J.; Huang, S. M. Graphene-Based Counter Electrode for Dye-Sensitized Solar Cells. *Carbon N. Y.* **2011**, *49* (15), 5382–5388.

(74) DoE, U. S. W. D. C. International Energy Outlook (IEO). **2017**.

(75) Ankati, H.; Zhu, D.; Yang, Y.; Biehl, E. R.; Hua, L. Asymmetric Synthesis of Both Antipodes of β-Hydroxy Nitriles and β-Hydroxy Carboxylic Acids via Enzymatic Reduction or Sequential Reduction/Hydrolysis. *J. Org. Chem.* **2009**, *74* (4), 1658–1662.

(76) Baud, M. G. J.; Leiser, T.; Haus, P.; Samlal, S.; Wong, A. C.; Wood, R. J.; Petrucci, V.; Gunaratnam, M.; Hughes, S. M.; Buluwela, L.; et al. Defining the Mechanism of Action and Enzymatic Selectivity of Psammaplin A against Its Epigenetic Targets. *J. Med. Chem.* **2012**, *55* (4), 1731–1750.